

COUPLING BETWEEN THE FLUCTUATING WIND FIELD, WAVE FIELD AND THE MOMENTUM FLUX

Final Report

N00014 -93 -1 - 0360

**Larry Mahrt
College of Oceanic and Atmospheric Sciences
Oregon State University
Corvallis, OR 97331**

DISTRIBUTION STATEMENT A

**Approved for public release
Distribution Unlimited**

Prepared for:

**Grant Monitor: Scott Sandgathe
Atmospheric Modeling and Prediction
Office of Naval Research**

19970717 161

DTIC QUALITY INSPECTED 3

5 Dec 1995



DEPARTMENT OF THE NAVY
OFFICE OF NAVAL RESEARCH
SEATTLE REGIONAL OFFICE
1107 NE 45TH STREET, SUITE 350
SEATTLE WA 98105-4631

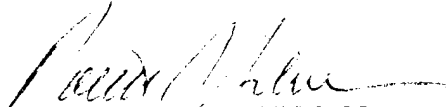
IN REPLY REFER TO:

4330
ONR 247
11 Jul 97

From: Director, Office of Naval Research, Seattle Regional Office, 1107 NE 45th St., Suite 350, Seattle, WA 98105
To: Defense Technical Center, Attn: P. Mawby, 8725 John J. Kingman Rd., Suite 0944, Ft. Belvoir, VA 22060-6218

Subj: RETURNED GRANTEE/CONTRACTOR TECHNICAL REPORTS

1. This confirms our conversations of 27 Feb 97 and 11 Jul 97. Enclosed are a number of technical reports which were returned to our agency for lack of clear distribution availability statement. This confirms that all reports are unclassified and are "APPROVED FOR PUBLIC RELEASE" with no restrictions.
2. Please contact me if you require additional information. My e-mail is silverr@onr.navy.mil and my phone is (206) 625-3196.


ROBERT J. SILVERMAN

COUPLING BETWEEN THE FLUCTUATING WIND FIELD, WAVE FIELD AND THE MOMENTUM FLUX

Final Report

N00014 -93 -1 - 0360

**Larry Mahrt
College of Oceanic and Atmospheric Sciences
Oregon State University
Corvallis, OR 97331**

Prepared for:

**Grant Monitor: Scott Sandgathe
Atmospheric Modeling and Prediction
Office of Naval Research**

5 Dec 1995

Table of Contents

1. Introduction	1
2. Sea surface drag coefficients in RASEX	2
3. Roughness lengths in coastal terrain	32
4. Quality control and flux sampling problems: Application to RASEX	36
5. Further work on the Kitaigorodskii roughness length model: A new derivation using Lettau's expression on steep waves	66
6. List of papers supported by this grant	87

1. INTRODUCTION TO THE RESULTS

The manuscript "Sea surface drag coefficients in RASEX", to appear in the *Journal of Geophysical Research* (first chapter of this report), systematically shows that the drag coefficient at weak wind speeds is sensitive to the method of calculation and also sensitive to the flux sampling errors. This sensitivity probably explains some of the confusion and discrepancies in the literature. More specifically the quantitative increase of the drag coefficient at weak wind speeds varies between studies partly because the method of analysis of the drag coefficient varies between studies. The current debate between the applicability of the "smooth flow" and "rough flow" predictions of the drag coefficient cannot be addressed with data analysis until more care is given to the method of calculation of the drag coefficient, and, until more stationary records for the weak wind case are collected.

This manuscript also reveals the dominating effect of fetch on the drag coefficient. For the present analysis, the drag coefficient increases with decreasing fetch indicating the influence of growing steep waves. In contrast, the results in Chapter II (Roughness lengths in coastal terrain) suggest that the roughness height decreases with decreasing fetch. The discrepancy is explained by noting that the later study estimated the stress from the profile method while the former study use direct eddy correlation methods. We have learned that with offshore flow and short fetch, existing similarity theory does not apply so that the profile method does not work. Furthermore, existing stability functions for Monin Obukhov similarity theory also fail to explain the stability dependence of the transfer coefficients. Either the roughness length must be stability dependent or new stability functions are required. Definite solutions cannot be offered until a more thorough analysis of the wave field can be completed.

In "Quality control and flux sampling problems: Application to RASEX" (Chapter III), the RASEX data is subjected to more than 20 quality control procedures and various flux sampling errors. Certain records are hard flagged for instrumentation errors while other records are soft flagged for unusual, but physically plausible, time series. The flux sampling errors are large primarily for weak wind cases.

Finally, "Further work on the Kitaigorodskii roughness length model: A new derivation using Lettau's expression on steep waves" (Chapter IV), derives a new methodology for relating the wave age to the wave statistics. This approach will be applied to the RASEX wave data in order to assess the influence of the wave characteristics on the surface stress.

Sea surface drag coefficients in RASEX

L. Mahrt, Dean Vickers, Jim Howell
College of Oceanic and Atmospheric Sciences
Oregon State University
Corvallis, OR 97331 USA

Jørgen Højstrup
Risø National Laboratory
4000 Roskilde, Denmark

James M. Wilczak
Environmental Technology Lab., ERL/NOAA
Boulder, CO 80303 USA

Jim Edson and Jeffrey Hare
Woods Hole Oceanographic Institute
Woods Hole, MA 02543, USA

27 Nov 1995

Abstract

This study examines the dependence of the computed drag coefficient on wind speed, stability, fetch, flux sampling problems and method of calculation of the drag coefficient. This analysis is applied to data collected at a tower 2 km off the coast of Denmark during the Risø Air Sea Experiment (RASEX). Large drag coefficients are observed with weak large scale flow. However the value of the computed drag coefficient at weak wind speeds is sensitive to fetch, stability, flux sampling problems and the method of calculation of the drag coefficient.

1. Introduction

The drag coefficient over the sea is thought to increase as the wind speed becomes weak. Recently, Wu (1994) has suggested that closely packed capillary waves associated with surface tension partly explains the large drag coefficients at weak winds observed by Geernaert et al. (1988) and Bradley et al. (1991). Recently, Greenhut and Khalsa (1995) have observed a similar increase of the drag coefficient at low wind speeds.

In addition to wind speed and surface tension, the drag coefficient depends on a number of other factors. For a given wind speed, the stress is expected to be greater with young developing waves and smaller with decaying waves (Kitaigorodskii, 1973; Nordeng, 1991; Geernaert et al., 1987, 1988; Donelan, 1990; Maat et al., 1991) even after accounting for built in correlation associated with the usual method of relating the drag coefficient to wave age (Smith et al., 1992). More directly, the drag coefficient increases with wave steepness. As a result, most studies indicate that the drag coefficient decreases with wave age although laboratory data analyzed in Toba et al. (1990) includes a counter example. Since the drag coefficient for a given wind speed is larger with young developing waves, the drag coefficient is expected to be larger with flow acceleration, as observed in Large and Pond (1981) and Smith (1980). In fact, the stress may become very small or even reverse sign with significant deceleration implying small or negative drag coefficients (Smedman et al., 1994). Unfortunately, during rapid acceleration, the stress is nonstationary and the calculated stress is sensitive to choice of averaging scales. The drag coefficient is also influenced by changing wind direction, fetch (Geernaert et al., 1988), water depth, and wave breaking (Banner, 1990). Shoaling processes can cause changes of wave shape and wave breaking in shallow water (Freilich and Guza, 1984; Freilich et al., 1990) leading to increased stress, while limited fetch can enhance the stress through wave growth.

Fluxes and exchange coefficients are often computed from data without considering the dependence of these quantities on averaging lengths and sampling errors, which become especially important at weak wind speeds. The choice of averaging length and use of any detrending or filtering varies between different studies so that comparison of fluxes and exchange coefficients is sometimes ambiguous. While there are no guidelines for a "standard calculation" of the flux, this study will focus on the sensitivity of the flux and

exchange coefficients to the method of calculation. If the values of the flux and exchange coefficients are sensitive to the calculation procedure, then this calculation is not "well posed".

The principal difficulty in estimating fluxes is that motions simultaneously occur on a variety of scales; often small mesoscale motions occur on scales only slightly larger than turbulent scales corresponding to nonstationarity (heterogeneity) and absence of the textbook "spectral gap". The division between the turbulence and mesoscale motions is not always obvious. For example, roll vortices are generally considered as turbulence and can lead to significant flux at higher levels in the boundary layer (LeMone, 1973; Mourad and Brown, 1990) even though such motions are neither fully three dimensional, nor random. However, their signal observed from tower data appears on time scales longer than that normally included as turbulence.

Significant mesoscale variability occurs in most atmospheric boundary layers even in the absence of well defined mesoscale circulations such as sea breezes and organized moist convection (Lilly, 1983). Mesoscale motions may be generated by a number of instabilities (Emanuel, 1983) including gravity waves and convection waves coupled to boundary layer eddies (Hauf and Clark, 1989). Geernaert et al. (1987) observed oscillations of the surface stress direction over the sea with a period of 3-4 hours. Mahrt and Gibson (1992) observed oscillations of the stress magnitude (direction was not included in their analysis) on a similar time scale at a coastal site. Both studies speculate that inertial-gravity waves at the top of the boundary layer are one possible candidate. Oscillations of the stress sometimes occur with significant differences between the wind direction and wave directions (Plant, 1982; Geernaert, 1988). Furthermore, with ubiquitous mesoscale motion, the mean synoptic flow is difficult to determine from traditional averaging of observations (Pierson, 1983).

When there is significant mesoscale modulation of the turbulent flux, the computed flux is sensitive to the choice of averaging scale, particularly at weak wind speeds. For similar reasons, the computation of the drag coefficient at weak wind speeds becomes sensitive to whether the wind speed is vector averaged or the instantaneous speed is averaged (Godfrey and Beljaars, 1991; Beljaars, 1995; Mahrt and Sun, 1995), whether the cross wind stress is included or not and whether flux sampling criteria are applied. The present study documents these sensitivities. The question then becomes whether the increase of the drag coefficient at weak winds can be predicted with any

confidence.

This question will be addressed using offshore tower data from RASEX described in Section 2. Section 3 introduces the averaging procedures, Section 4 develops the framework for analysis of flux sampling errors while Section 5 examines the dependence of the drag coefficient on method of computation. Section 6 then studies the dependence of the drag coefficient on wind speed, fetch and stability.

2. The data

This study analyzes data from a research tower in shallow water 4 m deep, located 2 km off the Danish coast in the spring and fall of 1994, described by Barthelmie et al. (1994) and Højstrup et al. (1995). The fluctuating wind and virtual temperature data were measured with a Gill/Solent Ultrasonic Anemometer with an asymmetric head mounted 10 m above the sea surface. The asymmetric head was aligned such that the supporting struts did not distort the flow in the preferred wind directions.

The buoyancy flux is computed using virtual temperature fluctuations from the sonic anemometer after making corrections for bending of the acoustic wave by the crosswind flow (Mortensen and Højstrup, 1995). Temperature was measured using a platinum resistance wire (Pt100).

To correct for tilt of the sonic anemometer, a single set of tilt angles were computed using the entire data set. Using 30 minute mean values, the vertical motions for the entire observational period were fit in a least squares sense to the equation

$$w = a + bu + cv. \quad (1)$$

The regression coefficients b and c estimate the dependence of the "measured" vertical velocity on the two measured horizontal velocity components due to tilt of the sonic anemometer from true vertical. The calculation of corrected sonic velocity components are constructed by subtracting the value a and rotating the coordinate system such that the statistical influence of $bu + cv$ vanishes. This transformation of the coordinate system puts the regression prediction in the horizontal plane such that applying Eq. 1 in a least squares sense to the corrected rotated data would yield $a = b = c = 0$. The tilt correction angles are approximately 1° while the displacement a is 0.003 m/s.

However, the small rotation of the data exerted an important influence on the fluxes for the weak wind records and altered the computed drag coefficient by as much as 50%.

Data for wind directions between 340° and 120° were eliminated due to tower interference and possible interference from wind turbines northeast of the observation tower. Winds from 120° to 240° are fetch limited but included in this study, providing 606 one-hour records. The current was measured with the electromagnetic system developed by Geological and Marine Instrumentation (Denmark).

The following analyses will apply simple unweighted averaging with a moving window of length L even though such averaging possesses a "sloppy" response function in Fourier space. Increased complexity of filters with sharper response functions does not seem justified for analysis of turbulence data since the turbulence is not periodic and is often characterized by sharp boundaries such as edges of thermals and wind gusts (Mahrt and Howell, 1994). Furthermore, weighted averaging does not formally satisfy Reynolds averaging although we have found such errors to be relatively small. Detrending is not applied to the analyses reported in this study.

3. Averaging procedure

3.1 Bulk aerodynamic formulation and averaging scales

Turbulent fluctuations of some quantity, ϕ , are defined as deviations from the *local average*, $\bar{\phi}$, in which case the decomposition of ϕ can be written as

$$\phi = \bar{\phi} + \phi' \quad (2)$$

where $\bar{\phi}$ is an average over time scale L . The local averaging length L determines which scales of the motions are included in the computed flux. L might be chosen to include only scales which have characteristics of turbulence. The numerical choice of L is discussed below.

Turbulent fluxes are then computed by averaging the product of the perturbations over some period, λ , which can be chosen to be larger than L . For example, the fluxes might be averaged over the entire record length in which case $\lambda = \text{recordlength}$. λ will be referred to as the *flux averaging length*.

Averaging over length λ is symbolized as $\langle \rangle$ so that the magnitudes of the vector averaged wind and stress are, respectively:

$$\begin{aligned}\langle V \rangle &= (\langle u \rangle^2 + \langle v \rangle^2)^{1/2} \\ \langle w'v' \rangle &= (\langle w'u' \rangle^2 + \langle w'v' \rangle^2)^{1/2}\end{aligned}\quad (3)$$

where v' is the fluctuating horizontal velocity vector and when $\langle \rangle$ operates on a vector, the magnitude of the vector average is implied. Here, the flow is computed to be relative to the moving surface current; that is, the current velocity has been subtracted from the original velocity vector. However, the current, due mainly to the tides, was normally only a few tens of cm/s , and the inclusion of the current velocity was significant only in cases of very weak winds. The momentum flux $\langle w'v' \rangle$ is computed by first forming the time series $w'v'$ where u' and v' are computed as deviations from the averages over the local averaging window L . The product time series $w'v'$ is then averaged over the flux averaging length λ .

The time average of the instantaneous wind speed $\langle V \rangle$ is computed as

$$\langle V \rangle = \langle (u)^2 + (v)^2 \rangle^{1/2} \quad (4)$$

where again the air motion is relative to the surface current. For application to observations, the bulk aerodynamic relationship for momentum is usually written as

$$\langle w'v' \rangle = C_D(L, \lambda) \langle V \rangle^2. \quad (5)$$

where again the averaging operator $\langle \rangle$ designates the magnitude of the vector average. This form of the drag coefficient is used in most observational studies although it could be considered inconsistent in the sense that it mixes scalar and vector averages. For example in the limit of vanishing large scale flow with random instantaneous wind and stress vectors, the vector averaged wind and stress vanish but the average of the instantaneous wind speed does not vanish. Then Eq. 5 predicts the drag coefficient to approach zero with vanishing large scale flow.

For application to numerical models, the wind speed is computed from the grid averaged velocity components computed from the equations of motion, in which case the drag coefficient is defined as

$$\langle w'v' \rangle = \hat{C}_D(L, \lambda) \langle V \rangle^2. \quad (6)$$

where \hat{C}_D is the drag coefficient based on the vector averaged wind. The distinction between these two drag coefficients is illustrated in terms of RASEX data in Section 5.

3.2 Choice of local averaging scale

The local averaging length L must be chosen sufficiently large such that the perturbation flow includes most of the turbulence, although such a determination may be ambiguous in nonstationary conditions. To systematically examine the dependence of the flux on the local averaging scale, all continuous records longer than 10 hrs. were chosen. The records were classified as stationary or nonstationary according to the value of the ratio

$$\beta \equiv \frac{(\sigma_u^2 + \sigma_v^2)^{1/2}}{\langle V \rangle} \quad (7)$$

where the standard deviations are computed from the six 10 minutes average of the wind components for a one hour period and $\langle V \rangle$ is the one hour averaged wind speed. Then the hourly values of β are averaged over the record. The record is classified as nonstationary if the average value of β exceeds 0.1. Six stationary and 11 nonstationary records are found ranging in length from 10 to 24 hours with an averaged length of about 15 hours.

For each subrecord of width $\lambda = L$, the magnitude of the vector averaged momentum flux (Eq. 3) is computed and then averaged over all of the subrecords in a given class (stationary or nonstationary). Fig. shows the flux as a function of local averaging scale. The choice of $L = 5$ min. appears to be adequate to capture most of the turbulence flux for the stationary class. The flux is generally weaker for the nonstationary class which is more often associated with weak winds. The flux for the nonstationary class decreases at the largest scales because of meandering of the stress vector and cancellation associated with sign reversal of the stress components.

3.3 Choice of flux averaging scale

Choosing the flux averaging length λ to be larger than the local averaging length L eliminates short term oscillations of the flux as can be seen by contrasting the thin and thick lines in Figure 2a. Choosing larger λ also improves the flux gradient relationship and performance of the bulk aerodynamic rela-

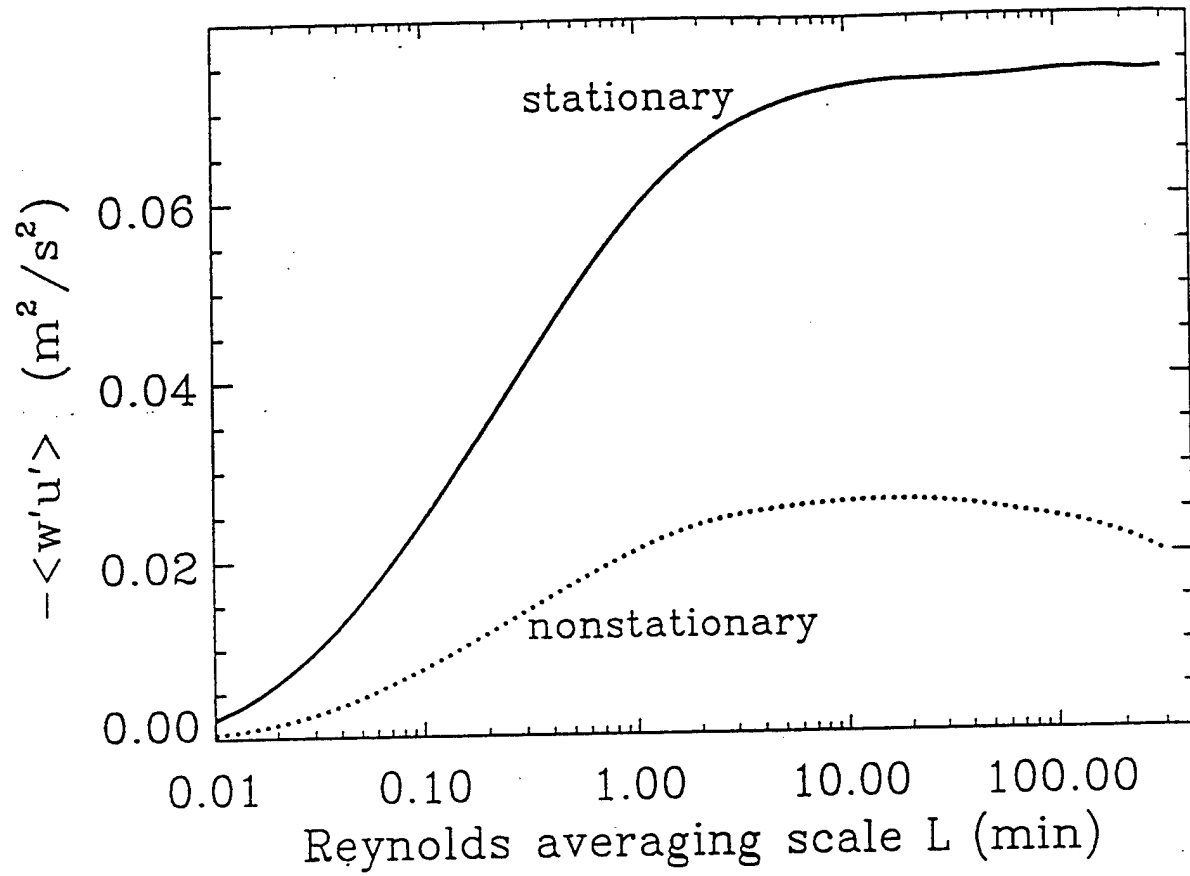


Figure 1: Dependence of the momentum flux (Eq. 3) on the local averaging scale L used to compute perturbation quantities for the stationary (solid) and nonstationary (broken) classes.

tionship by explicitly including only those motions in the mean flow (scales greater than λ) which vary sufficiently slowly to allow adjustment of the turbulent flux to the changing mean flow. Large values of λ additionally ensure a larger sample of the transporting eddies which improves the estimate of the mean turbulent flux. Unfortunately, choosing the flux averaging length λ larger than the local averaging length L increases the chances of inadvertent capture of nonstationarity. Some nonstationarity seems to be always present due to ubiquitous nameless mesoscale motions.

Mesoscale modulation of the turbulent flux is evident in the nonstationary record shown in Figure 2a where the downward turbulent flux reaches a maximum at about 90 minutes into the record. This mesoscale modulation of the turbulent flux is distinct from the direct transport by mesoscale vertical motions $\langle w \rangle$ shown in Figure 2b, where the angle brackets indicate averaging over λ . The magnitude of the mesoscale motion is affected by the correction for the anemometer tilt and is therefore somewhat uncertain. Note that the mesoscale flux in this example is larger than the turbulent flux which in this case is very small. However, the mesoscale flux in RASEX normally decreases in importance with increased flux averaging scale since the mesoscale flux frequently reverses sign (Sun et al., 1995).

In conditions of significant mesoscale modulation of the turbulent flux, the flux may reverse sign within the record (Figure 3) so that the averaged turbulent flux is less than the average of the absolute value of the turbulent flux. In general, increasing the flux averaging length increases the chance of capturing a sign reversal of one of the flux components which reduces the magnitude of the vector averaged flux. As a result, the drag coefficient becomes sensitive to the choice of flux averaging length as occurs for the data used to construct Figure 3.

The drag coefficient for the stationary wind class (Fig. 4) for $L=10$ min. is relatively independent of the flux averaging length λ . However the drag coefficient for the nonstationary class decreases significantly with increasing λ due to modulation or meandering of the stress vector. Increasing λ leads to more sign reversals and cancellation when averaging the stress components over larger scales.

The value of λ can be chosen in terms of the performance of the bulk aerodynamic relationship. That is, what value of λ produces the maximum correlation between the momentum flux and wind speed? This correlation for the stationary class of records is relatively independent of the averaging

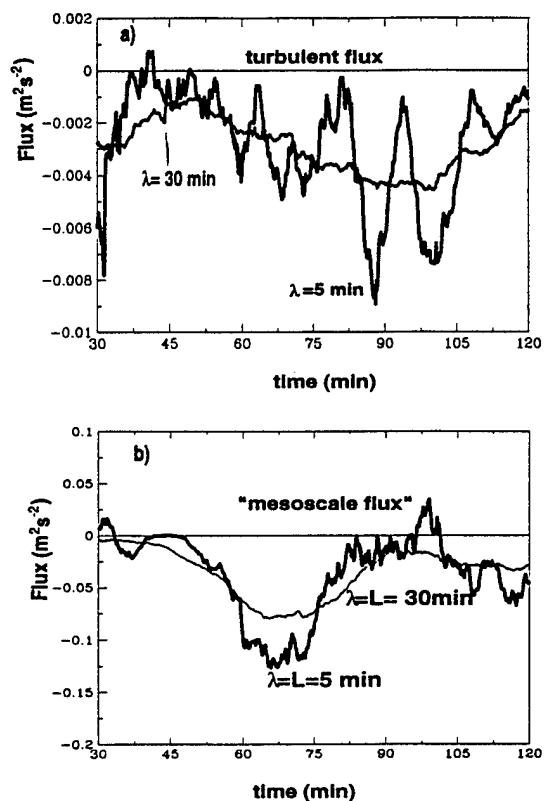


Figure 2: a) Variation of the turbulent flux (upper panel) computed from a moving average using $L = \lambda = 5 \text{ min}$. (thick line), and $L = 5 \text{ min}$, $\lambda = 30 \text{ min}$. (thin line) for a 150 min. record of weak winds where the wind increases from 0.5 m/s at the beginning of the record to 2.0 m/s at the end of the record. b) Variation of the mesoscale flux (lower panel) computed from 5 and 30 min. running means.

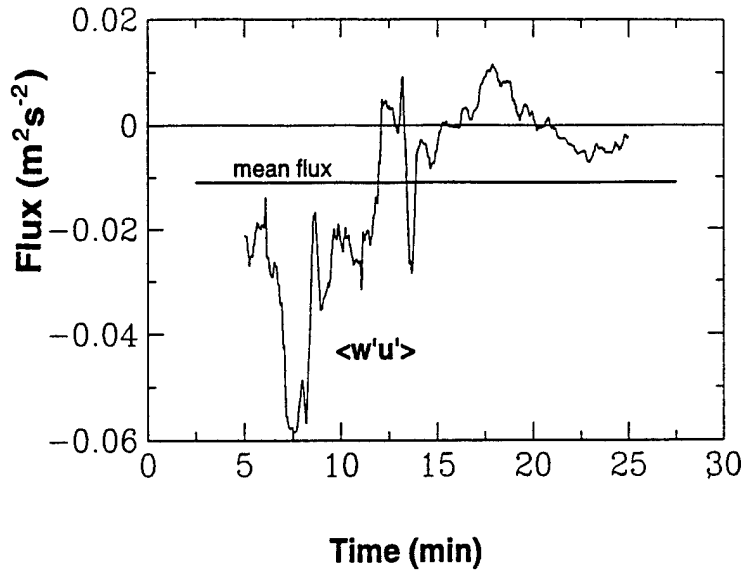


Figure 3: Temporal variation of the turbulent flux computed from a moving average using $L = \lambda = 5$ min. for a strongly nonstationary record.

length (Fig. 5, dashed lines) except at the smallest averaging lengths where a significant fraction of the flux is omitted and the sample size is inadequate.

For the nonstationary class, the correlation between the mean wind and flux is smaller and more sensitive to the local averaging length L (Fig. 5, solid lines). For choice of flux averaging lengths greater than a few hours (not shown), the correlation begins to decrease due to capture of too much nonstationarity with the averaging window. The choice of flux averaging length $\lambda = 1$ hour obtains a near maximum correlation yet remains within the practical and traditional range of averaging lengths.

4. Flux sampling errors and uncertainty

Three types of sampling errors must be considered in assessing the reliability of the flux measurements:

1. The *systematic error* is the failure to capture all of the largest transporting scales, typically leading to an underestimation of the flux.

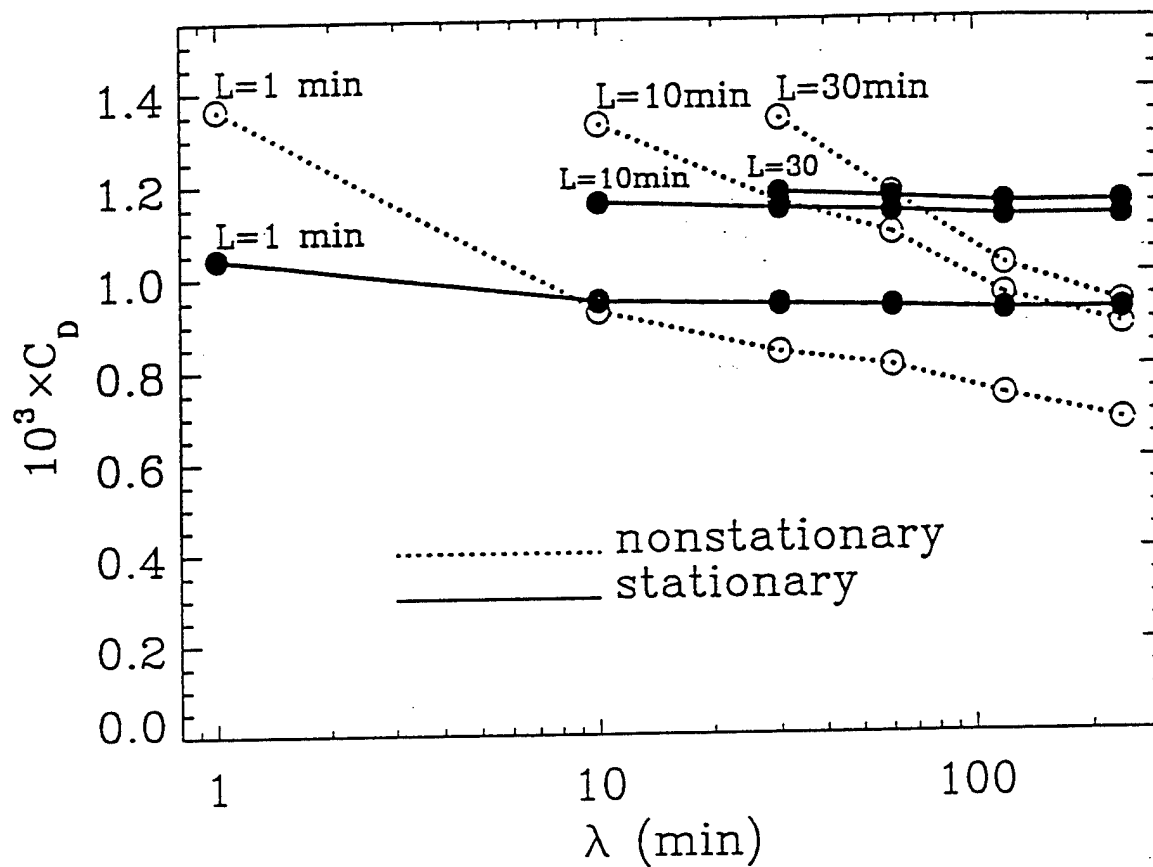


Figure 4: The drag coefficient as a function of flux averaging length λ over which the fluxes and instantaneous wind speed are averaged for stationary (solid) and nonstationary (broken) classes. Each line corresponds to a different value of the averaging length $L \leq \lambda$ which defines the average flow from which the deviations are computed.

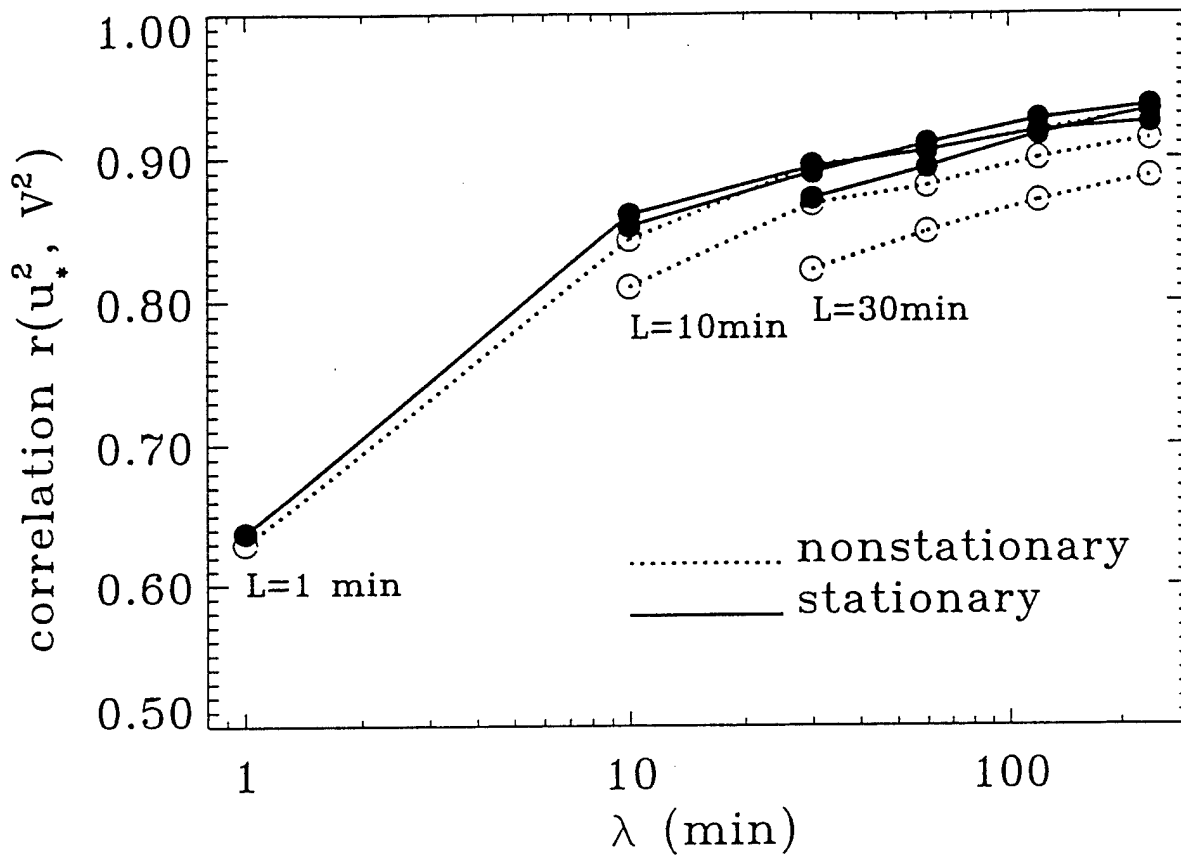


Figure 5: Correlation r between the stress and wind magnitude as a function of flux averaging length λ for stationary (dashed) and nonstationary (solid) classes. Each line corresponds to a different value of the local averaging length $L \leq \lambda$, used to compute the perturbation quantities.

2. The *random error* is due to an inadequate sample of the main transporting eddies as a consequence of small record length.

3. *Nonstationarity* due to mesoscale variability leads to significant dependence of both the flux and drag coefficient on choice of averaging scales (Section 3).

This section develops simple quantitative measures of the above errors and critical values of the measures for flagging records with large errors. However the choice of the critical values will be lenient since elimination of records with these errors systematically reduces the number of weak wind cases and creates a bias towards stronger winds. Some bias cannot be avoided since some of the weak wind records appeared to have very large sampling errors and must be removed from the study of the drag coefficient behavior. The critical values will be chosen by qualitatively maximizing the reduction in scatter in the drag coefficient-wind speed relationship and minimizing the number of records eliminated.

4.1 Systematic errors and choice of local averaging scale L

Although L should be chosen to include almost all of the turbulent flux for stationary conditions, the choice of L is not obvious for nonstationary conditions where the computed flux continues to change with addition of scales larger than those normally associated with turbulence. To document such cases, we define a crude measure of the systematic error

$$RSE \equiv \frac{\langle w' \phi' \rangle_{2L} - \langle w' \phi' \rangle_L}{\langle w' \phi' \rangle_L} \quad (8)$$

where L is chosen to be 10 min. Sixteen of the 606 hourly records are flagged where $|RSE|$ exceeds 0.75.

4.2 Random sampling error and nonstationarity

The ideal choice of the flux averaging length λ is sufficiently long enough to reduce the random error but short enough to avoid capture of nonstationarity associated with meso and synoptic scale variability. Unfortunately, atmospheric flows are characterized by motions which simultaneously vary

on a variety of scales. The spectra of the along wind component rarely shows a well-defined spectral gap. As a result, some motion usually appears on scales which are just larger than the largest transport scales.

The following analysis attempts to partition the variability of the turbulent flux into a) random variability of the flux associated with random location and strength of the transporting eddies, and, b) variation of the flux associated with modulation by larger scale motions. This partitioning is implemented by dividing the record of length 1 hour into nonoverlapping subrecords of width $L = 5$ min. and computing the average flux for each subrecord, symbolized as F_i . The 5 min. subrecord flux, F_i , is decomposed into the record mean 5 min. flux $\langle F \rangle \equiv \langle w'\phi' \rangle$, the linear trend of this flux superimposed upon the record mean, F_{tr} , and the deviation of the 5 min. flux from the linear trend F_i^* , such that

$$F_i = \langle F \rangle + F_{tr} + F_i^* \quad (9)$$

$$F_{tr} = a_0 + a_1 t \quad (10)$$

where t ranges from zero to 1 hour and a_0 and a_1 are the coefficients for the least squares fit. When the 90% confidence interval for the slope a_1 includes zero, the slope is set to zero and the trend is considered to be insignificant.

To assess the random flux errors, we compute the *relative flux error* defined as the ratio of the standard flux error to the mean flux

$$RFE \equiv \frac{\sigma_{F^*}}{|\langle F \rangle| N^{1/2}} \quad (11)$$

where σ_{F^*} is the within-record standard deviation of the random part of the flux, N is the number of subrecords of width L , here equal to 12. Corrections due to dependence between subrecords (Sun and Mahrt, 1994) are not included. At least ten samples of the flux are required to estimate the random flux error while choosing L significantly less than 5 min. would omit too much flux for some records. Nineteen of the 606 records are flagged where RFE exceeds 0.75.

The corresponding measure of nonstationarity is defined as

$$RN \equiv \frac{\sigma_{F_{tr}}}{|\langle F \rangle| N^{1/2}} \quad (12)$$

where $\sigma_{F_{tr}}$ is the standard deviation of the 5 min. flux due to the trend, which can be computed analytically from the slope of the trend, a_1 . Since the random part of the flux, F_i^* , is not significantly correlated with the trend, within a given record, the total variance of F_i is approximately the sum of the random variance and the variance due to the trend. However, the variance due to the random part and trend do tend to be correlated between records. That is, records with large flux trend also have large random variation of the flux. Outlying values of F_i and nonlinear trend could both increase the two variances simultaneously. Records will be flagged when RN exceeds 75%. Five of the 606 records fail this criteria.

If the relative nonstationarity of the flux is large, then RFE can no longer be formally interpreted as the random error which is strictly defined for stationary conditions. RFE is then interpreted more loosely as a measure of the flux variability.

In addition to the flux sampling errors described above, a measure of isolated large flux events is calculated as

$$Event = \frac{Max(F_i)}{|< F >|} \quad (13)$$

where again, F_i is the subrecord flux and $< F >$ the record mean. This parameter is usually highly correlated with RFE , but can significantly differ when the variation of the flux is due mainly to a single event within the subrecord. In this case, $Event$ may be large while RFE may not be large. In other words, $Event$ is a crude measure of the higher moments of the flux while the random flux error is based on the flux variance. Sixty five records are flagged where $Event$ exceeds 2.5.

Applying the criteria for the random and systematic flux errors, the non-stationarity parameter and the $Event$ criteria, 81 out of 606 records are flagged. Some of the records are multiply flagged. In Section 5, statistics of the drag coefficient will be computed with and without the flagged records.

5. Drag coefficient

The value of the drag coefficient depends on many factors including the wind speed, fetch and wave age, stability, method of calculation of the drag coefficient and choice of averaging lengths. It is impossible to sort out these influences without massing an enormous data set, presently not available.

The basic approach here is to display the dependence of the drag coefficient on wind speed for different classes of the other parameters. Unless otherwise noted, the local averaging length is L is 10 min. and the flux averaging scale λ is one hour.

For the weakest wind speed category, the drag coefficient computed from the vector averaged wind is more than twice that computed from the time average of the instantaneous wind (Fig. 6). The speed of the vector averaged wind is reduced by meandering or mesoscale modulation of the wind vector which is important for some weak wind cases. However, most of the cases where the speed of the vector averaged wind is significantly smaller than the speed of the instantaneous wind will be removed by the flux sampling criteria. In the following analysis, the drag coefficient will be computed from the time average of the instantaneous wind.

Removing records which fail flux sampling criteria (Section 4), reduces the drag coefficient at weak wind speeds by a factor of two (Fig. 7, lower panel) but exerts little influence on the drag coefficient at moderate and strong wind speeds. In other terms, some of the largest drag coefficients at weak wind speeds for this particular data are associated with sampling problems. Removing the records which fail flux sampling criteria reduces the standard error for variation of the drag coefficient within the weak wind speed category by a factor of two but has little influence on the standard error for the other wind speed categories. However, even after removing the cases with sampling problems, the standard error for the weak wind speed category is still much larger than that for moderate and strong wind speed categories (Fig. 7, upper panel). The records, which fail the flux sampling criteria, are not included in the remainder of the calculations below.

Fig. 8 shows that the drag coefficient is sensitive to the flux averaging scale only for weak wind speeds. Here modulation or meandering of the stress vector leads to sign reversals and cancellation when averaging the stress components (Section 3). As a result, increasing the flux averaging scale (λ) decreases the value of the drag coefficient at weak wind speeds (Fig. 8).

Much of the decrease of the stress with increasing flux averaging scale λ is due to decreasing importance of the cross wind stress which frequently switches sign. One could argue that nonzero cross wind stress is mainly due to inadequate sample size and should be discarded. However, there appears to be a small systematic cross wind stress. The direction of the stress vector should be closer to the wind shear direction than the wind direction

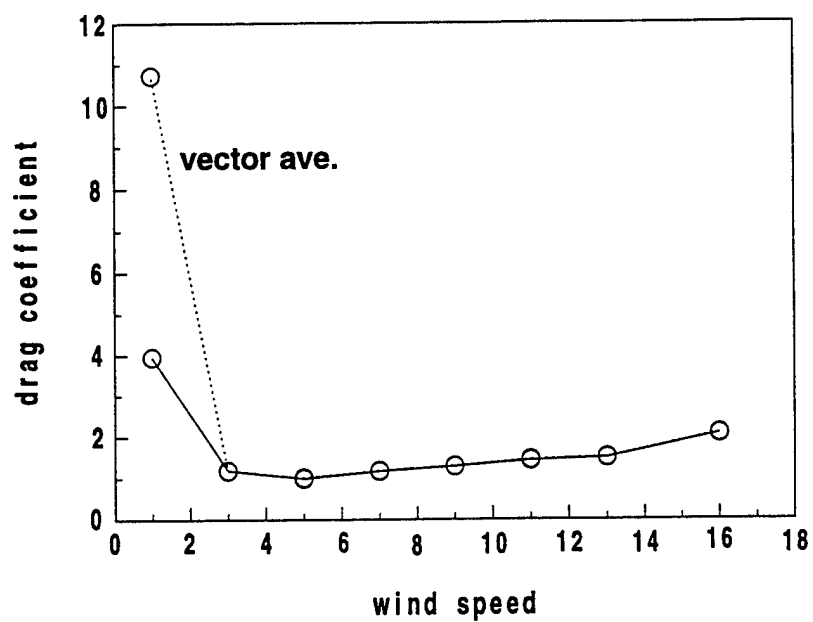


Figure 6: The drag coefficient computed from the average of the instantaneous wind speed (solid line) and the speed of the vector averaged wind (dotted line).

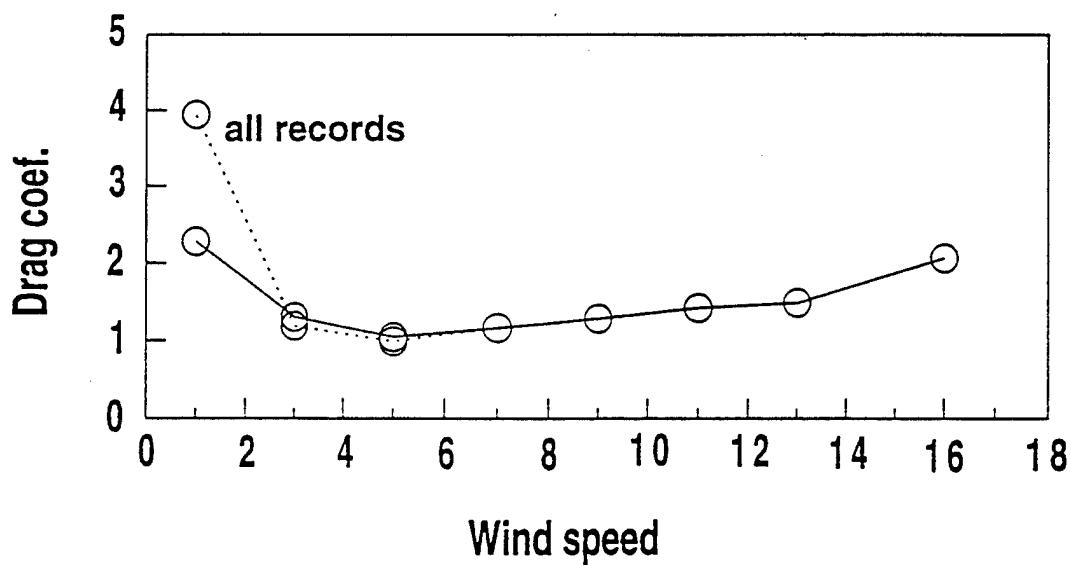
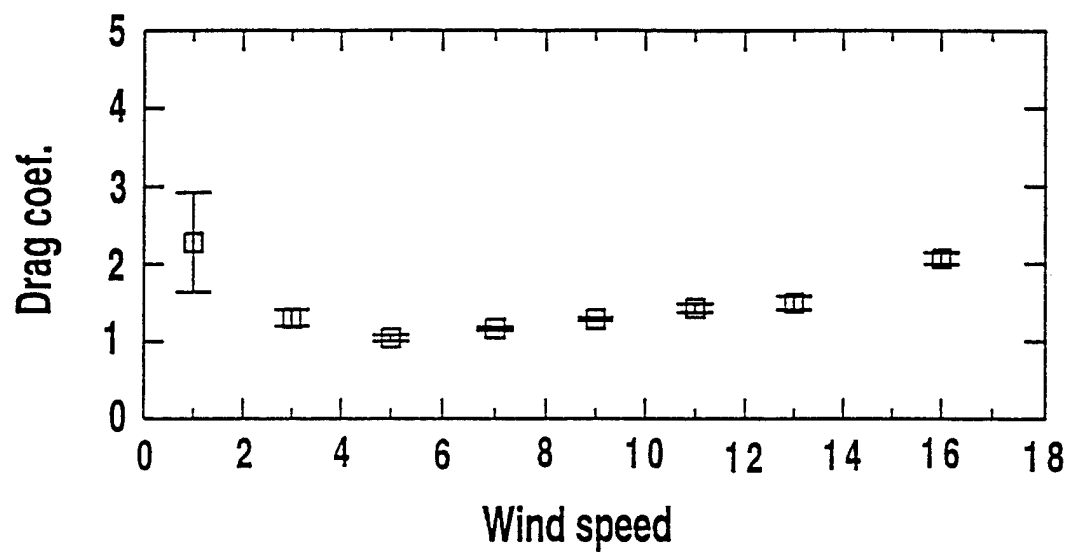


Figure 7: The drag coefficient as a function of wind speed and standard error bars after removing records which fail sampling criteria (upper panel). Comparison of the drag coefficients with (solid line) and without (dashed line) application of sampling criteria.

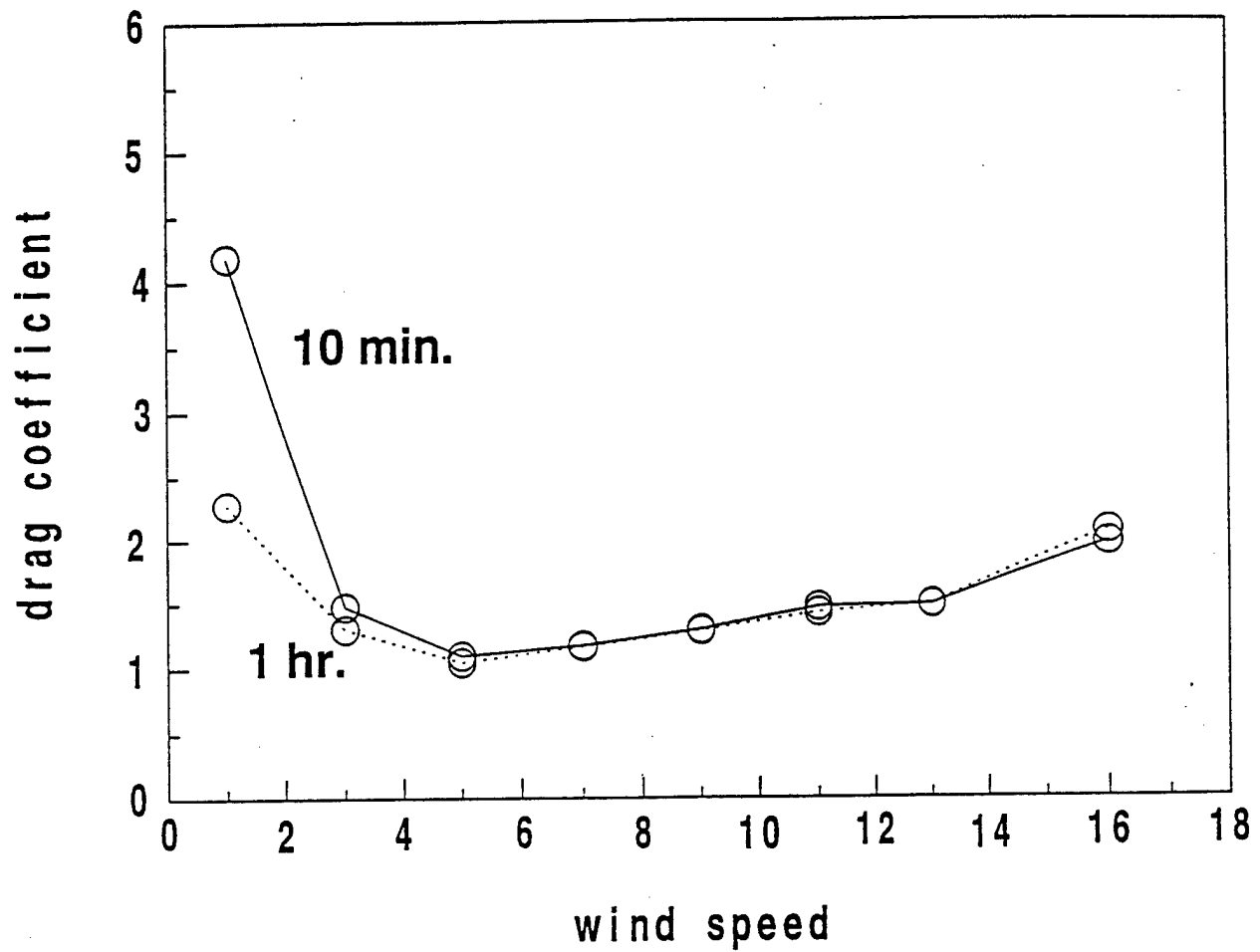


Figure 8: The drag coefficient for $L=10$ min. and $\lambda =60$ min. (solid line) and λ reduced to 10 min. (dotted line) as a function of wind speed.

which is directed to the right of the wind vector for Ekman flow in the Northern Hemisphere. The stress direction is also influenced by stability and baroclinity (Geernaert, et al., 1993) and the direction of the waves (Rieder et al, 1994). Removing the cross wind stress reduces the drag coefficient at weak wind speeds (not shown) but causes little effect at moderate and strong wind speeds. More specifically, the relationship between the wind and stress directions become less systematic at weak wind speeds. During these periods, the along wind stress can even be directed opposite to the wind vector for some records.

Finally, the way the averaging is conducted within each wind speed category influences the average value of the drag coefficient only for the weak wind category. The drag coefficients plotted above are simple averages of the drag coefficient for all of the records within a given wind speed category. As an alternative, the stress magnitude and wind speed were first averaged over all of the records within a given wind speed category and then the drag coefficient was computed from category averages (not shown). This drag coefficient for the weak wind speed category is significantly smaller than the average of the drag coefficient values. Again, the values of the drag coefficients for moderate and strong wind speed categories are not appreciably affected.

The above results collectively indicate that the value of the drag coefficient at weak winds is sensitive to the method used to compute the drag coefficient. In our opinion, there is no one correct drag coefficient for these cases, but rather, the drag coefficient is associated with considerable uncertainty. One can conclude that the drag coefficient increases at weak wind speeds but the exact numerical value of this increase can not be determined. Recognizing this uncertainty, we proceed to examine the dependence of the drag coefficient on wind speed, fetch and stability based on the usual magnitude of the vector averaged stress and the time averaged wind speed. The local averaging scale L will be 10 min. and the flux averaging scale λ will be one hour.

6. Dependence on stability and wind direction

The historical literature (Introduction) as well as the present data (Fig. 8) suggest that the drag coefficient reaches a minimum value for mean wind speeds near $4 - 5 \text{ ms}^{-1}$. However, in the present data set, most of the weak

winds are blowing from land and part of the enhancement of the drag coefficient at weak winds could be due to fetch limited growing waves. Asymmetric wave profiles resulting from near-resonant nonlinear wave-wave interactions in shallow water may also be important. However, some of the short fetch cases are associated with thin internal boundary layers in which case the drag coefficient may be quite different from that predicted from similarity theory. To investigate the influence of fetch, the records are divided into a long fetch class (>15 km, between 225° and 340°) and a short fetch class (< 4 km, between 120° and 220°). In general, the drag coefficient for the short fetch flow is indeed greater than that for the flow with long fetch (Fig. 9) particularly at stronger wind speeds where the averaged short fetch drag coefficient is more than 50% than the averaged long fetch value. At these strong wind speeds, the flux sampling errors are generally small. The effect of stability on the drag coefficient is expected to be small at stronger wind speeds, as is suggested by the drag coefficients which were reduced to neutral stability (Fig. 9) using similarity theory (Geernaert et al., 1986). Therefore differences in the wave field and associated roughness seem to be the most likely explanation for the greater drag coefficients with short fetch. Here, short fetch presumably corresponds to wave age values which are small compared to 10, in which case fetch limited conditions are expected to lead to increased surface drag coefficient (Nordeng, 1991).

Notice that the difference between the short and long fetch drag coefficients increases with wind speed. Although the long fetch cases are still fetch limited in contrast to open ocean, this general result might be related to the overall conclusion of Geernaert (1990, Fig. 8) which shows that near coastal or lake drag coefficients are larger than open ocean drag coefficients, and, that the difference between the two cases tends to increase with wind speed. The numerical values of the drag coefficients in RASEX for both the short and long fetch cases are closer to the near coastal values than the open ocean values summarized in Fig. 8 of Geernaert (1990). Geernaert (1990) emphasized the differences in water depth as a cause of different values of the drag coefficient between the different observations. Water depth could also be a factor with the RASEX data even though the observations are from a fixed platform. With offshore winds, the footprint of the flux measurements are upstream over shallower water and vice versa.

The drag coefficient for the short fetch class is large in spite of some very small individual values associated with advection of warm air from land.

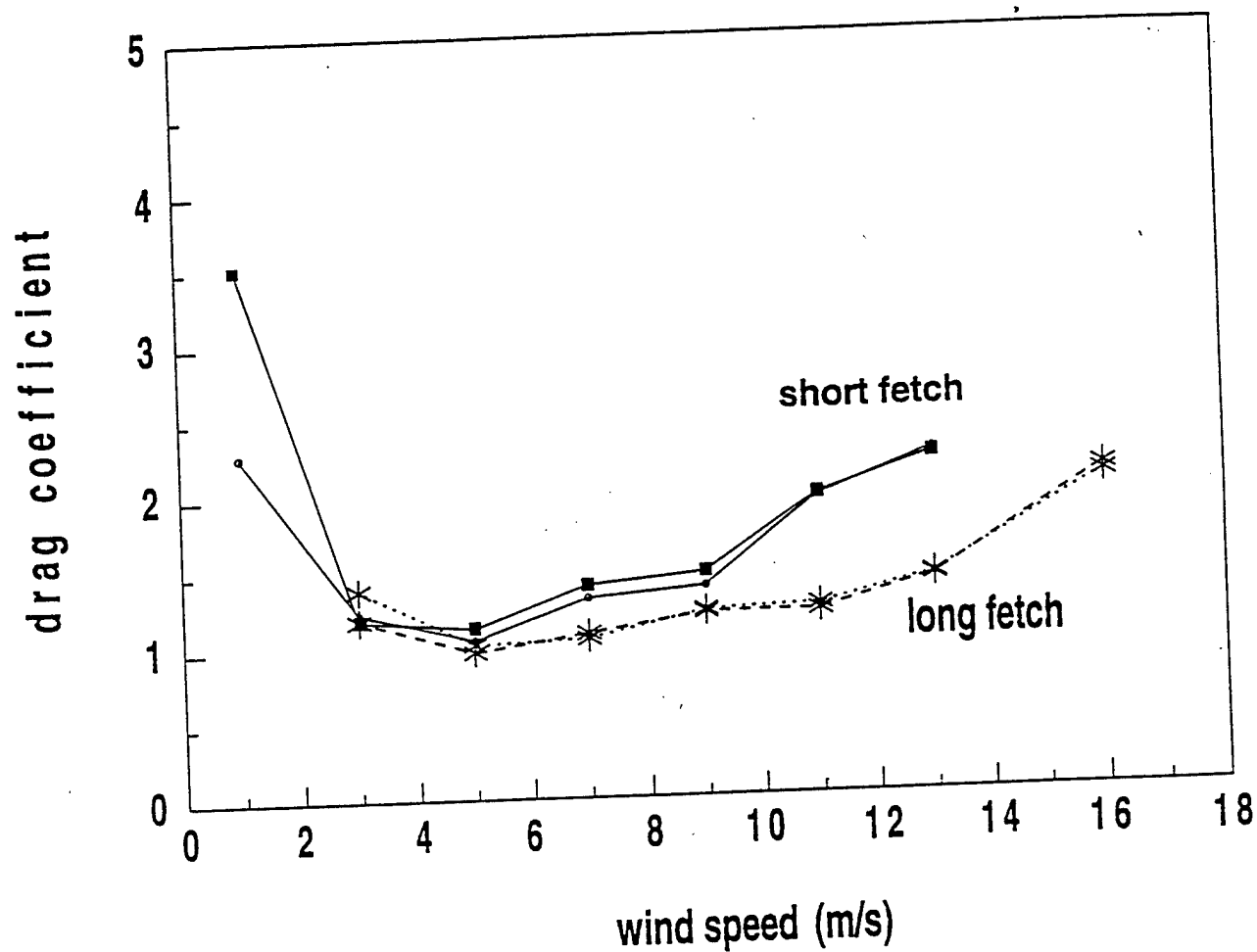


Figure 9: The drag coefficient for the short (solid line with circles) and long fetch (dotted line with asterisks) records and the corresponding values reduced to neutral conditions (solid line with squares for short fetch; dashed line with x's for long fetch).

With significant warm air advection, stable stratification leads to partial collapse of the surface stress and increase of stress with height. This advective internal boundary layer is not described by similarity theory.

The increase of the drag coefficient for weak winds is much greater for the unstable class of records (upward virtual heat flux) than for the stable class of records (comparison not shown). However reducing the value of the drag coefficient to its neutral value does not significantly close the gap between the two classes of data. That is, the neutral drag coefficient reduced from the unstable class of records is still significantly larger than the neutral drag coefficient reduced from the stable class of records, even after subdividing the records according to fetch. Furthermore, the neutral value of the drag coefficient is still correlated with stability ($-z/L$), particularly for unstable flow with long fetch. As one final test of the effectiveness of reducing the drag coefficients to neutral values, the drag coefficient was modeled with a least squares dependence on wind speed. Using values of the drag coefficient which were reduced to their neutral values did not increase the variance explained by the modelled dependence of the drag coefficient on wind speed, as compared to the regression model using the original drag coefficients.

One explanation is that existing similarity theory is generally inadequate which will be examined in a future study. An alternative explanation is that the heat and momentum fluxes are relatively small at weak winds so that the relative flux errors are large. Then the computation of the Obukhov length and reduction of the drag coefficient to the neutral value suffer large errors at weak wind speeds while the stability correction is generally unimportant at strong wind speeds.

7. Conclusions

Analysis of RASEX data shows that the drag coefficient for weak winds is sensitive to the method used to calculate the drag coefficient. The value of the drag coefficient at moderate and strong wind speeds is not sensitive to the method of calculation provided that the computed perturbation flow includes all of the transporting scales. More specifically, *the following tendencies were observed for the class of weak wind records but were not observed for the moderate and strong wind classes:*

- 1) The computed drag coefficients for the weak wind cases are larger

when the wind speed is computed from the vector averaged wind (analogous to numerical models) compared to averaging the instantaneous wind speed.

2) Flux sampling criteria eliminate a significant fraction of the weak wind cases; however, the standard error still remains significantly larger than that for moderate and strong wind classes. Rotation of the coordinate system to reduce the influence of inadvertent tilt of the sonic anemometer significantly affects the drag coefficient for weak wind cases.

3) The computed drag coefficient is smaller when the flux is averaged over longer time periods due to meandering of the stress vector and cancellation associated with sign switches.

4) For a few weak wind cases, inclusion of the current velocity in the calculation of the relative surface wind significantly affects the value of the drag coefficient.

5) The wind and stress vectors are generally not aligned for weak wind cases.

6) The difference between the stress values estimated from profiles and estimated from eddy correlation showed the greatest differences for the weak wind case.

Regardless of the method of calculation, the drag coefficient shows some increase at weak wind speeds. It is not known if the increase of the drag coefficient at weak wind speeds can be associated with the smooth flow physics of Liu et al (1979), increased roughness associated with capillary waves (Wu, 1994), increased role of surfactants at weak winds, or greater nonequilibrium between the wind and wave field due to larger relative influence of flow meandering. The drag coefficient also increases with increasing instability and decreasing fetch. After attempting to remove the influence of stability by reducing the drag coefficients to their neutral values using conventional similarity theory, significant dependence on stability remains. In fact, reducing drag coefficients to neutral values had a much smaller influence than eliminating records with large flux sampling errors. A future study will attempt to isolate these various influences as well as wave age and shoaling through

inclusion of the wave wire data and independent estimates of the surface stress from wind profiles.

The large scatter in the drag coefficient at weak winds in the present study contrasts with the data from Geernaert et al. (1988) and Bradley et al. (1991) appearing in Wu (1994) where the scatter at weak winds was small. Those values of the drag coefficient were computed from the dissipation technique. However, the dissipation technique has not been calibrated for the case of very weak winds and Geernaert et al. (1988) points out that the usual dissipation technique is successful when the flow is near neutral and stationary. For the RASEX data, both of these conditions are violated more frequently for weak wind cases. The direct eddy correlation measurements show large scatter at weak winds and the drag coefficient can vary by a factor of three due to method of calculation. This uncertainty masks any attempts to differentiate between the smooth and rough flow predictions (Wu, 1994) and also precludes testing the dissipation method for the weak wind case.

We recommend that examination of the drag coefficient at weak wind speeds should always include sensitivity to the method of calculation, choice of averaging scale and assessment of nonstationarity. In the present study, the flux averaging scale was chosen partly by consulting the scale dependence of the correlation between the mean flow and momentum flux.

Acknowledgments: This work is supported by grants N00014-93-1-0360 and N00014-93-1-0274 from the Office of Naval Research. The extensive comments of Michael Freilich, Jielun Sun, Chris Fairall and Tetsu Hara, and the data assistance of Michael Courtney are greatly appreciated.

References

- Banner, M. L., The influence of wave breaking on the pressure distribution in wind-wave interactions, *J. Fluid Mech.*, 211, 463-495, 1990.
- Barthelmie, R. J., M. S. Courtney, J. Højstrup, and P. Sanderhoff, The Vindeby Project: A Description. Report R-741(EN), Risø National Laboratory, DK4000, Roskilde, Denmark, 1994.
- Beljaars, A.C., 1995: The parametrization of surface fluxes in large scale models under free convection. To appear in *Quart. J. Roy. Met. Soc.*

- Bradley, E. F., P. A. Coppin, and J. S. Godfrey, Measurements of sensible and latent heat flux in the Western Equatorial Pacific Ocean, *J. Geophys. Res.*, 96, 3375-3389, 1991.
- Donelan, Mark, Air-sea interaction, *Ocean Engineering Science*, B. Le Mehaute and D. M. Hanes, Eds. John Wiley and sons, 239-291, 1990.
- Emanuel, K. A., On the dynamical definition(s) of "mesoscale", *Mesoscale Meteorology - Theories, Observations and Models*, D. K. Lilly and T. Gal-Chen, Reidel, 1-12, 1983.
- Freilich, M. H. R., R. T. Guza, and S. L. Elgar, Observations of nonlinear effects in directional spectra of shoaling gravity waves, *J. Geophys. Res.*, 95, 9645-9656, 1990.
- Freilich, M.H. R., and R. T. Guza, Nonlinear effects of shoaling surface gravity waves, *Phil. Trans. R. Soc. Lond.*, A311, 1-41, 1984.
- Geernaert, G. L., Measurements of the angle between the wind vector and wind stress vector in the surface layer over the North Sea, *J. Geophys. Res.*, 93, 8215-8220, 1988.
- Geernaert, G. L., Bulk parameterizations for the wind stress and heat fluxes, *Surface Waves and Fluxes. Vol. 1 - Current Theory*, 91-172, G. L. Geernaert and W. J. Plant, Eds., Kluwer, 1990.
- Geernaert, G. L., Katsaros, K. B. and K. Richter, Variation of the drag coefficient and its dependence on sea state, *J. Geophys. Res.*, 91, 7667-7679, 1986.
- Geernaert, G. L., S. E. Larsen, and F. Hansen, Measurements of the wind stress, heat flux and turbulence intensity during storm conditions over the North Sea, *J. Geophys. Res.*, 92, 13,127-13,139, 1987.
- Geernaert, G. L., K. L. Davidson, S. E. Larsen, and T. Mikkelsen, Wind stress measurements during the Tower Ocean Wave and Radar Dependence Experiment, *J. Geophys. Res.*, 93, 13,913-13,923, 1988.
- Geernaert, G. L., F. Hansen and M. Courtney, Directional attributes of the ocean surface wind stress vector, *J. Geophys. Res.*, 98, 16571-16582, 1993.

- Greenhut, G. and S.J.S. Khalsa, Bulk transfer coefficients and dissipation-derived fluxes in low wind speed conditions over the western equatorial Pacific Ocean. *J. Geophys. Res.*, 100, 857-863, 1995.
- Godfrey, J. S., and A. C. M. Beljaars, On the turbulent fluxes of buoyancy, heat and moisture at the air-sea interface at low wind speeds, *J. Geophys. Res.*, 96, 22,043-22,048, 1991.
- Hauf, Thomas, and T. L. Clark, Three-dimensional numerical experiments on convectively forced internal waves, *Quart. J. Roy. Met. Soc.*, 115, 309-333, 1989.
- Højstrup, J., J. Edson, J. Hare, M. S. Courtney, P. Sanderhoff, The RASEX 1994 experiments, Risø-R-788, Risø National Laboratory, Roskilde, Denmark (ISBN-87-550-2039-9), 1995.
- Howell, J. F., and L. Mahrt, An adaptive multiresolution data filter: applications to turbulence and climatic time series, *J. Atmos. Soc.*, 51, 2165-2178, 1994.
- Kitaigorodskii, S. A., *The physics of air-sea interaction*, translated from Russian, Israel Program for Scientific Translations, Jerusalem, 273 pp., 1973.
- Large, W. G., and S. Pond., Open ocean momentum flux measurements during moderate to strong winds, *J. Phy. Oc.*, 11, 324-336, 1981.
- LeMone, M. A., The structure and dynamics of horizontal roll vortices in the planetary boundary layer, *J. Atmos. Soc.*, 33, 1308-1320, 1973. .
- Lilly, D. K., Mesoscale variability of the atmosphere, *Mesoscale Meteorology - Theories, Observations and Models*, D. K. Lilly and T. Gal-Chen, Reidel, 13-24, 1983.
- Maat, N., C. Kraan, and W. A. Oost, The roughness of wind waves, *Boundary-Layer Meteorol.*, 54, 89-103, 1991.
- Mahrt, L., and J. F. Howell, The influence of coherent structures and microfronts on scaling laws using global and local transforms, *J. Fluid Mech.*, 260, 247-270, 1994.

- Mahrt, L., and Wayne Gibson, Flux decomposition into coherent structures, *Boundary-Layer Meteorol.*, 60, 143-168, 1992.
- Mahrt, L., and J. Sun, Multiple velocity scales in the bulk aerodynamic relationship for spatially averaged fluxes. To appear in *Month. Wea. Rev.*, 1995.
- Mortensen, N. G. and J. Højstrup, 1995, The Solent sonic: response and associated errors. To be submitted to *J. Atm. and Oceanic Tech.*
- Mourad, Pierre D., and R. A. Brown, Multiscale large eddy states in weakly stratified planetary boundary layers, *J. Atmos. Soc.* 47, 414-438, 1990.
- Nordeng, T. E., On the wave age dependent drag coefficient and roughness length at sea, *J. Geophys. Res.*, 96, 7167-7174, 1991.
- Pierson, W. J. Jr., The measurement of the synoptic scale wind over the ocean, *J. Geophys. Res.*, 88, 1683-1708, 1983.
- Plant, W. J., A relationship between wind stress and wave slope. *J. Geophys. Res.*, 87, 1961-1967, 1982.
- Rieder, K. F., J. A. Smith, and R. A. Weller, Observed directional characteristics of the wind, wind stress and surface waves on the open ocean, *J. Geophys. Res.*, 99, 22,589-22,596, 1994.
- Smedman, A.-S., M. Tjernström, and U. Hogström, Near-neutral marine atmospheric boundary layer with no surface shearing stress: A case study, *J. Atmos. Soc.*, 51, 3399-3411, 1994.
- Smith, S. D., Wind stress and heat flux over the ocean in gale force winds, *J. Phy. Oc.*, 10, 709-726, 1980.
- Smith, S. D., R. J. Anderson, W. A. Oost, C. Kraan, N. Maat, J. Decosmo, K. B. Katsaros, K. L. Davidson, K. Bumke, L. Hasse, and H. M. Chadwick, Sea surface wind stress and drag coefficients: The HEXOS results, *Boundary-Layer Meteorol.*, 60, 109-142, 1992.
- Sun, J., and L. Mahrt, Spatial distribution of surface fluxes estimated from remotely sensed variables, *J. Appl. Meteor.*, 33, 1341-1353, 1994.

- Sun, J., L. Mahrt, S. K. Esbensen, J. Howell, C.M. Greb, R. Grossman and M. A. LeMone, Scale dependence of air-sea fluxes over the Western Equatorial Pacific, submitted to *J. Atmos. Soc.*, 1995.
- Toba, Y., N. Iida, H. Kawamura, N. Ebuchi, and I. S. F. Jones, Wave dependence of sea-surface wind stress, *J. Geophys. Res.*, 20, 705-721, 1990.
- Wu, Jin, The sea surface is aerodynamically rough even under light winds, *Boundary-Layer Meteorol.*, 69, 149-158, 1994.

ROUGHNESS LENGTHS IN COASTAL TERRAIN

Jørgen Højstrup

Meteorology and Wind Energy Department
Risø National Laboratory
Roskilde, Denmark

1. INTRODUCTION

The roughness lengths relevant for shallow water coastal areas will be discussed, mainly from the viewpoint of wind energy and proper siting of wind turbines.

We have seen increasing planning and environmental problems with the siting of wind turbines on land, and consequently it may be necessary to place wind turbines offshore in the future. The world's first offshore windfarm has been in operation in Denmark for some years now, and we know that the cost of offshore windfarm installations is significantly higher than for their land-based counterparts. The windspeed is also higher at sea and since the wind resource varies as the windspeed cubed we need to be able to assess the offshore windspeeds with good accuracy. Reliable tools are available for the estimation of the wind resource for open sea conditions, but the most likely sites for offshore windfarms are in near-coastal areas, where the windspeeds are diminished by the influence of the nearby rough land surface.

The general characteristics of the offshore wind climate is somewhat different from the onshore situation. The rather small values of roughness encountered at sea are responsible for higher windspeeds and reduced turbulence intensities. Both of these factors are beneficial for wind energy, the higher windspeeds of course makes it possible to produce more energy and the lower turbulence levels create less fatigue damage in the wind turbines and increase their lifetime. For coastal areas we see some complicating factors influencing these parameters:

- The surface roughness of the sea is quite well known for open ocean conditions, but in the near-shore situation we can expect somewhat different (higher) values because of changed wave structure with breaking and refracting waves near the coast.
- Wind from shore will need some time to accelerate in response to the lower sea roughness. Which distance from the coast comprises a reasonable balance between the increased cost and the increased windspeed?
- Atmospheric stability effects on the wind profiles are different from the land situation, how does this affect the wind resource?

In the following we will concentrate on the first

problem, the surface roughness, concentrating on neutral conditions. The second problem was discussed in Højstrup et al (1994). The last question has been dealt with in detail recently by Barthelmie et al (1994). Results from measurements from a coastal site and from an offshore site will be used.

2. ROUGHNESS LENGTHS AT SEA

Over land, the surface roughness can usually be assumed to have little variation with windspeed attaining values from 0.01m to 0.1m for the types of terrain usually of interest for wind energy purposes.

At sea the situation is much more complicated. The roughness is very small at low windspeeds but increases then rapidly with increasing windspeed. A very simple description of this behavior was derived by Charnock (1954) and is still in widespread use:

$$z_0 = A \frac{u_*^2}{g} \quad (1)$$

where z_0 is the surface roughness, u_* the surface friction velocity, g acceleration of gravity and A a constant. In neutral conditions the windspeed variation with height can be described using the logarithmic wind profile:

$$U = \frac{u_*}{k} \ln \frac{z}{z_0} \quad (2)$$

where z is the height over ground and k the von Karmann constant.

Using the eq.2 to eliminate u_* , we obtain

$$z_0 = \frac{Ak^2}{\ln \frac{z}{z_0}} U^2 \quad (3)$$

From this implicit equation for z_0 it is obvious that we have a very rapid variation of the roughness with windspeed.

Normally accepted values for the "constant" A are 0.011 for open ocean and a somewhat higher value 0.018 for near coastal conditions. These values then result in a variation of roughness length over three orders of magnitude for a normal range of windspeed

variations: Roughness lengths 10^{-5} - 0.001 m (4-25 m/s).

We shall employ three methods for the derivation of roughness lengths from measurements:

- 1) WINDPROFILE. Using windspeed measurements at two levels and eq. 2.
- 2) TURBULENCE INTENSITY. Using the standard deviation of windspeed variations as a measure of u_* at one level together with the mean windspeed to obtain z_0 from eq.2

The turbulent intensity, defined as the ration of standard deviations of windspeed fluctuations to the average windspeed (typical averaging times of 10-30 minutes) can for neutral conditions be written as a function of the surface roughness only, assuming that windspeed standard deviations vary proportionally with u_* (the constant of proportionality happens be about 2.5, see Panofsky and Dutton (1984) cancelling out the von Karmann constant here taken as 0.4):

$$I = \frac{\sigma_u}{U} = \frac{\sigma_u}{u_*} \frac{k}{\ln(\frac{z}{z_0})} = \frac{1}{\ln(\frac{z}{z_0})} \quad (4)$$

- 3) DRAG COEFFICIENT. From direct measurements of U and u_* we can derive z_0 from eq.2.

These three ways of calculating the roughness length from measurements are not necessarily directly comparable. Each of them will be influenced differently by upstream inhomogeneities, they have different "footprints", and they also exhibit different sensitivities to the accuracy of the instrumentation involved.

3. MEASUREMENTS

We will consider measurements from two sites

- 1) Nibe, a north-south running coastline with a shallow fjord to the west with 5-20 km fetch over water, see fig.1. Data were selected from the 56m tower in a 90° West-sector and a 90° East sector. 12 years of 10 minute average values (four each hour) were used.
- 2) Vindeby, the offshore windturbine site, with two 48m offshore towers at varying distances from the shoreline, and one 48m tower just on the shoreline (fig.2). Neutral data were selected from a 90° sector to the west of the tower situated west of the windfarm, depth of the water approx. 4m. The site and instrumentation were described in Barthelmie et al (1994). Upstream fetch was 10-20km over water depths of 5-20m. We had about one year of 30 minute averages. Data from the two RASEX intensive campaigns at the same site were also used (Højstrup et al, 1994).

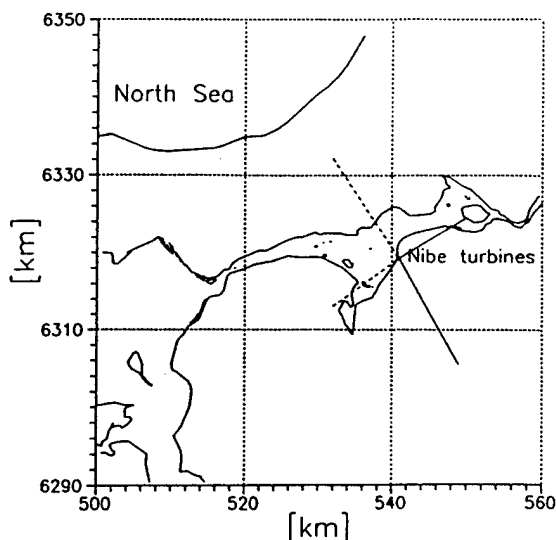


Figure 1 The Nibe site. The full lines indicate the winddirection sector with over land fetch. The dashed lines the corresponding over water fetch.

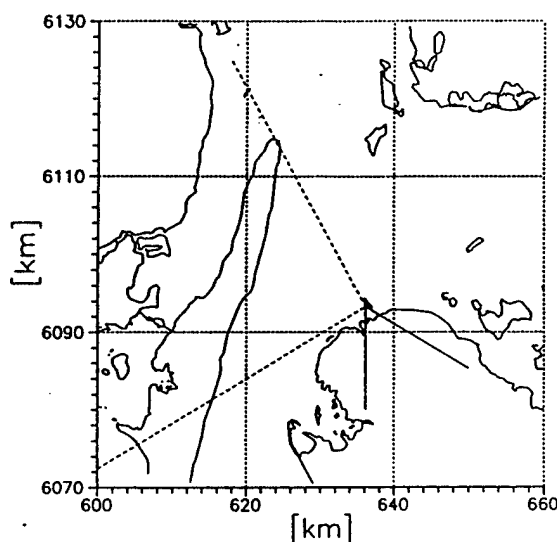


Figure 2 The Vindeby/RASEX site. Full lines indicate short fetch sector (2km), dashed lines the long fetch sector (15-20km).

4. RESULTS

4.1. Profile and turbulence intensity methods

Roughness lengths have been calculated using eqs. 2 and 4. The results from the two sites are shown in figs. 3 and 4. Fig.3 shows results from Nibe for the profile and the turbulence intensity methods for flow from the fjord (West) and for flow from the East for comparison.

The results from flow from the East are similar for the two methods, resulting in roughness lengths of

approx. 0.02m as expected. At low windspeeds we see some differences with higher values for the turbulence intensity method, probably due to the influence of instationarities and "fossil" turbulence.

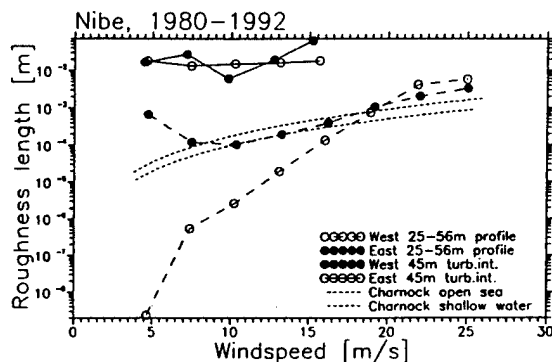


Figure 3 Nibe roughness lengths derived from profiles and turb.int. The full lines are over land fetches, the dashed lines indicate over water fetch. The Charnock expression are shown for comparison.

The results from the onshore flow comes out quite differently for the two methods, the profile methods shows very small values at low windspeeds increasing rapidly with windspeed to about 0.01m at 25m/s. The turbulence intensity method shows variation more similar to the Charnock expressions also shown on the graph. The low windspeed increase must again be assumed to be caused by instationarities and "fossil" turbulence as mentioned above.

In fig.4 are shown the same type of results from the offshore site, and we see results qualitatively similar to the coastal site.

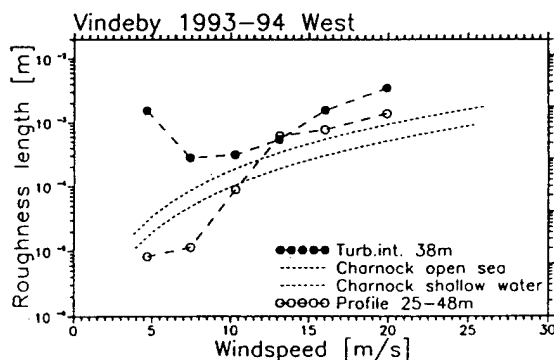


Figure 4 Roughness lengths from the Vindeby West mast, derived from profiles ('1') and turb.int. ('2'), compared with the Charnock expression.

For a more limited dataset (approx. 2000 sets of 30min. timeseries) from the RASEX experiment we have selected neutral data from two different fetch situations, about 20km fetch from the West, and about two km fetch from the Southeast.

For the long fetch we see the same type of behavior as seen from the two previous data sets, but the short fetch situation looks quite differently

showing consistently very low values for the roughness derived from the profile.

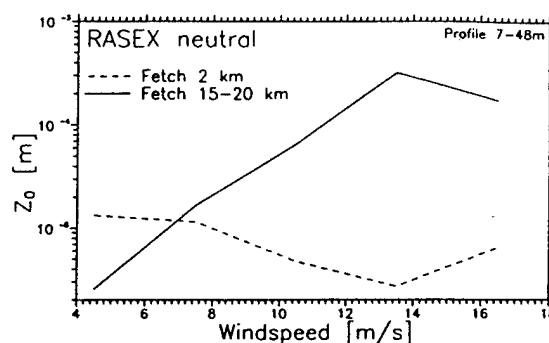


Figure 5 Roughness lengths calculated from windprofiles from the RASEX experiments. Full line is 15-20km fetch. Dashed line 2km fetch

4.2. Drag coefficient method

Direct measurements of stress were available only from the RASEX data, and the results are shown in fig.6 together with the results from the profile method and for comparison the Charnock values are also shown. The stress measurements at 3m were used.

The long fetch data are quite well described by the Charnock expression, whereas the short fetch data at windspeeds below 10m/s are about two orders of magnitude smaller.

5. DISCUSSION

For simplicity we relate all the results to the Charnock values. The apparent roughness lengths from the profile methods for long fetches are much lower than expected, most so for the coastal site. The reason for this behavior is possibly that approaching the coast the structure of the waves change and they eventually break even at low windspeeds, and are less efficient in taking energy from the wind, resulting in less stress near the waves, in turn resulting in a windprofile with less steepness meaning that the apparent roughness length becomes smaller. The importance of this effect is of course largest close to

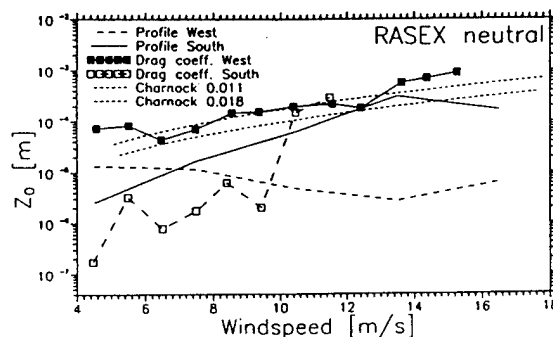


Figure 6 Roughness lengths calculated from profiles and drag coefficients.

the coast. At high windspeeds the waves are much larger and bottom friction takes more energy out of the waves offsetting effect of the waves breaking, and we do indeed see behavior reasonably well described by the Charnock relation at high windspeeds.

The apparently very low roughness lengths for the short fetch situation could be caused by internal boundary layer distortion of the windprofile. In fig. 7 is shown a windprofile where the effect has been artificially exaggerated to better illustrate the point. When the wind speeds up, we do not see a simple smooth adjustment between the upstream and downstream equilibrium profiles. The higher order closure models show that the profiles exhibit an inflection point in the adjustment zone, meaning that if the lowest level windspeed used to calculate the roughness length is situated in this zone, then we will see a somewhat diminished average windspeed gradient, which of course results in seemingly lower roughness length.

The low values of the drag coefficient for the short fetch situation is a result of the smaller waves resulting from flow off land (fig.8). At higher windspeeds there seems to be a tendency towards the same curve for both the drag coefficient values (fig.6) and the wave heights. However the amount of data available from high windspeeds situations in this dataset were not sufficient to more than indicate the probable behavior.

There are less assumptions involved in the profile method, and this method is probably most accurate, but poses also grave requirements for accurately calibrated velocity sensors at several levels, undisturbed by local terrain features. The turbulence intensity method seems to give reasonable results at high windspeeds where the roughness attains larger values. The profile and turbulence intensity methods seem to agree very well over land (fig.3). The lower turbulence levels over water seem to be much more sensitive to the more frequent occurrence of insensitatory situations at low windspeeds causing large velocity standard deviations.

ACKNOWLEDGEMENTS

The measurements at Nibe were supported by the Danish Ministry of Energy. The measurements and analysis of Vindeby data were supported by the EU, contracts J0U2-CT93-0325 and J0U2-CT93-0350 and by ELKRAFT. The RASEX experiments were supported by ONR, contract N00014-93-1-0360.

REFERENCES

Barthelmie, R.J., D.Melas, J.Højstrup, M.S.Courtney, 1994: Modification of the offshore coastal wind field. Second International Conference on Meteorology and Air/Sea Interaction of the Coastal Zone. Lissabon Sept. 1994, American Meteorological Society.

Barthelmie, R.J., M.S.Courtney, J.Højstrup, P.Sanderhoff, 1994: The Vindeby Project: A description. Risø-R-741, Risø National Laboratory, Roskilde, Denmark.

Charnock, H., 1955: Wind stress on a water surface. Quart. J. R. Meteorol. Soc., 81, 639-640.

Højstrup, J., J.Edson, J.Hare, M.S.Courtney and P.Sanderhoff, 1995: The RASEX 1994 experiments. Datareport. Risø-R-788, Risø National Laboratory, Roskilde, Denmark.

Højstrup, J., R.J.Barthelmie, M.S.Courtney, 1994: Preliminary results of Offshore Meteorological Monitoring at the Vindeby Windfarm. In proceedings from: European Seminar on Offshore Wind Energy in the Mediterranean and other European Seas, Rome March 1994.

Panofsky, H.A. and J.A.Dutton, 1984: Atmospheric Turbulence: Models and Methods for Engineering Applications. Wiley-Interscience, New York.

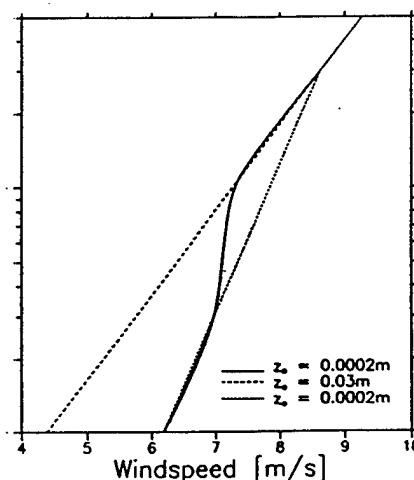


Figure 7 Rough-to-smooth windprofile. Inflection point exaggerated.

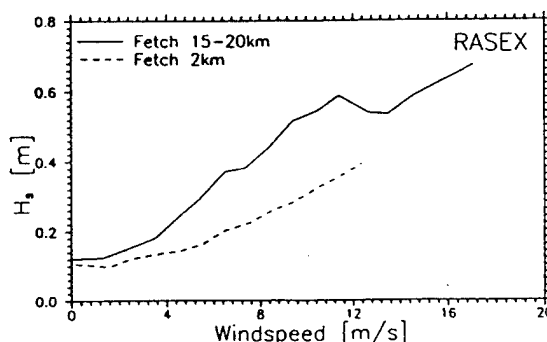


Figure 8 Significant wave heights for long and short fetch situations.

Quality control and flux sampling problems : Application to RASEX

Dean Vickers and L. Mahrt

5 December 1995

1 Introduction

The long term goal of this work is to develop an overall strategy for pre-analysis of tower and aircraft data. This document motivates and describes techniques to calibrate, quality control and evaluate various flux sampling problems for RASEX tower data. The instrumentation section describes the RASEX experiment. The calibration section applies known corrections to the data. The quality control section outlines a large number of checks which flag abnormal behavior and potential instrument problems, and the flux sampling section describes measures of sampling errors. The remaining sections present the results for RASEX.

The quality control and flux sampling assign flags to records. *Hard flags* identify physically unlikely abnormalities which may be instrumental or data recording problems. *Soft flags* identify unusual behavior which is physically plausible but might be removed for certain calculations or reserved for special studies. Such behavior might include unusual vertical structure associated with an internal boundary layer or near surface inversion, microscale fronts, mesoscale modulation and nonstationarity.

Unfortunately, there is no systematic method for categorically distinguishing between instrumental problems and unlikely but possible physical behavior. For example, electronic noise can produce spikes which might have a similar amplitude to rare fine scale fluctuations. Spike removal criteria can be formulated in terms of a certain number of standard deviations from the

mean, or some other statistical properties, however the statistical properties themselves might be contaminated by the instrumental spikes. Then applying the same criteria to two records would leave more spikes in the record which initially contained more spikes. This study considers a variety of time series characteristics, or "trouble shooting" parameters which attempt to identify instrumentation problems. The selection of the numerical value of these critical parameters is based on frequency distributions for RASEX and inspection of records, but remains somewhat arbitrary. Inspection of the individual records is required for verification of instrumental problems.

2 RASEX instrumentation

The full RASEX experiment instrumentation is described in Barthelmie et.al. (1994) and Højstrup et. al. (1995). In this study we consider 10 hertz observations from Gill/Solent Ultrasonic sonic anemometers at the 10 and 32 m levels on the sea mast west tower for estimating the wind speed, wind stress and sensible heat flux. Data were collected during two intensive campaigns in the spring and fall of 1994. Also included are cup anemometer wind speed measurements at the 7,15,20,29,38,43 and 48 m levels on the tower, wind direction at the 20 and 43 m levels, atmospheric temperature difference measurements, sea surface radiative temperature, 10 m absolute air temperature, precipitation and water currents.

The sea mast west tower is located 2 km off the coast of Denmark in 4 meters of water in a generally high wind speed regime. Winds from 120 through 150 degrees have a short fetch (2 km), winds from 150 through 240 have mixed fetch (2 to 5 km) and winds from 240 through 340 have long fetch (15 to 60 km). Wind directions between 340 and 120 degrees are discarded from this analysis because of upwind interference from the tower and a wind generator farm.

Our analysis of the RASEX tower data considers 1 hour data records. The choice of 1 hour for the record size is supported below in the discussion of flux sampling errors. The sonic anemometer fields of three dimensional winds and virtual temperature are recorded at a 10 Hz frequency, resulting in 36,000 data points per record. For all other quantities, only the 1 hour statistics are considered. The spring data set consists of 63 records and the

fall set 546 records, for a total of 609 1 hour records.

3 Calibration

The following calibrations are known and applied to the RASEX data.

1. The virtual temperature from the sonic anemometer is corrected for the bending of the acoustic signal by the cross wind by applying the method of Højstrup and Mortensen (1995).

2. To correct for the tilt of the sonic anemometer, a single set of tilt angles for each sonic were computed using the entire data set. Using 30 minute mean values, the vertical motions for the entire observational period were fit in a least squares sense to the equation

$$w = a + bu + cv. \quad (1)$$

The regression coefficients b and c estimate the dependence of the “measured” vertical velocity on the two measured horizontal velocity components due to tilt of the sonic anemometer from true vertical. The calculation of corrected sonic velocity components are constructed by subtracting the value a and rotating the coordinate system such that the statistical influence of $bu + cv$ vanishes. This transformation of the coordinate system puts the regression prediction in the horizontal plane such that applying Eq.(1) in a least squares sense to the corrected rotated data would yield $a = b = c = 0$.

3. The absolute air temperature and temperature differences are calibrated according to Højstrup (1995), personal communication.

4. The surface radiative temperature from the infrared instrument is obtained assuming an emissivity of water equal to one.

After calibration, the horizontal wind components for each record are rotated into the mean wind direction such that the mean along-wind component is positive and the mean cross-wind component is zero. The rotation is:

$$u_r = u \cos(\xi) + v \sin(\xi) \quad (2)$$

$$v_r = u \sin(\xi) - v \cos(\xi) \quad (3)$$

$$\xi = \arctan(< v > / < u >) \quad (4)$$

where u and v are the unrotated wind components, u_r and v_r are the rotated ones, and the averaging operator $< >$ indicates an average over the record. For all the analysis that follows, the rotated components are used.

4 Quality control

In this section we present parameters which describe different aspects of the data. Threshold values for these parameters have been specified to identify records which might be removed because of instrument problems or selected for special study. These values are determined from frequency distributions of the parameters themselves and visual inspection of the individual records. The generality of the usefulness of the following package, which is based on RASEX tower data, to other data sets is not known.

4.1 Resolution

For some records with very weak variance (weak winds, stable conditions), the resolution of the recorded data is not small compared to the typical fluctuations, leading to a step ladder appearance in the data. A resolution problem might also result from faulty instrument and data recording systems. A problem is detected by computing a series of discrete frequency distributions with 100 bins for 10 minute non-overlapping windows. The interval for the distribution is taken as the smaller of the mean plus and minus 4 standard deviations, and the range. The percent of bins with zero points is averaged over all 10 minute windows. When the record average percent of empty bins exceeds 60 percent, the record is hard flagged as having a resolution problem. The 60 percent threshold is based on numerical experiments which artificially decrease the resolution and compute the change in the flux. These show that the flux is insensitive to the resolution (less than 1 percent flux change) until the ratio of the resolution to the standard deviation approaches 0.15, which is the point where the percent of empty bins nears 60 percent.

4.2 Drop outs

Data dropouts may be indicative of a dead or pegged instrument or electronic recording problems. Dropouts are identified using the same frequency distributions used for the resolution problem. A record is hard flagged when 40 or more consecutive data points (4 seconds for 10Hz RASEX data) fall in the same bin.

4.3 Spikes

Data spikes can be caused by random electronic spikes in the monitoring or recording systems as might occur during precipitation when water can collect on the transducers of the sonic anemometer. The spike detection method computes the mean and standard deviation for a series of 5 minute running windows. Any point in the window which exceeds plus or minus 3.5 standard deviations from the mean is considered a spike. The replacement is done using linear interpolation. When 4 or more consecutive spikes are detected, they are considered a real event and not spikes, and are not replaced. The entire process is repeated for 5 passes or until no more spikes are found. During the second pass, when the standard deviations may be smaller if spikes were replaced on a previous pass, the threshold for spike detection increases to 3.6 standard deviations, and a like amount for each subsequent pass. The record is hard flagged as having too many spikes when the number of spikes exceeds 0.5 percent of the total number of points (180 spikes for a 1 hour record of 10Hz RASEX data). The threshold of 3.5 standard deviations is somewhat arbitrary. We base our selection on visual inspection of the especially spikey records before and after the despiking.

4.4 Absolute limits

Unrealistic data values may occur for a large number of reasons. These are detected and hard flagged by simply comparing the minimum and maximum value of all points in the record to some fixed limits. For the sonic anemometer, these limits are 30 m/s for horizontal wind components, 5 m/s for vertical wind and -10 to +30 degrees C for virtual temperature. The absolute air temperature and water temperature are hard flagged when the record mean value is outside the range (-10,30) degrees C.

The cup anemometer winds speeds are flagged when the record mean value is outside the range (1.5,30) m/s. The cups in RASEX were calibrated to provide the best accuracy at higher wind speeds, and are not reliable when the speed is less than 1.5 m/s. This is a soft flag in terms of calculating the wind stress and heat flux from the sonic, but is a hard flag for all cup profile calculations and intercomparisons of sonic and cup data.

4.5 Higher moment statistics

Higher moment statistics are used to detect possible instrument or recording problems and physical but unusual behavior. The skewness and kurtosis are computed for the entire record and compared to fixed limits. The record is hard flagged when the skewness is outside the range (-2,2) or the kurtosis is outside the range (1,8). These limits are somewhat arbitrary, and are selected here because they detect only the most extreme cases for RASEX. The record is soft flagged when the skewness is outside the range (-1,1) or the kurtosis is outside (2,5).

4.6 Discontinuities

Discontinuities in the data are detected using the Haar transform (Mahrt, 1991). The Haar computes the difference in some quantity over two half window means. Large values of the transform identify changes which are coherent on the time scale of the window. The goal is to detect discontinuities in the mean on the 5 minute time scale that are semi-permanent changes as opposed to sharp changes associated with smaller scale fluctuations. The transform is computed for a series of 5 minute running windows and then normalized by the standard deviation for the entire record. The record is hard flagged if the absolute value of any single normalized transform exceeds 3, and soft flagged at 2.

To identify coherent changes on the 5 minute time scale in the intensity of the fluctuations, we compute the variance about the mean for each half window and then compute the difference normalized by the variance over the entire record. The record is then hard flagged if the absolute value of any single normalized transform exceeds 3, and soft flagged at 2.

Persistent very small scale discontinuities are detected using a similar

technique. The absolute value of the Haar transform of the mean is computed for a series of 30 second running windows and then normalized by the standard deviation for the entire record. The record mean transform is then compared to fixed limits. The record is hard flagged if the value exceeds 1, and soft flagged at 0.5.

4.7 Unusual or inconsistent vertical structure

Here, and elsewhere, vertical temperature gradients are converted to potential temperature gradients by adding the adiabatic lapse rate of 0.98 C/100 m. A soft flag is raised if the vertical gradient of potential temperature computed from either of the two direct temperature difference measurements falls outside the range (-0.1,0.1) K/m. Temperature difference measurements are available for 47 - 10 m and for 24 - 10 m levels.

A soft flag is raised if the vertical gradient of wind speed computed from the cup wind speeds (48 - 7 m) and (20 - 7 m) falls outside the range (-0.02,0.20) s⁻¹.

The friction velocity computed from wind profiles at the lower part of the tower (7,15,20,29 m) is compared to that computed from the upper levels (29,38,43,48 m). When the difference normalized by the average exceeds 50 percent, the record is soft flagged. There are many cases where the stress increases significantly with height. Some of these cases are associated with internal boundary layer flow from land but flow distortion at the lowest levels could also be important.

Additional soft flags are raised if the stratification of potential temperature behaves in an abnormal way. The conditions are:

- i) Stability reverses with height

$$\left[\frac{d\theta}{dz}\right]_{high} * \left[\frac{d\theta}{dz}\right]_{low} < 0 \quad (5)$$

- ii) Stability increases with height

$$\left[\frac{d\theta}{dz}\right]_{high} > \left[\frac{d\theta}{dz}\right]_{low} > 0 \quad (6)$$

- iii) Instability increases with height

$$\left[\frac{d\theta}{dz}\right]_{high} < \left[\frac{d\theta}{dz}\right]_{low} < 0 \quad (7)$$

iv) The air-sea temperature difference is a different sign from the atmospheric stability

$$\left[\frac{d\theta}{dz}\right]_{47-10m} * \left[\frac{\theta_{10m} - \theta_{sc}}{10m}\right] < 0 \quad (8)$$

4.8 Intercomparison

The friction velocity calculated from the sonic anemometer eddy correlations and from the cup wind profile from the (7,15,20,29 m) levels is compared. When the difference normalized by the average exceeds 50 percent, the record is soft flagged. These differences require further study.

4.9 Nonstationarity of the horizontal wind

Nonstationary records are of great interest in analyzing the stress and the drag coefficient. These cases are usually identified with weak large scale flow and significant relative mesoscale variability. In this case, the drag coefficient for numerical models, which are necessarily based on the speed of the vector averaged wind, will be different from that computed with the average wind speed. Four measures of the nonstationarity are computed and soft flags are assigned.

The *wind speed reduction* is defined as the ratio of the speed of the vector averaged wind to the averaged speed. When this ratio falls below 0.9, there is some cancellation in the vector average of the wind components and a soft flag is raised.

The *along-wind relative nonstationarity* is calculated using a linear regression to estimate the difference in the along-wind component between the beginning and end of the record, δu . This difference normalized by the mean of the along-wind component, $[u]$, is used to compute the relative nonstationarity,

$$RNu = \delta u / [u] \quad (9)$$

Positive (negative) RNu corresponds to accelerating (decelerating) winds over the record.

The *cross-wind relative nonstationarity*, RNv , is computed from the difference based on the regression of the cross-wind component δv , such that,

$$RNv = \delta v / [u] \quad (10)$$

Any systematic wind direction change over the record is proportional to RNv .

The *vector wind nonstationarity* is given by

$$RNS = \frac{(\delta u^2 + \delta v^2)^{1/2}}{[u]} \quad (11)$$

The record is soft flagged if any of RNu , RNv or RNS exceed 0.25. These records will be used for further study of the drag coefficient under nonstationary conditions.

4.10 Precipitation

The sonic anemometers are thought to be more likely to produce spikes during precipitation, especially for virtual temperature. Precipitation at the RASEX land mast (located 2 km from sea mast west) was measured with a semi-conductor plate, which measures one value if the plate is dry and another if wet, and the 30 minute statistics recorded. A soft flag is raised for the record when the mean value indicates it was raining more than half the time.

5 Flux sampling errors

Three types of sampling errors will be considered in assessing the reliability of the flux measurements:

i) The *systematic error* is the error due to the failure to capture all of the largest transporting scales, typically leading to an underestimation of the flux.

ii) The *random error* is due to an inadequate sample of the main transporting eddies as a consequence of too short a record length.

iii) The *nonstationarity* is due to mesoscale variability which can lead to a significant dependence of both the flux and drag coefficient on the choice of averaging scale.

In the selection of the critical values of the flux sampling and nonstationarity parameters for flagging records, much larger errors will be tolerated compared to the criteria for instrumentation problems, and, only soft flags will be employed. This toleration of flux sampling errors recognizes the fact that the error estimates themselves are somewhat uncertain and complex. For example, strict criteria for the random flux error leads to removal of many of the weak wind cases, creating a bias in the data.

There are trade offs to be made in reducing the three types of error. The systematic error can be reduced by increasing the scale of eddies included in the flux. However, as the scale increases, the number of independent samples of the flux necessarily decreases, which can only increase the random error. Increasing the scale also increases the chance of including mesoscale variability.

5.1 Systematic error

The task is to determine which scales of motion must be included in the calculation of the flux. Turbulent fluctuations of some quantity, ϕ , are defined as deviations from the *local average*, $\bar{\phi}$, in which case the decomposition of ϕ can be written as

$$\phi = \bar{\phi} + \phi' \quad (12)$$

where $\bar{\phi}$ is an average over time scale L . The averaging time L defines the longest time scales of the motions included in the turbulent flux. L might be chosen to include only scales which have characteristics of turbulence. Or, in order to estimate the total flux, L should include all scales of transport, regardless of their physical characteristics. To determine L , we select all of the records which are stationary based on the time-dependence of the horizontal wind. Nonstationary records are discarded for this analysis since in this case the choice of L is not well defined and the flux can continue

to increase or decrease on scales larger than those normally associated with turbulence. For these purposes we define stationary records as those where $|RNu| < .1$, $|RNv| < 0.1$ and $RNS < 0.1$. For the stationary records we compute the flux $w'\phi'$ for different values of L , average the flux over the record, and then for each L average over all records. In order to provide greater resolution at the smaller scales where sensitivity is greatest, we choose a dyadic set of scales with R equal to the record length,

$$L = \frac{R}{2^n}; n = 0, 1, \dots 4 \quad (13)$$

The results for the 110 most stationary records for the 10 m sonic vector stress are shown in Figure 1. In the figure, the flux is normalized so that the $L = R$ stress is one. These results indicate that choosing L equal to 3.75 minutes captures 95 percent of the record stress, and choosing L equal to 7.5 minutes captures 98 percent. For final flux and drag coefficient calculations, we select L equal to 10 minutes. Choosing L larger would not significantly increase the flux, at least for the stationary records, and would reduce the number of flux samples in each record, which would increase the random sampling error. A more finely tuned approach might allow L to vary, since the scale of the transporting eddies is larger with unstable conditions and deeper boundary-layer flow and the time duration of the eddies viewed from the tower decreases with increasing wind speed.

Although L is chosen to include almost all of the turbulent flux for stationary conditions, the choice of L is not obvious for nonstationary conditions. To document such cases, we define a crude measure of the systematic error

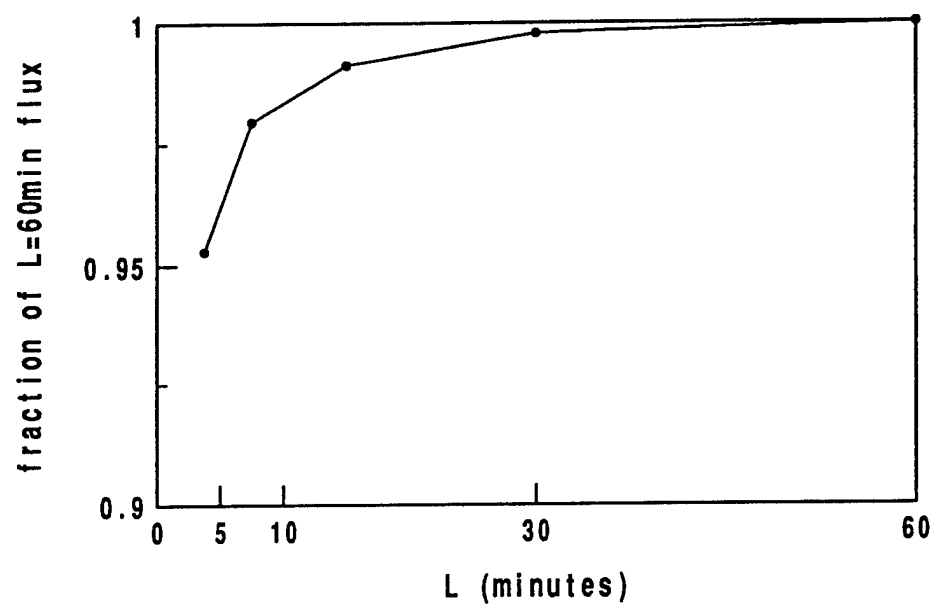
$$RSE = \frac{\langle w'\phi' \rangle_{2L} - \langle w'\phi' \rangle_L}{\langle w'\phi' \rangle_L} \quad (14)$$

where the averaging operator $\langle \rangle$ indicates an average over the entire record, and $L = 10$ minutes.

The vector stress version of RSE is given by

$$RSE = \frac{((\langle w'u' \rangle_{2L} - \langle w'u' \rangle_L)^2 + (\langle w'v' \rangle_{2L} - \langle w'v' \rangle_L)^2)^{1/2}}{(\langle w'u' \rangle_L^2 + \langle w'v' \rangle_L^2)^{1/2}} \quad (15)$$

Figure 1.



Records are soft flagged when RSE for the heat flux, the along-wind component of the stress or the vector stress exceeds 0.25. The cross-wind component of the stress is not flagged, as the expected value of $\langle w'v' \rangle$ is zero.

5.2 Random error

In order to provide a stable estimate of the flux with small random sampling error, it is necessary to average the flux over a period which is longer than L . Here, the instantaneous flux will be averaged over the record length R such that the flux is expressed as

$$\langle w'\phi' \rangle \quad (16)$$

The ideal choice of record length is long enough to reduce the random error but short enough to avoid capture of nonstationarity associated with meso and synoptic scale variability. Unfortunately, atmospheric flows are characterized by motions which simultaneously vary on a variety of scales. The spectra of the along wind component rarely shows a well defined spectral gap. As a result, some motion usually appears on scales which are just larger than the largest transport scales.

The following partitions the variability of the turbulent flux into random variability associated with random location and strength of the transporting eddies, and, systematic variation associated with modulation by larger scale motions. This partitioning is implemented by dividing the record into nonoverlapping subrecords of width $L=5$ minutes and computing the average flux for each subrecord, symbolized as F_i . The subrecord flux, F_i , is partitioned into the record mean value $\langle F \rangle \equiv \langle w'\phi' \rangle$, the linear trend (less the record mean), F_{tr} and the deviation from the linear trend F_i^* , such that

$$F_i = \langle F \rangle + F_{tr} + F_i^* \quad (17)$$

$$F_{tr} = a_0 + a_1 t \quad (18)$$

where a_0 and a_1 are the coefficients for the least squares fit. When the 90 percent confidence interval for the slope a_1 includes zero, the slope is set

to zero. To assess the error in the estimate of the flux due to random flux errors, we compute the relative flux error defined as the ratio of the standard flux error to the mean flux

$$RFE \equiv \frac{\sigma_{F^*}}{|\langle F \rangle| N^{1/2}} \quad (19)$$

where σ_{F^*} is the standard deviation of the random part of the flux, and N is the number of subrecords of width L , equal to R/L . For this calculation, L is chosen as 5 min. and R as 60 min., corresponding to $N=12$. Choosing a smaller L would omit too much flux for some records, while increasing R would increase the probability of capturing significant nonstationarity. Corrections due to dependence between subrecords (Sun and Mahrt, 1994) are not included.

The corresponding measure of nonstationarity is defined as

$$RN \equiv \frac{\sigma_{Ftr}}{|\langle F \rangle| N^{1/2}} \quad (20)$$

where σ_{Ftr} is the standard deviation due to the trend, which can be computed analytically from the slope of the trend, a_1 . Since the random part of the flux, F_i^* , is not significantly correlated with time, and therefore not correlated with the trend, F_{tr} , the total variance of F_i is approximately the sum of the random variance and the variance due to the trend. The two variances tend to be correlated. That is, records with large flux trend also have large random variation of the flux. Outlying values of F_i and nonlinear trend could both increase the two variances simultaneously; however, the flux is in general more erratic in periods of change.

The expressions for the vector stress are

$$|\langle F \rangle| = [\langle w'u \rangle^2 + \langle w'v \rangle^2]^{1/2} \quad (21)$$

$$\sigma_{F^*} = [\sigma_{Fu^*}^2 + \sigma_{Fv^*}^2]^{1/2} \quad (22)$$

$$\sigma_{Ftr} = [\sigma_{Ftru}^2 + \sigma_{Ftrv}^2]^{1/2} \quad (23)$$

where Fu^* , Fv^* , $Ftru$ and $Ftrv$ refer to the random and linear trend parts of the along-wind and cross-wind momentum flux. If the relative nonstationarity of the flux is large, then RFE can no longer be formally interpreted as

the random error which is strictly defined for stationary conditions. *RFE* is then interpreted more loosely as a measure of the flux variability.

Records are soft flagged when *RFE* or *RN* for the heat flux, the along-wind component of the stress or the vector stress exceeds 0.25. The cross-wind component of the stress is not flagged, as the expected value of $|\langle F \rangle|$ is zero.

5.3 Flux events

In addition to the flux sampling errors described above, a measure of isolated large flux events is calculated. The parameter is

$$Event = \frac{Max(F_i)}{|\langle F \rangle|} \quad (24)$$

where again, F_i is the subrecord flux and $\langle F \rangle$ the record mean. As for the random errors, the subrecord length L is chosen as 5 minutes and the record is 1 hour. This parameter is usually highly correlated with *RFE*, but can significantly differ when the variation of the flux is due mainly to a single subrecord flux. In this sense, *Event* is a crude measure of the higher moments whereas the random flux error is based on the variance. Records are soft flagged when *Event* for the heat flux, the along-wind component of the stress or the vector stress exceeds 2.

6 Hard flagged records 10m sonic

A list of the records hard flagged using the above criteria for the spring and fall 10 m sonic data is shown in Table 1. The "check" column shows the result from visual inspection of the record. A \checkmark indicates the record is verified as unphysical and should be removed from further analysis, an "ok" indicates the record is unusual but plausible and will be retained, and a "gw" indicates a possible gravity wave case. Out of 609 total records, 23 (4 percent) are hard flagged, and of these only 7 are verified and removed after visual inspection.

Table 1. 10 meter sonic hard flagged records

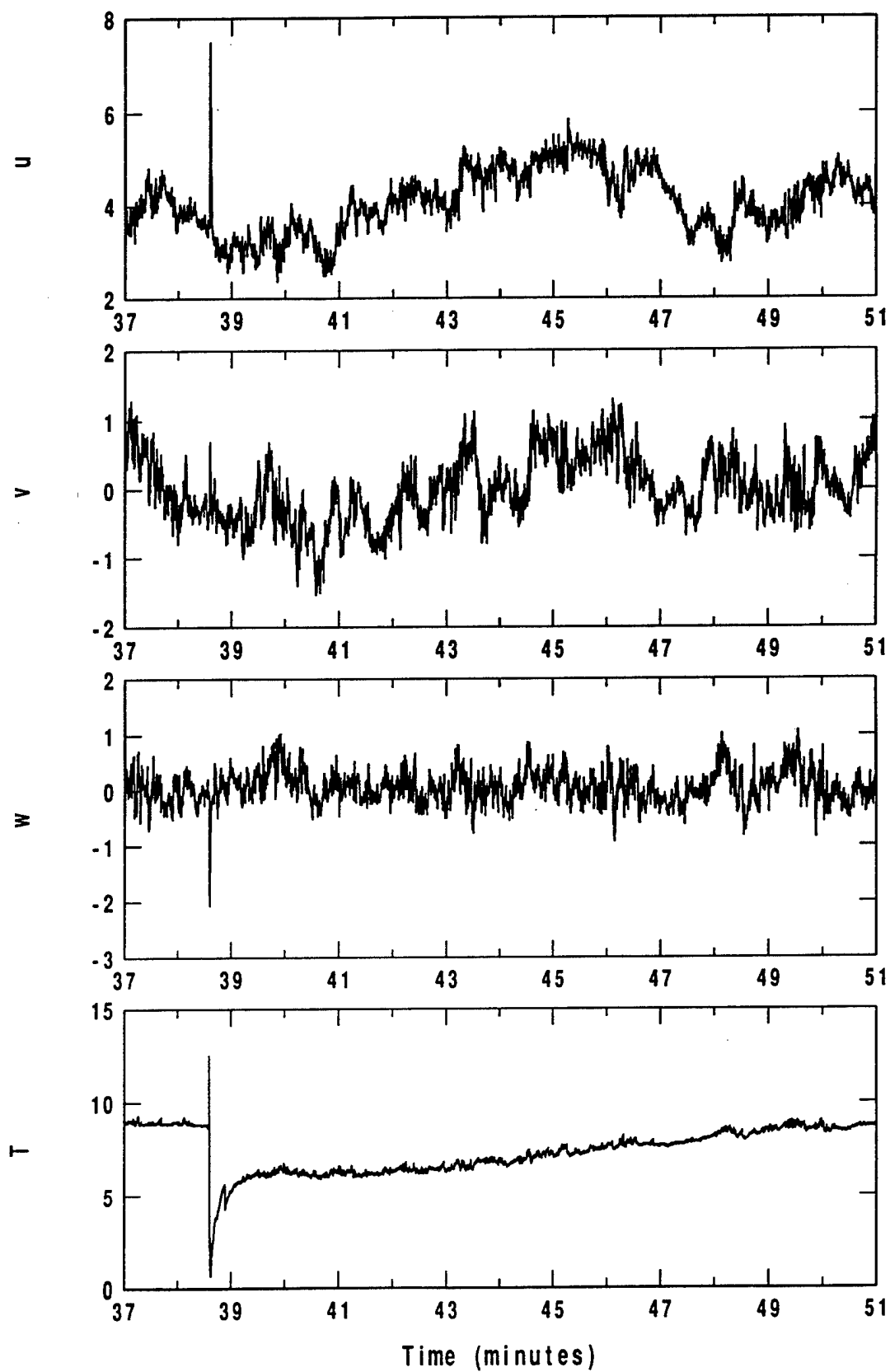
record	10m sonic hard flag(s)	speed	dir	check
122/020327	Haar var w, dropouts v	3.5	288	ok
277/041804	Haar var T	10.0	269	ok
277/041904	Haar mean u	9.3	283	ok
278/050826	dropouts u,v,w,T	9.1	306	✓
281/080514	Haar mean and var T	3.7	183	gw
284/111922	skewness and kurtosis T	5.2	237	ok
287/142210	kurtosis T	3.6	173	ok
288/150010	Haar var and dropouts T	4.5	197	✓
288/150610	Haar mean T	5.7	245	✓
290/170956	skew, kurt, Haar var, dropouts T	0.9	289	✓
290/171956	dropouts v	2.4	291	ok
291/180715	Haar var T	1.6	212	ok
297/241927	kurtosis and Haar var w	5.0	176	ok
299/260114	skewness T	5.2	144	✓
303/300431	kurtosis v	6.1	182	ok
303/301834	resolution and skewness T	1.6	255	✓
303/302234	dropouts T	4.3	159	✓
304/310534	Haar mean v	1.1	172	gw
310/061720	Haar var w	2.0	188	ok
310/061920	resolution T, Haar var w	0.9	183	ok
310/062120	Haar var w	1.9	235	ok
310/062320	Haar var w	1.8	294	ok
311/070646	resolution T	0.8	190	ok

6.1 Verified Problems

Record 278/050826 is flagged for a data dropout of 5 minutes which effects all fields from the sonic. All quantities are fixed at a constant value during this period.

Figure 2 shows record 288/150010 flagged for a large Haar jump in the variance and for dropouts of virtual temperature. All the wind components and the virtual temperature are effected by an instrumental spike near minute 39 into the record. The spikes are of sufficient duration that it is not con-

Figure 2. Record 288/150010



sidered an electronic spike by the despiking method. After the event, the virtual temperature requires nearly 10 minutes to recover to the pre-spike levels. Precipitation was recorded during this period and is a likely cause of the spike event. The slow recovery of the virtual temperature suggests the transducers were effected by water which was gradually removed over the next 10 minutes.

Figure 3 shows record 288/150610 flagged for a large jump in the mean virtual temperature. There is no supporting physical evidence for a sharp jump of this magnitude. Precipitation was soft flagged for this record and may be the cause.

Another unrealistic virtual temperature event in very light winds is shown in Figure 4 for Record 290/170956. The skewness, kurtosis, Haar variance jump and dropouts are all flagged for virtual temperature. Near minute 28 into the record, the virtual temperature jumps upward nearly 2 degrees for 20 seconds then returns to the original value. This is the only virtual temperature event of this type during this record on the tower. An independent 10 m air temperature for this period recorded a temperature range of only 0.4 degrees during the first 30 minutes of this record. An isolated virtual temperature jump of this magnitude is not thought to be physical and is attributed to instrumental error.

Figure 5 shows record 299/260114 flagged for skewness of the virtual temperature caused by a sharp 0.6 degree increase at minute 53. The wind speed and direction data and absolute 10 m air temperature offer no support for such an increase. There is precipitation during the last half of the record which is probably responsible for the sharp increase.

The vertical velocity and virtual temperature for a representative 20 second segment in record 303/301834 are shown in Figure 6. The virtual temperature is flagged for a resolution problem and large skewness. The step ladder appearance of the series shows the virtual temperature resolution is near 0.02 degrees. For this record the heat flux cannot be reliably calculated.

A virtual temperature flagged for dropouts in record 303/302234 is shown in Figure 7. The virtual temperature flag is caused by a sharp discontinuity of 0.4 degrees lasting for 1 minute, a time scale too short to be flagged by the

Figure 3. Record 288/150610

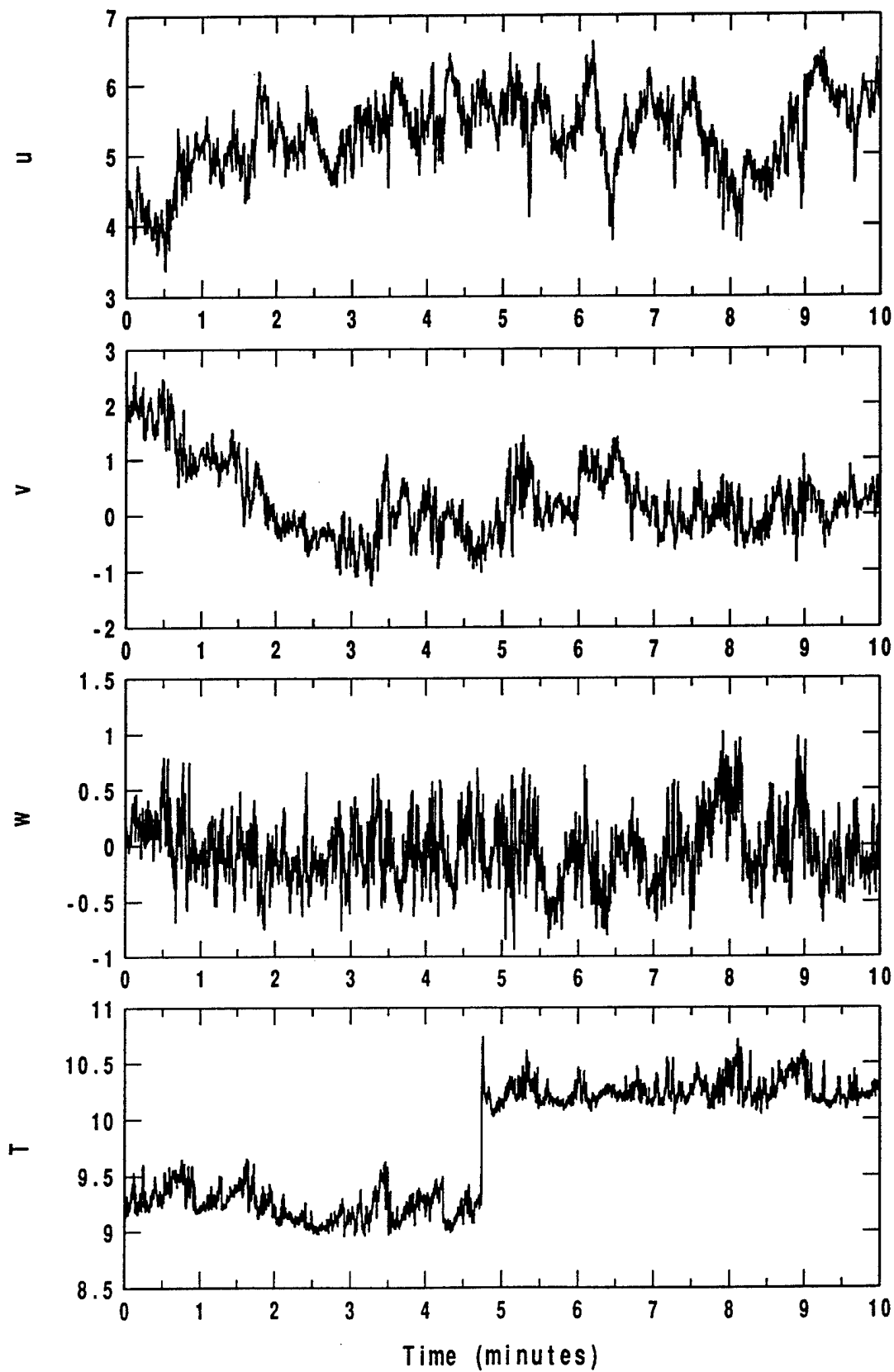


Figure 4. Record 290/170956.

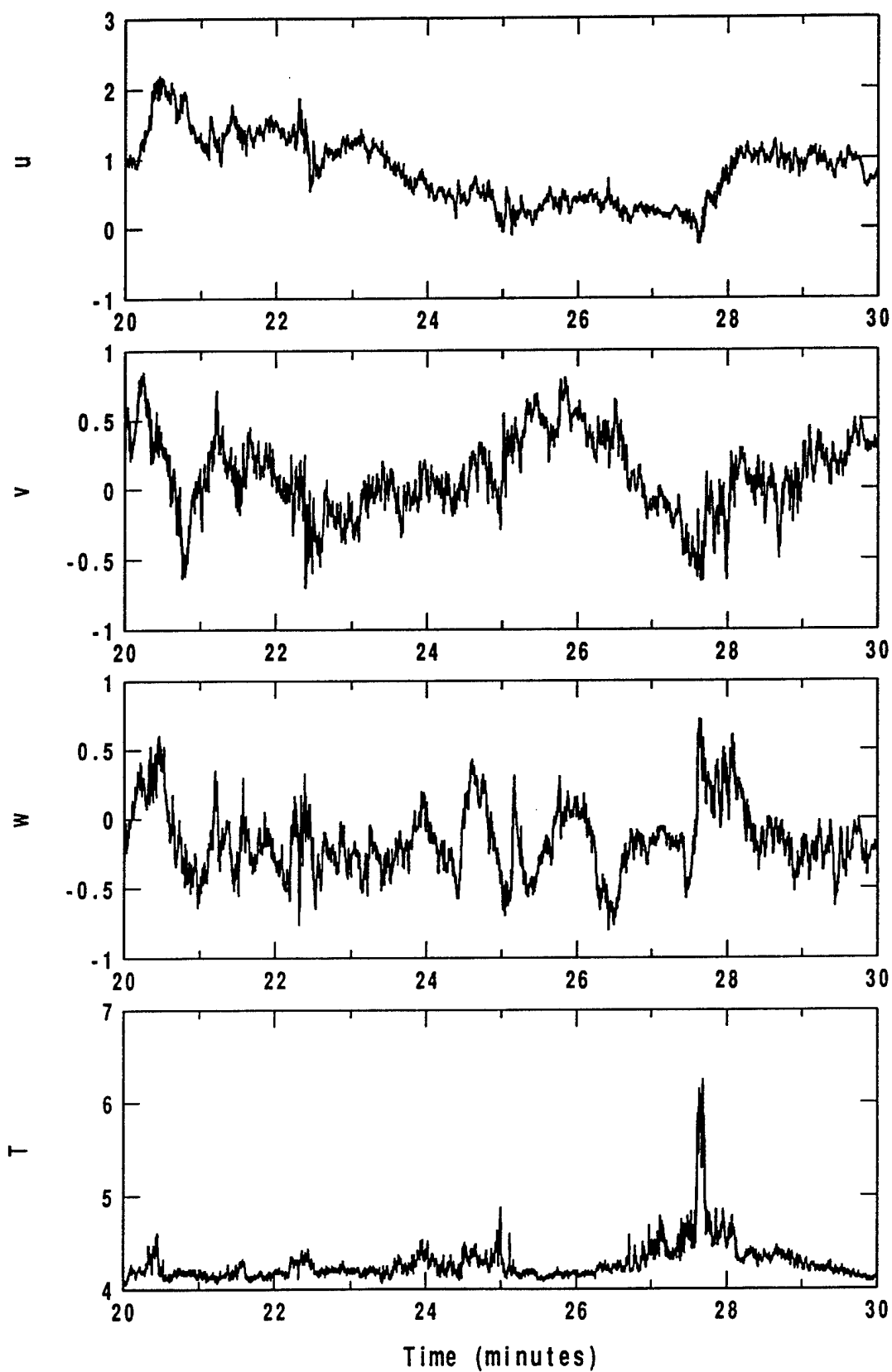


Figure 5. Record 299/260114.

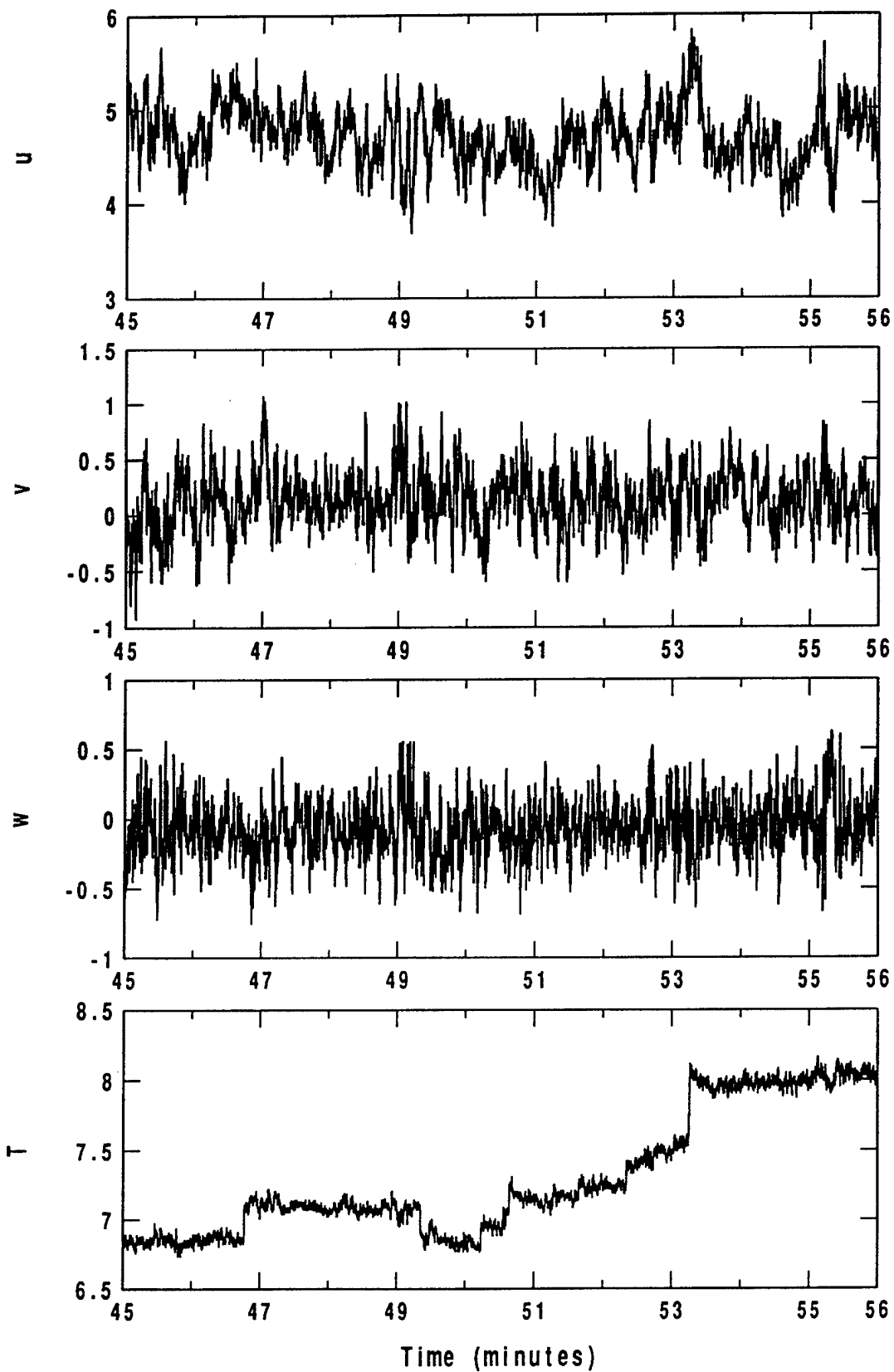


Figure 6. Record 303/301834

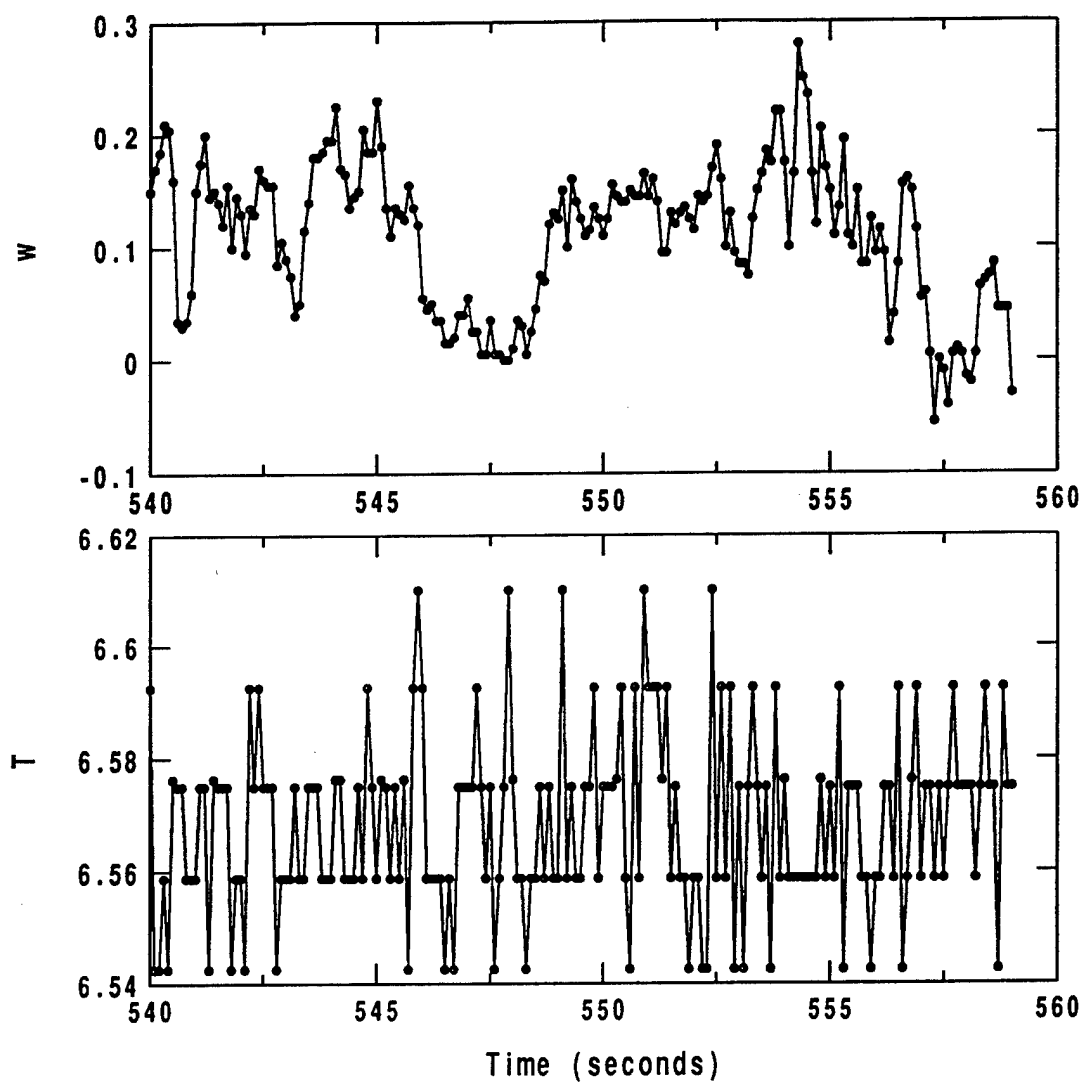
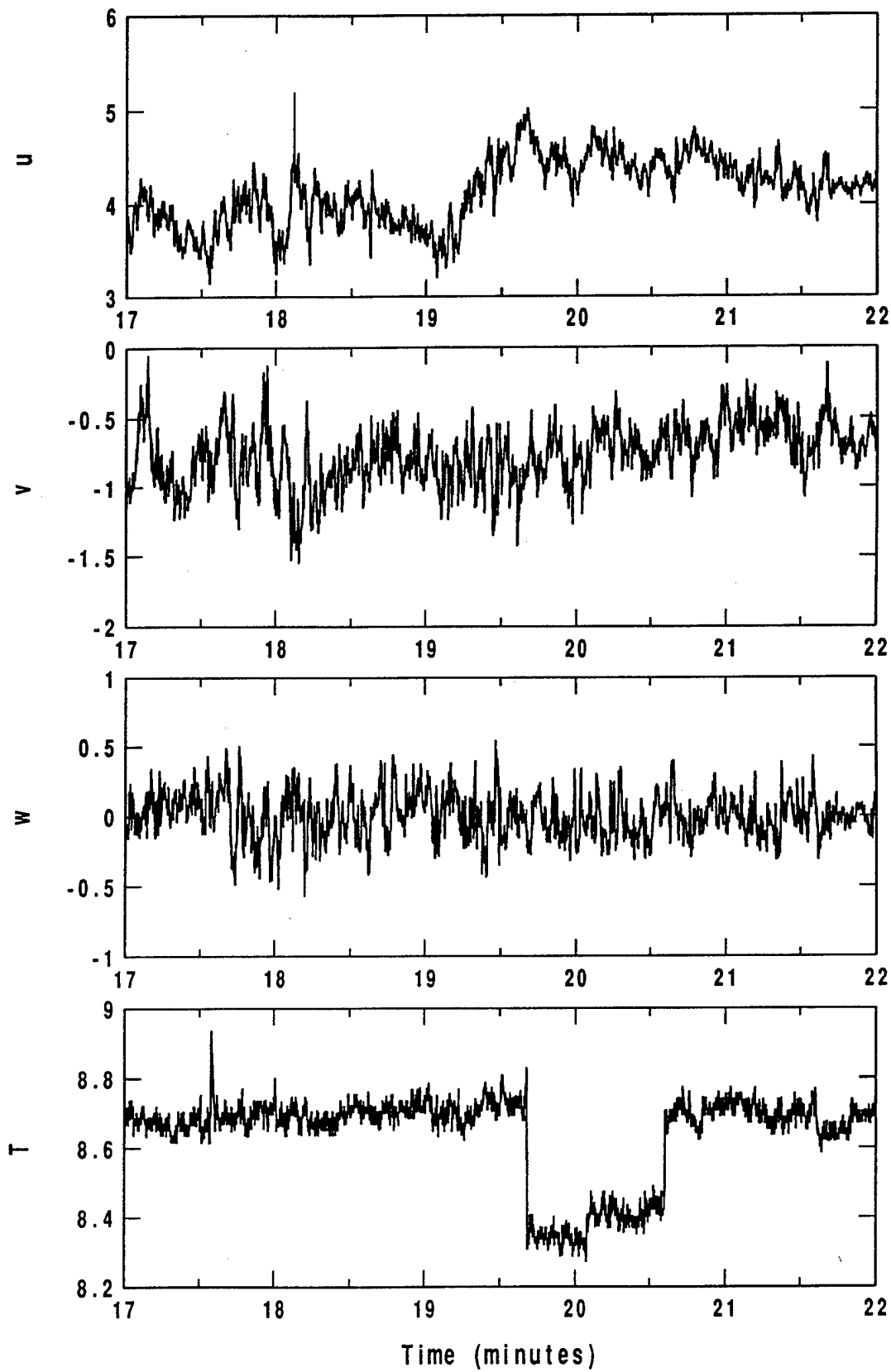


Figure 7. Record 303/302234



5 minute Haar tranform. The negative jump in the virtual temperature and subsequent positive jump back to the original levels after 1 minute, expands the range and thus the width of the bins used in the calculation of the discrete frequency distribution. Because the virtual temperature (and vertical velocity) fluctuations are generally small for this record, the sharp discontinuity triggers the flag. Constant precipitation was recorded during this off shore flow record, and is a probable cause of the virtual temperature discontinuity.

6.2 Unusual physical behavior

Four records on day 310, flagged for a large Haar jump in the variance of vertical velocity, are classified as plausible after visual inspection. These records exhibit light and variable southerly winds with bursts of intermittent turbulence. There was no precipitation recorded. Figure 8 shows the variance computed for the 310/061720 record using a 1 minute non-overlapping window for the statistics. All wind components and the virtual temperature show large fluctuations in the variance on short time scales. The vertical and horizontal wind component variances are positively correlated, $R=0.58$. This record has numerous soft flags; kurtosis of u and w , nonstationarity of the horizontal wind ($RNS=0.71$), a flux event for the along wind component ($Event=3.0$), all vector stress flux sampling flags, and RFE and RSE for the heat flux. Since changes in the local variances show positive correlation, they are probably physical.

Record 297/241927 is flagged for kurtosis and a Haar jump in the variance of the vertical velocity and demonstrates a sharp transition from near laminar flow to strong turbulence. Figure 9 show the wind component and virtual temperature variances using a 1 minute non-overlapping window. This record begins with moderate southerly winds and a short fetch. At 45 minutes into the record, the vertical velocity variance increases dramatically, the wind speed increases from 5 to 7 m/s, the wind direction shifts to a longer fetch and the virtual temperature rises more than 2 degrees. This behavior is supported by the cup anemometer at 20m, which measured an eight fold increase in the variance of the wind speed.

Record 281/080514 is an example of a gravity wave possibly initiated by

Figure 8. Record 310/061720

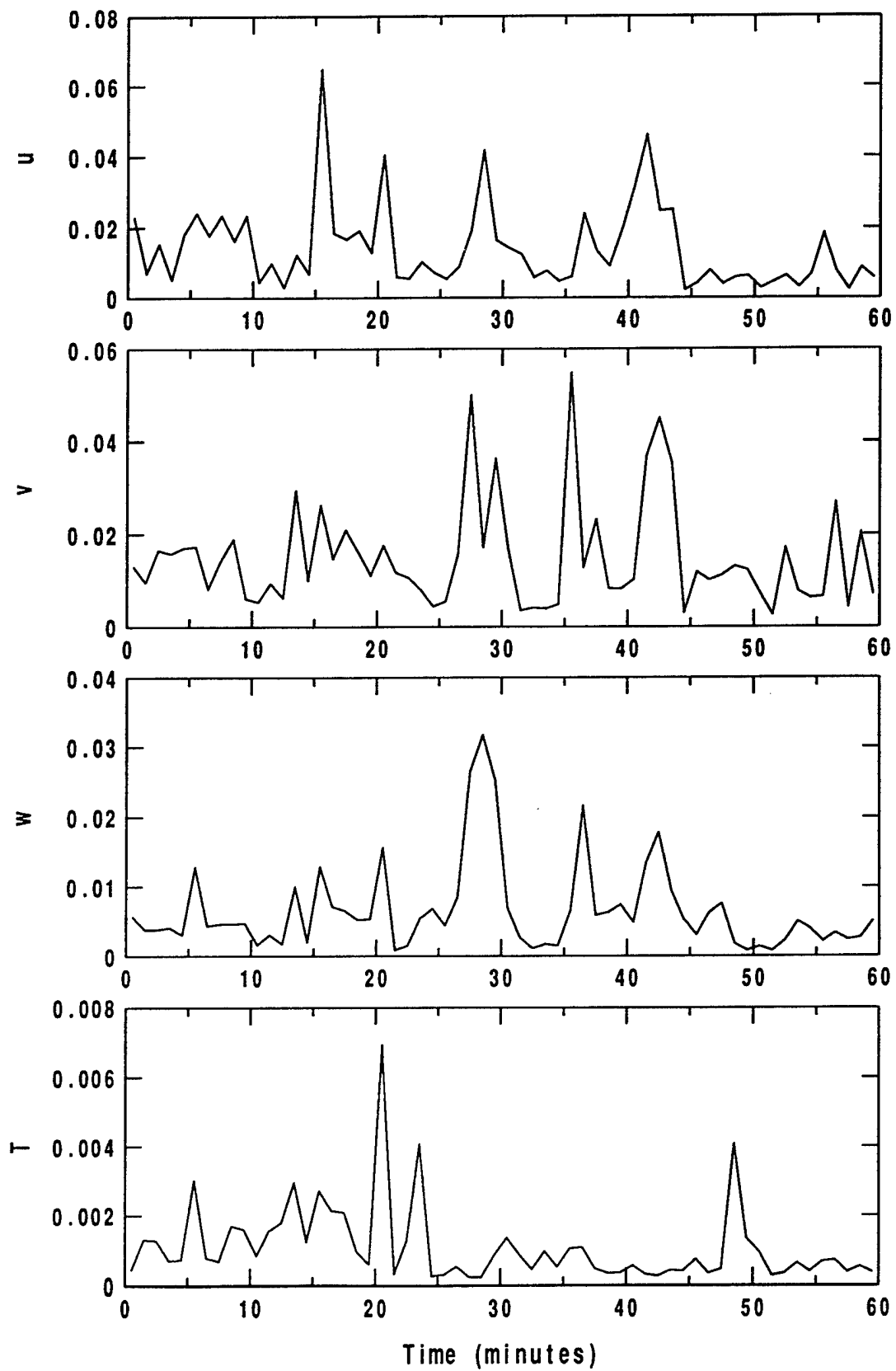
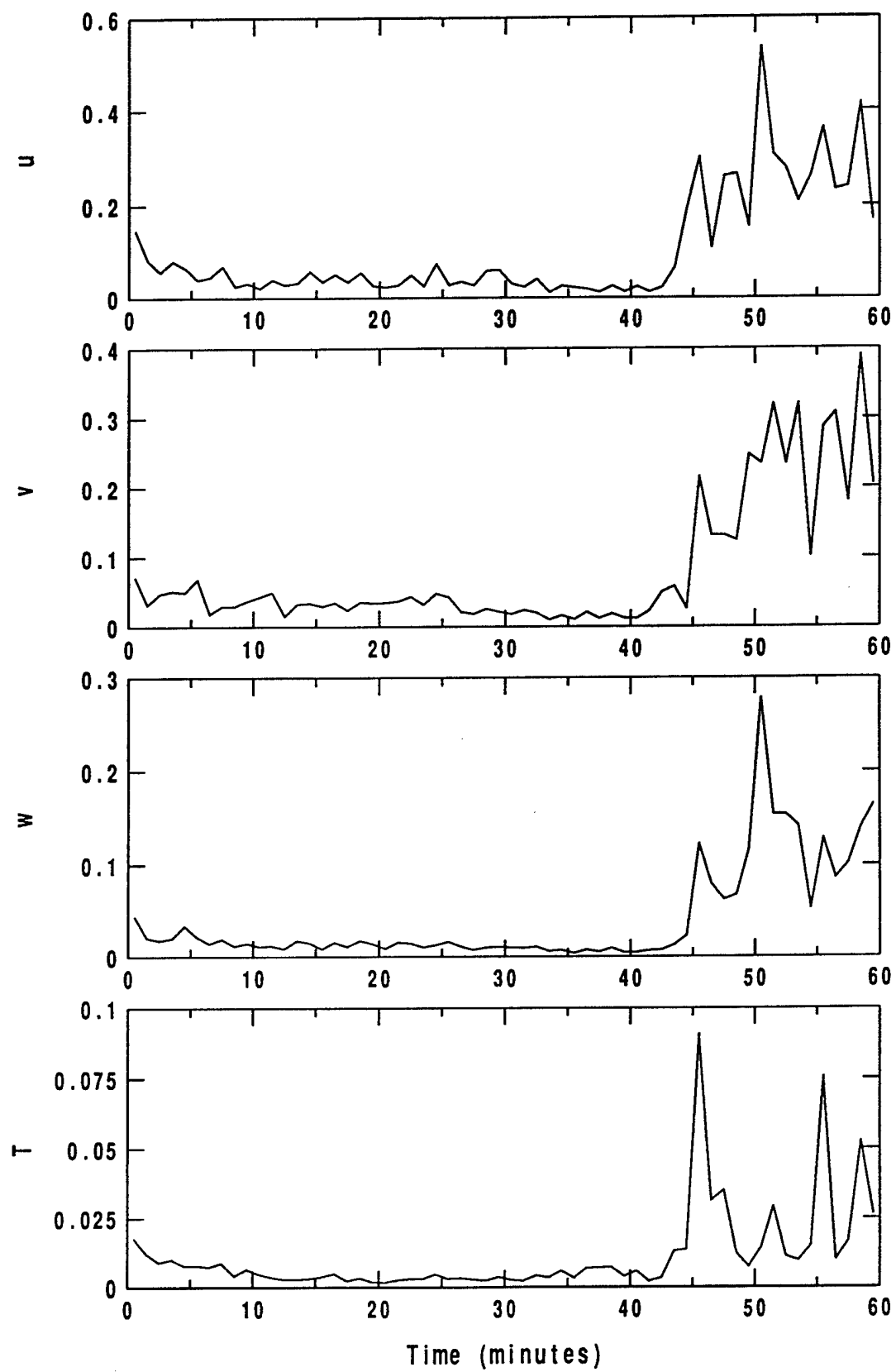


Figure 9. Record 297/241927



a frontal passage (Figure 10). Large Haar jumps in the mean and variance of virtual temperature for the 5 minute window are flagged. The winds are light southerly but increase with time, and the stability increases with height. The cross-wind component and the virtual temperature (Figure 10) are highly correlated ($R=-0.70$), consistent with a gravity wave train. There is significant trend in the heat flux ($RN = 0.44$), large relative random error ($RFE = 0.46$), and a very large flux event ($Event = 6$). The cross-wind component and the virtual temperature exhibit similiar behavior at the 32m level.

7 Hard flagged records 32m sonic

A list of the records hard flagged for the spring and fall 32 m sonic data is shown in Table 2. Out of 609 total records, 46 (8 percent) are hard flagged, and of these 18 are verified with visual inspection and removed.

Figure 10. Record 281/080514

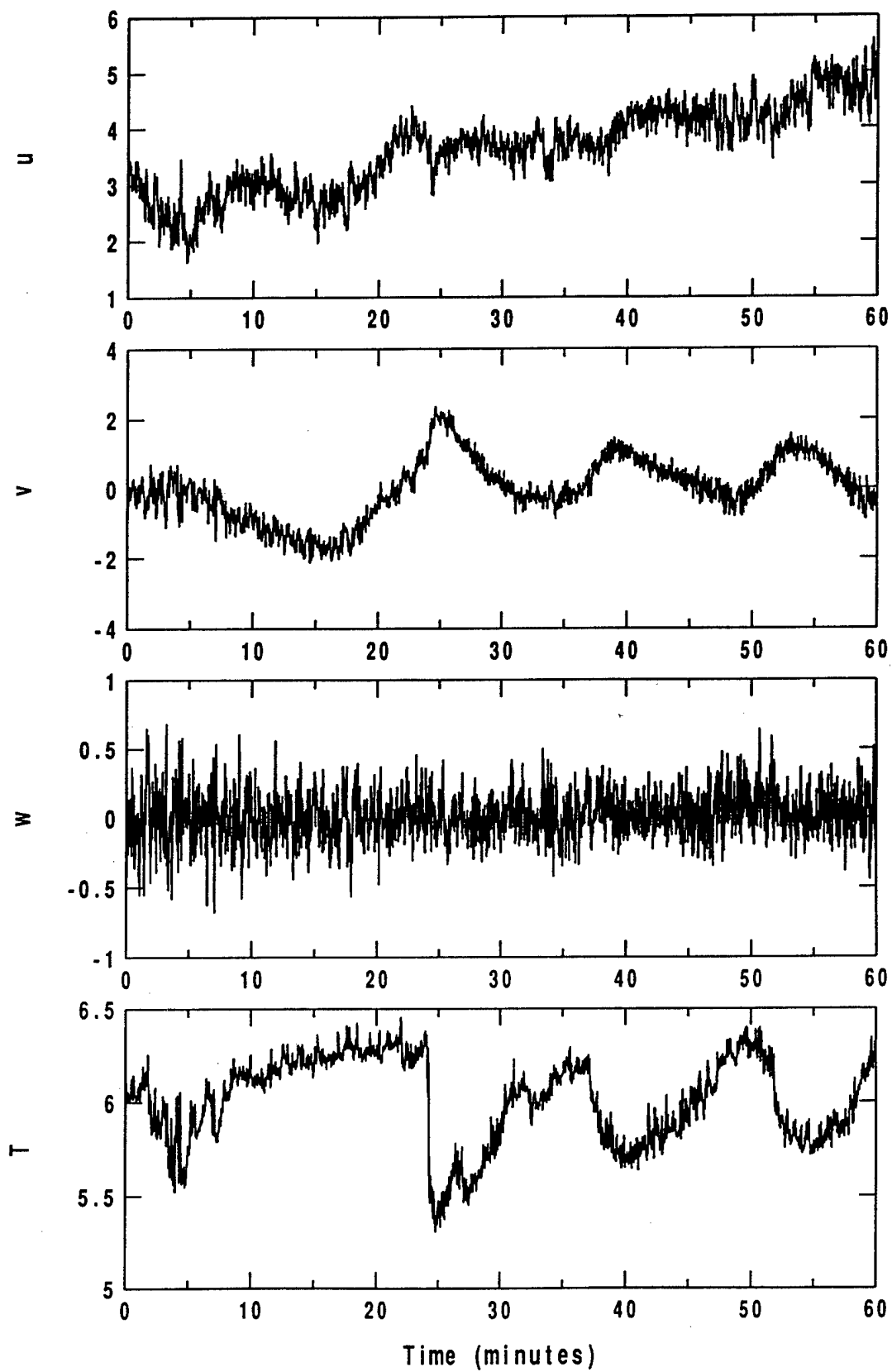


Table 2. 32 meter sonic hard flagged records

record	32m sonic hard flag(s)	speed	dir	check
118/282012	dropouts T	7.6	237	ok
119/291027	Haar var w	7.1	229	ok
122/020327	kurt and Haar var w	3.5	288	ok
122/021045	skew, kurt and Haar mean u	5.8	255	ok
125/050526	skew T, Haar var w	4.1	308	ok
276/030804	spikes T	14.2	331	✓
277/040919	skew and kurt T	9.5	270	✓
277/041904	Haar mean u	9.9	282	✓
278/050826	dropouts u,v,w and T	9.6	306	✓
279/060326	Haar var w and T	3.4	235	ok
279/060426	Haar mean and Haar var T	4.3	237	ok
279/060526	kurt and Haar var T	4.5	245	ok
279/060626	Haar var w	4.8	221	ok
281/081556	Haar var w	4.7	181	ok
282/091957	skew v and Haar var w	3.7	315	ok
283/101955	Haar var w	3.6	309	ok
284/111422	dropouts v	7.5	248	ok
287/141210	kurt T	5.3	231	ok
287/141810	skew, kurt and Haar var T	4.7	187	ok
287/142210	skew, kurt and Haar var T	4.6	173	✓
287/142310	skew, kurt and Haar var T	4.4	180	✓
290/170826	Haar var T	0.7	132	ok
291/180556	kurt and Haar var T, Haar var w	1.4	224	ok
291/180715	Haar mean and var w	1.3	212	ok
291/180815	resolution T, kurt and Haar var w	1.3	198	ok
291/181430	Haar var w	2.3	216	ok
291/181730	dropouts u	3.9	144	ok
291/181930	spikes w	6.1	122	ok
292/190935	out-of-range w	12.0	122	✓
297/241927	kurt and Haar var w and T, skew T	5.9	176	✓
297/242027	spikes, skew and kurt T	6.5	172	✓
299/260214	kurt and Haar var w and T, skew T	6.2	156	✓
299/261142	skew, kurt and Haar var T	12.6	230	✓

Table 2. continued, 32 meter sonic hard flagged records

record	32m sonic hard flag(s)	speed	dir	check
300/272306	spikes, skew and kurt T	9.2	235	✓
301/280006	skew and kurt T, out-of-range w	9.4	238	✓
302/292331	spikes, skew, kurt and Haar var T	7.8	151	✓
303/301014	Haar var w	5.4	248	ok
303/301834	Haar mean and var w	1.7	255	✓
303/301934	resolution T	0.8	172	✓
304/310534	Haar mean v	1.6	172	gw
305/011701	out-of-range w	17.1	248	✓
306/021041	Haar mean u	5.7	278	ok
306/022335	resolution T	0.6	151	gw
307/030035	resolution T and Haar var w	1.7	125	✓
310/061920	resolution T	0.9	183	ok
310/062120	Haar var w	2.0	235	ok

7.1 Verified Problems

Record 276/030804 is flagged for spikes in the virtual temperature. The range of virtual temperature during the last 30 minutes is near 20 degrees, while the standard deviation is only 1 degree. Almost continual precipitation was recorded during this record and is the probable cause of the spiking.

The virtual temperature record for 277/040919 is flagged for large skewness and kurtosis. During this period the winds are strong (9.5 m/s) and from the west with long fetch. The vertical velocity and virtual temperature for the last half of the record are shown in Figure 11. The virtual temperature fluctuations of 4.5 degrees near minute 45 are too large to be physical. There is some precipitation during this period.

Figure 12 shows record 277/041904 flagged for a jump in the Haar mean of the along-wind component. While the flag was detected from the wind component, the virtual temperature is the suspect field. The kurtosis of virtual temperature is 7.8, just below the hard flag threshold. Near minute 10, the virtual temperature jumps up nearly 6 degrees. The precipitation data indicate there were wet conditions during the first 30 minutes of the

Figure 11. Record 277/040919

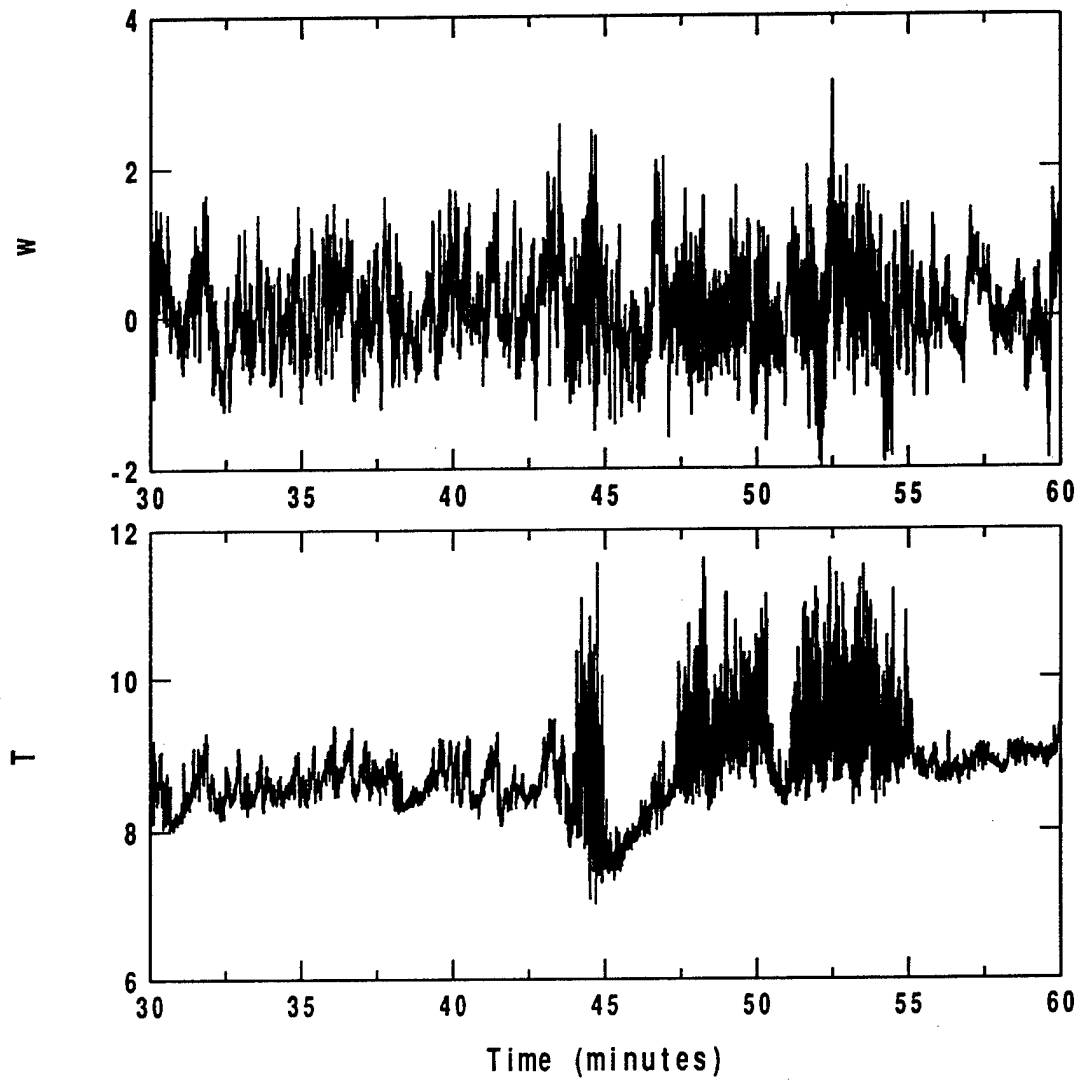
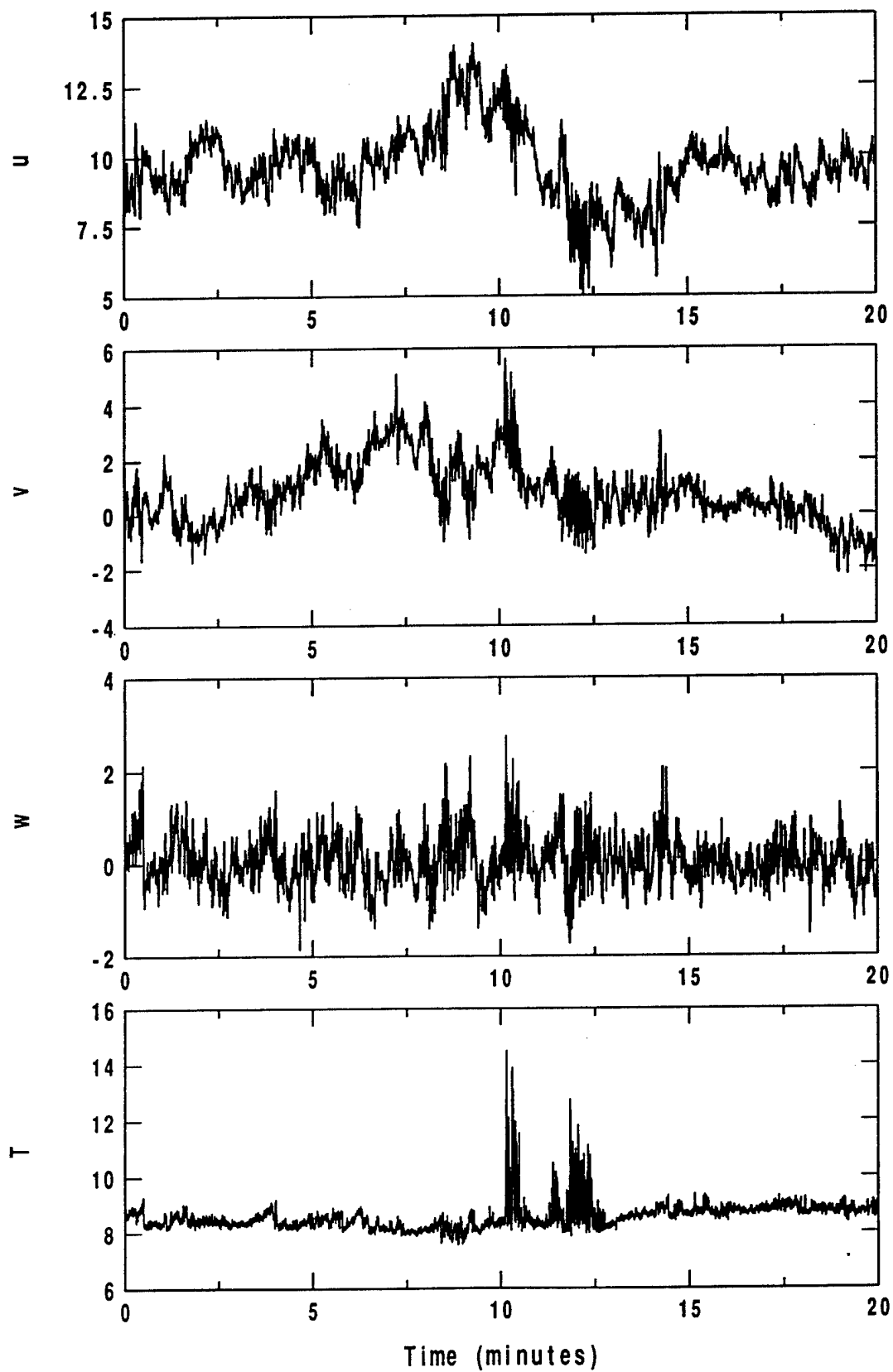


Figure 12. Record 277/041904.



record and totally dry conditions there after, which indicates precipitation is a possible cause of the unphysical virtual temperature behavior.

Record 278/050826 is flagged for a data dropout of 5 minutes which effects all fields from the sonic. The 10m sonic was also dropping out during this period.

The virtual temperature for record 287/142210 changes by an unrealistic amount in a short time (Figure 13). Some precipitation occurred during this period with moderate southerly winds. Record 287/142310 is shown in Figure 14. This record immediately follows the previous one where the virtual temperature dropped, and shows the recovery after the first minute. Once again, precipitation is a possible cause.

Records 292/190935 and 305/011701 are flagged for the vertical velocity exceeding the absolute limit threshold in very high winds. A vertical velocity exceeding 5 m/s is thought to be unphysical.

The vertical velocity and virtual temperature are hard flagged for kurtosis (31 and 12 respectively) and a large Haar jump in the variance (4.3 and 4.7) for record 297/241927. This record is moderate, increasing to strong, southerly winds. The vertical velocity and virtual temperature for the last 30 minutes are shown in Figure 15. For this same record, the 10m sonic was flagged for kurtosis and Haar variance of the vertical velocity, and classified as a physical sharp transition from weak to strong turbulence at minute 45. The 32m sonic wind components support this transition, but the behavior of the virtual temperature at 32m is not thought to be physically possible. The virtual temperature variance increase lags the wind transition by 10 minutes, and then becomes extremely large, probably caused by precipitation. During the first half of the record, no precipitation and no unusual behavior was recorded, while the second half is wet and has large, positively skewed fluctuations.

The next 5 verified hard flagged records in Table 2 have similar behavior to the previous record, 297/241927. In all cases, the virtual temperature, and to a lesser extent the wind components, display large fluctuations which are not thought to be physical and are highly correlated with changes in precipitation. The wind components by themselves might be considered plausible, but the magnitude of the corresponding virtual temperature changes

Figure 13. Record 287/142210.

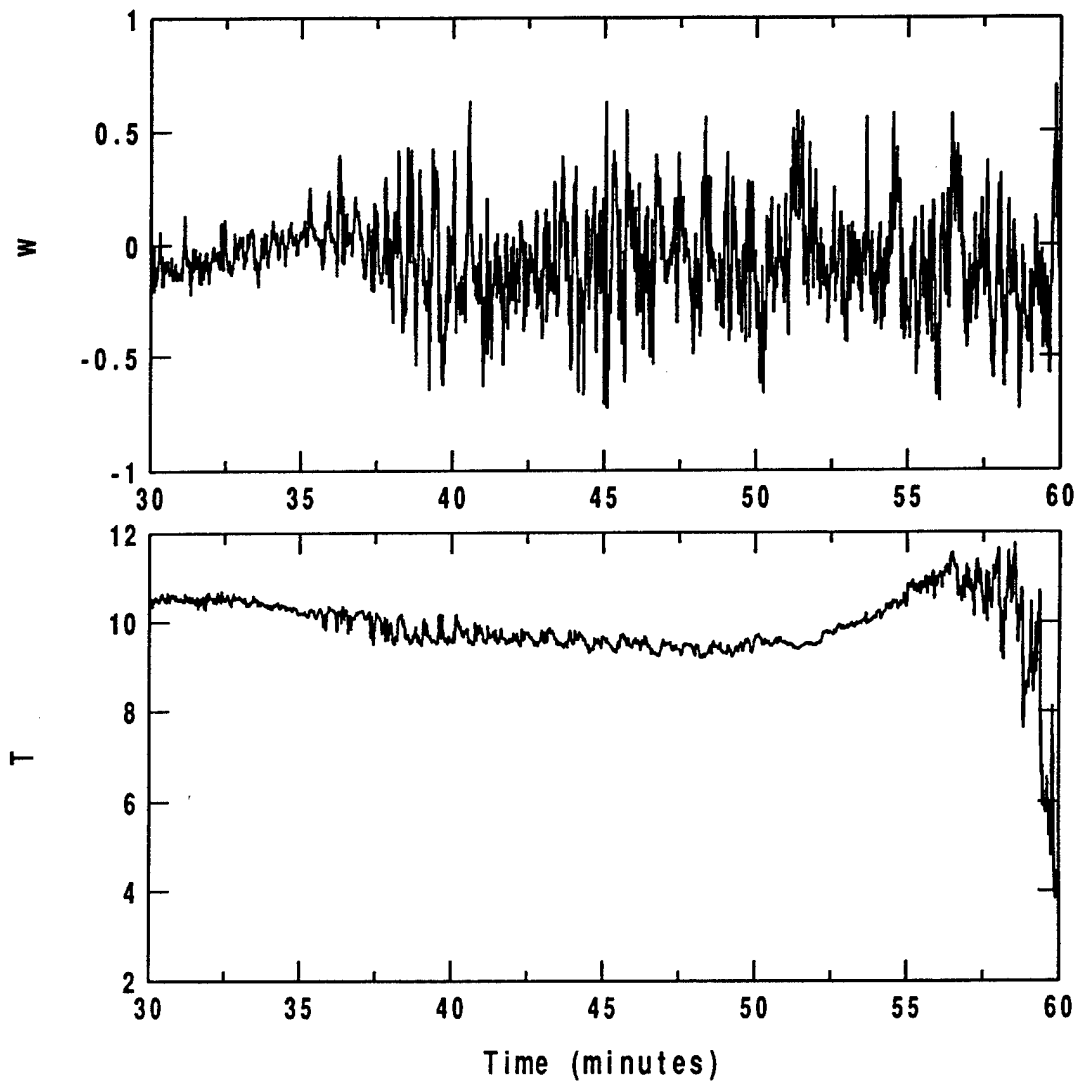


Figure 14. Record 287/142310.

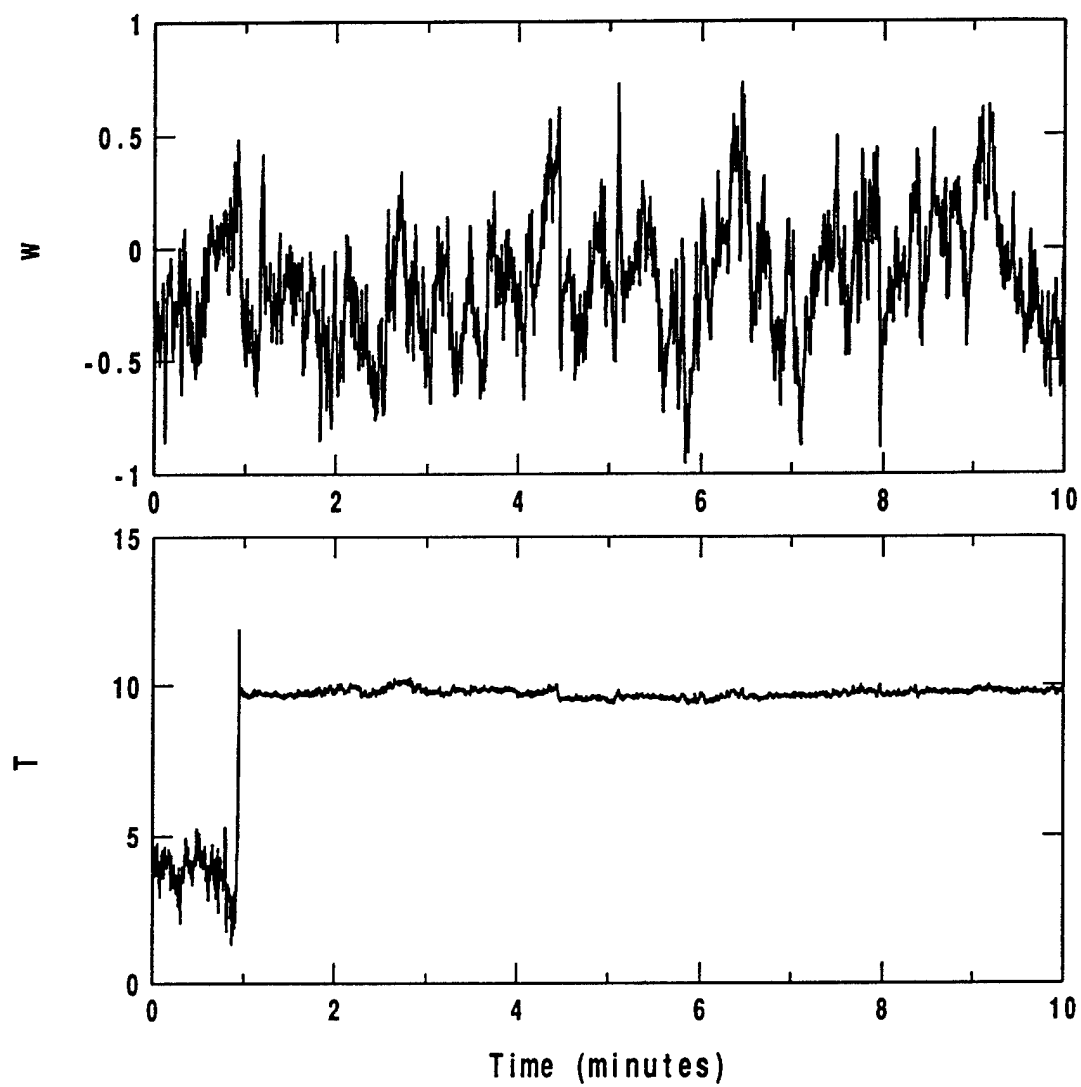
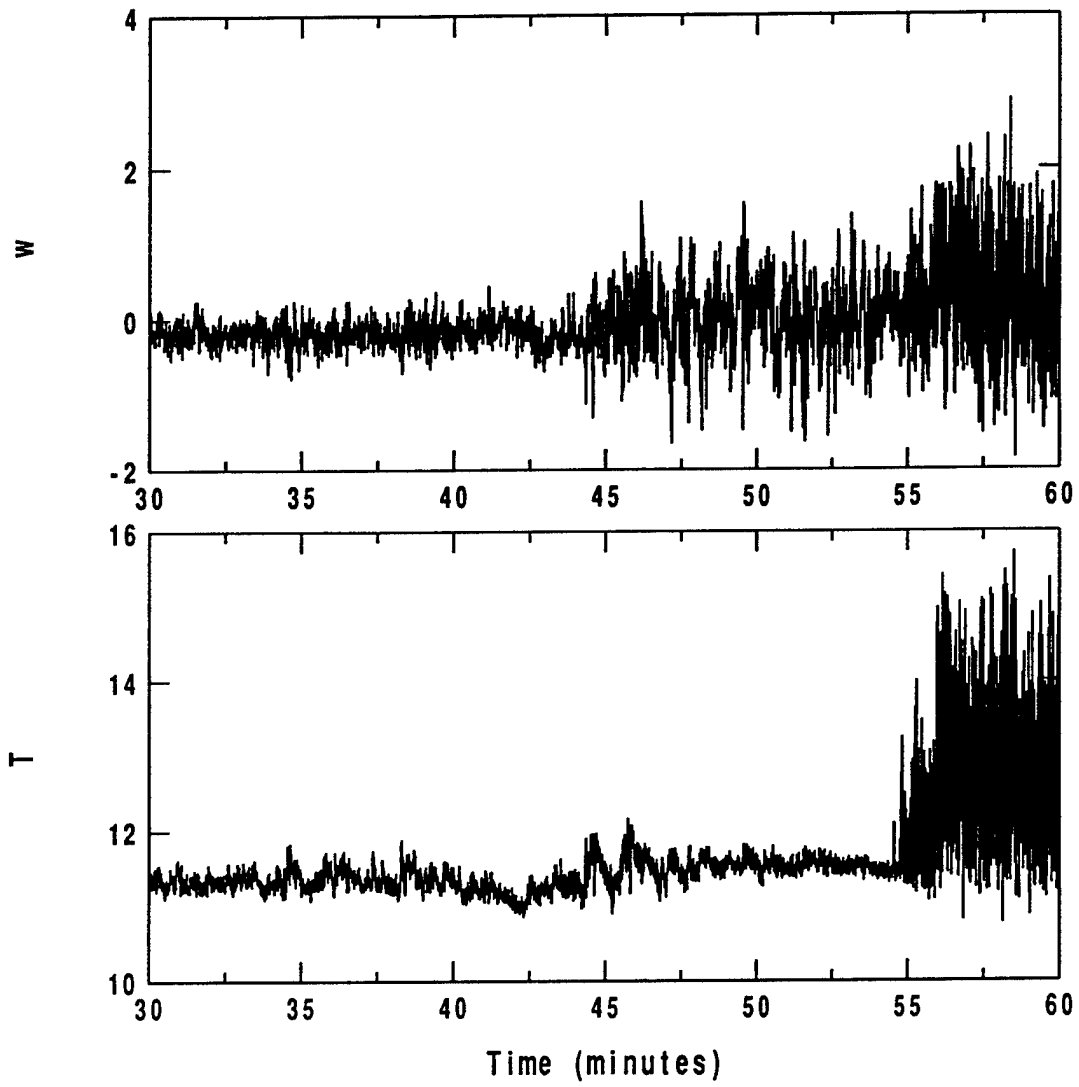


Figure 15. Record 297/241927



are unlikely.

Record 302/292331 is centered on a long wet period, with precipitation evenly distributed through the record. The entire record of 1 second average data is shown in Figure 16. The wind components show no unusual behavior anywhere in the record, while the virtual temperature only displays problems during four events towards the end of the record. Each virtual temperature event is a large jump in the mean and variance and lasts about 3 to 4 minutes.

Record 303/301834 is flagged for a jump in the Haar mean and variance of the vertical velocity. This record was also flagged for the 10 m sonic virtual temperature resolution and skewness. The jumps in the vertical velocity occur at the very end of the record, when precipitation was recorded, and appear unphysical.

In record 303/301934, the virtual temperature is flagged for a resolution problem. The very light winds and low turbulence levels would suggest that small virtual temperature fluctuations are likely, however, the resolution precludes accurately calculating the heat flux.

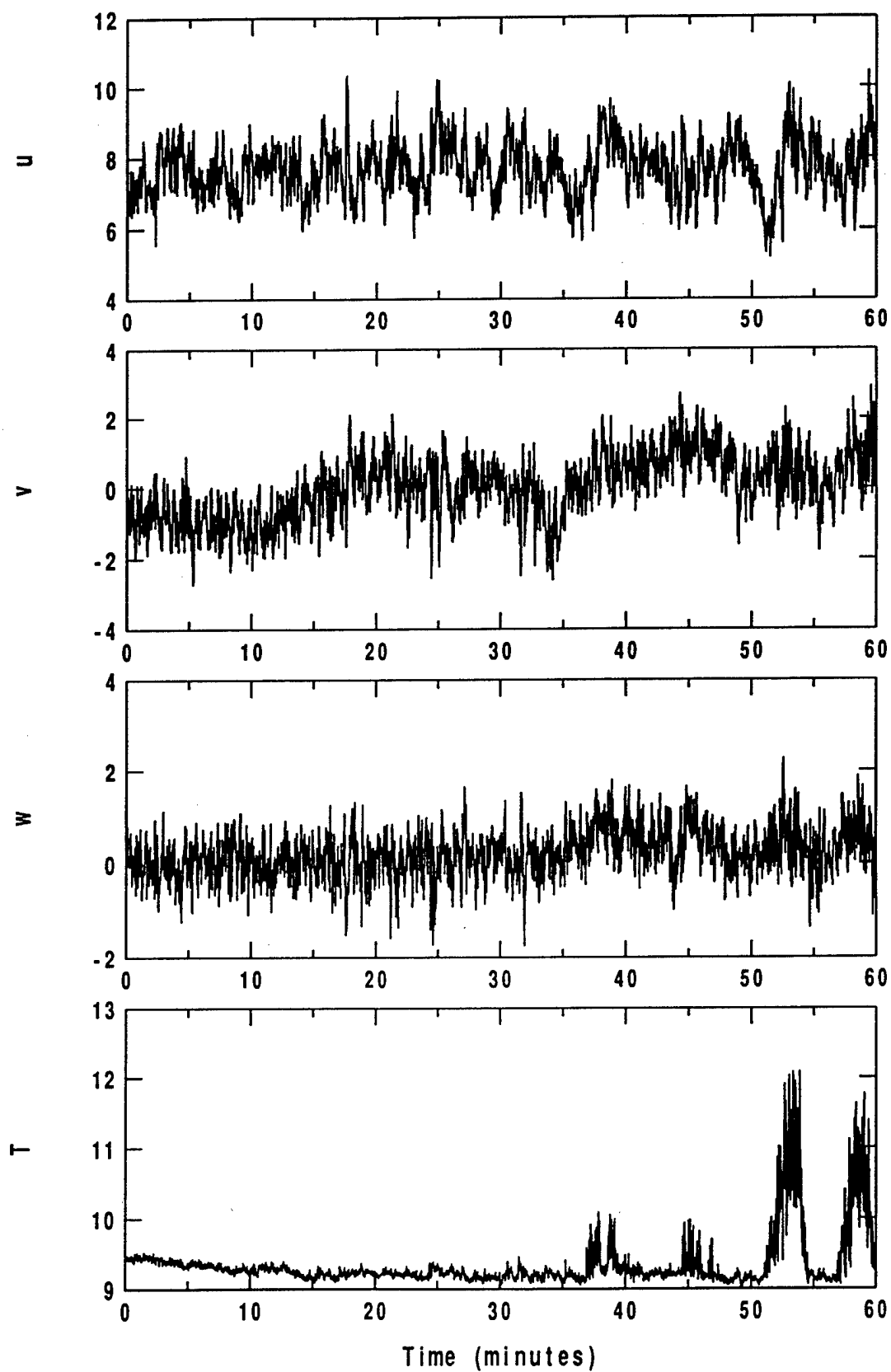
Record 307/030035 is flagged for a resolution problem with the virtual temperature and a jump in the vertical velocity variance. For this record the heat flux cannot be reliably calculated.

7.2 Unusual physical behavior

Record 281/081556 is hard flagged for a large jump in the vertical velocity variance, but classified as physical after inspection. In this case the wind sharply changes from 3 m/s at 200 degrees to 6 m/s at 160 degrees. At the wind shift, the vertical velocity and virtual temperature variances increase, and the mean virtual temperature slowly decreases for the remainder of the record. This situation is probably cool air advection from land with an associated rapid increase in the turbulence level.

Record 291/180815 is flagged for the virtual temperature resolution and the kurtosis and Haar variance of the vertical velocity, under very light south-westerly winds and dry conditions. The turbulence level sharply increases about half way into the record as the wind turns to more off shore. The

Figure 16. Record 302/292321.



apparent cause of this enhanced turbulence is the breakup of a stable layer, as the potential temperature gradient (48 - 7 m) decreases from 0.004 K/m to 0.001 K/m.

8 Soft flagged records

The number of records detected by flags is shown in Tables 3 and 4. The flux sampling flags in Table 4 are for the 10m sonic. The most frequent soft flag (337 records) is for the comparison of the friction velocity calculated from the cup profiles at the 4 lowest levels (7-29 m) and at the 4 highest levels (29-49 m). The two estimates have a correlation coefficient of 0.92, but the one based on the profile at higher levels is larger for 80 percent of the records. The largest positive differences occur with short fetch and light wind speeds, possibly associated with internal boundary layers.

Table 3. Number of 10 meter sonic records with soft flags

10m sonic flag	hard	soft
t resolution problem	3	0
u skewness	0	14
v skewness	0	12
t skewness	4	48
u kurtosis	0	20
v kurtosis	1	29
w kurtosis	1	22
t kurtosis	3	93
u Haar mean 5 min	1	55
v Haar mean 5 min	1	43
w Haar mean 5 min	0	3
t Haar mean 5 min	2	31
u Haar mean, 30 sec	0	214
v Haar mean, 30 sec	0	56
w Haar mean, 30 sec	0	62
t Haar mean, 30 sec	0	99
u Haar variance 5 min	0	10
v Haar variance 5 min	0	7
w Haar variance 5 min	6	15
t variance	5	10
stationarity of the wind	0	249
u dropouts	1	0
v dropouts	3	0
w dropouts	1	0
t dropouts	4	0

Table 4. Number of records with soft flags

soft flag	number
[wu] RFE and RN	83
[wu] Event	43
[wu] RSE	64
[wV] RFE and RN	105
[wV] Event	145
[wV] RSE	82
[wT] RFE and RN	136
[wT] Event	141
[wT] RSE	85
24/10 $\frac{d\theta}{dz}$ out of range	1
20/7 cup $\frac{du}{dz}$ out of range	5
profile u_* changes w/height 29/7 vs 48/29	337
stability changes w/height 47/10 vs 24/10	58
stability increases w/height	133
instability increases w/height	13
stability reversal, Tsfc, T10m, T47m	75
profile/sonic u_* intercomparison	195
precipitation	64

The next most frequent soft flag (249 records) is for nonstationarity of the horizontal wind. The winds at RASEX are in general moderate to strong and steady, but our relatively low threshold levels of 0.25 for RNu , RNv and RNS , and 0.9 for the wind speed ratio, capture 40 percent of the records. Increasing the threshold levels to 0.50 flags only 90 records (15 percent) as nonstationary.

The intercomparison of the friction velocity as calculated from the 10 m sonic and from the cup anemometer wind profile from the (7,15,20,29 m) levels, flags 195 records (32 percent) where the difference normalized by the average of the two values exceeds 50 percent. The mean friction velocity for all records is 0.231 m/s for the sonic and 0.236 m/s for the profile estimates, and the 2 estimates have a correlation of 0.65. The difference, sonic minus profiles, is moderately correlated with the heat flux ($R=0.45$), indicating a stability dependence.

Flags for the vertical structure of potential temperature find 133 records where the stability increases with height (47-10m versus 24-10 m), and only 13 records where the instability increases with height. Of the 133 cases where the stability increases with height, 88 (66 percent) are short fetch and probably are associated with thin internal boundary layers.

For flux sampling errors of the 10m vector stress, 82 records are flagged with a systematic error exceeding 0.25, 105 records have a random error or nonstationarity greater than 0.25, and 145 have a single flux event which is larger than twice the mean. The mean flux error quantities for all records excluding hard flags are 0.13 for *RSE*, 0.05 for *RN*, 0.19 for *RFE* and 1.8 for *Event*. All these quantities tend to be largest with light winds, especially the flux *Event*, which has a wind speed correlation of -0.52. The systematic error and the random error are weakly correlated ($R=0.36$) with each other.

The flux sampling errors of the along-wind component of the stress are similar but slightly less frequent than for the vector stress, which includes the cross-wind component. The along-wind component of the stress is flagged for *RSE* 64 records, *RFE* and *RN* 83 records and *Event* for 43 records. The number of records flagged for a flux *Event* is higher for the vector stress (145) than for the along-wind component stress (43), which indicates the cross-wind component of the stress contributes to a large fraction of the vector stress *Event* flags.

Flux sampling errors of the heat flux are slightly more frequent compared to the stress. The number of flags is *RSE* 85 records, *RFE* and *RN* 136 records and *Event* 141 records. The mean flux error measures are dominated by a few very large values when the record mean heat flux is near zero.

Not shown in Table 4 is the number of records flagged for cup wind speeds exceeding absolute limits. The cup at 7 m was flagged for 31 records with a mean wind speed less than 1.5 m/s, below which the cups are not accurate.

9 Summary

We have described techniques to calibrate, quality control and evaluate flux sampling errors for tower data. A set of hard flags are used to identify records

that may have instrumental problems. Our analysis of RASEX indicates that 1 percent of the 10 m sonic records and 3 percent of the 32 m sonic records have instrumental problems. Of the records which are objectively hard flagged, 30 (39) percent are verified as problems after visual inspection for the 10 (32) m sonic flags, respectively. The threshold values that define the hard flags are somewhat arbitrary, and in this analysis they detect unusual but real physical behavior, as well as intrumental problems.

Figure 17 shows all records and the circled 69 hard flagged records for the sonics at 10 and 32 m versus wind speed and direction. Clearly, "unusual" behavior is most likely to occur with weak winds. Also, hard flags are more likely during precipitation. 24 percent of all records include precipitation while 36 percent of the hard flagged records had precipitation. The behavior of several records indicates that precipitation is a likely cause of problems, particularly for the sonic virtual temperature.

Figure 18 shows all records (excluding the 25 verified hard flags) and a subset with large vector stress flux sampling errors for the sonics at 10 and 32 m. The flux sampling set selected here is $RSE > 0.5$, $RFE > 0.5$, $RN > 0.5$ or $Event > 3$, which captures 6 percent of the records. Large stress sampling errors are more likely with weak winds.

Figure 19 shows the same set, but for heat flux sampling errors. The sampling criteria capture 12 percent of the heat flux records. For the heat flux, large flux sampling errors are more evenly distributed with wind speed.

Figure 17.

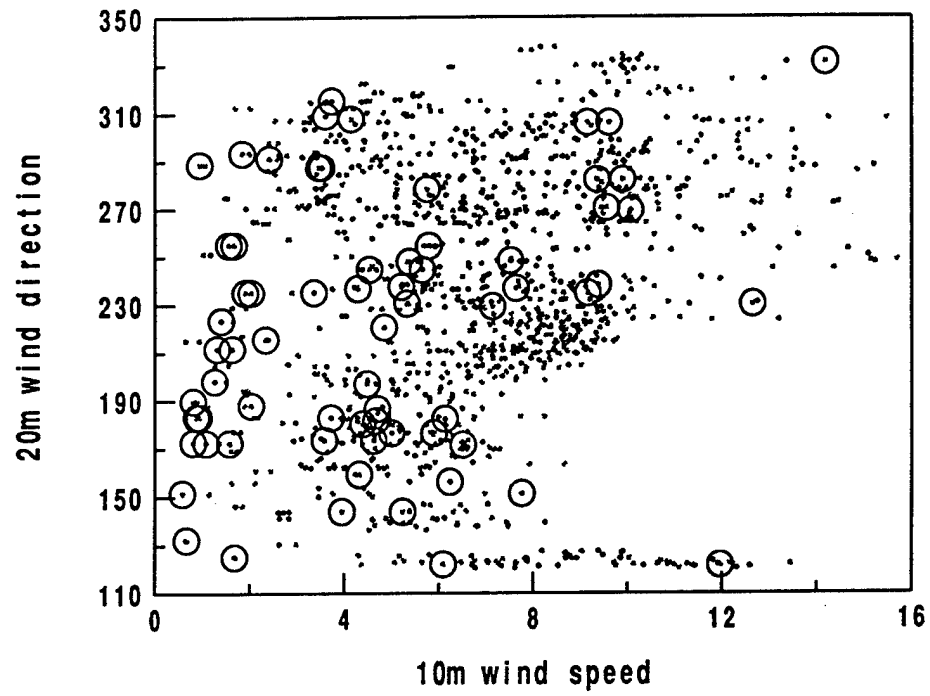


Figure 18.

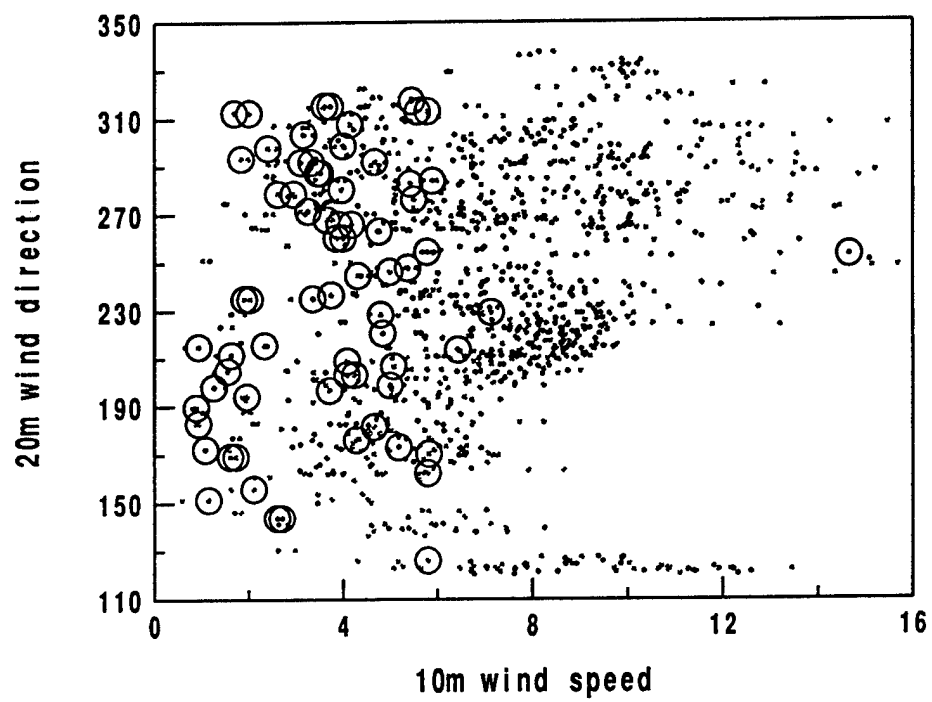
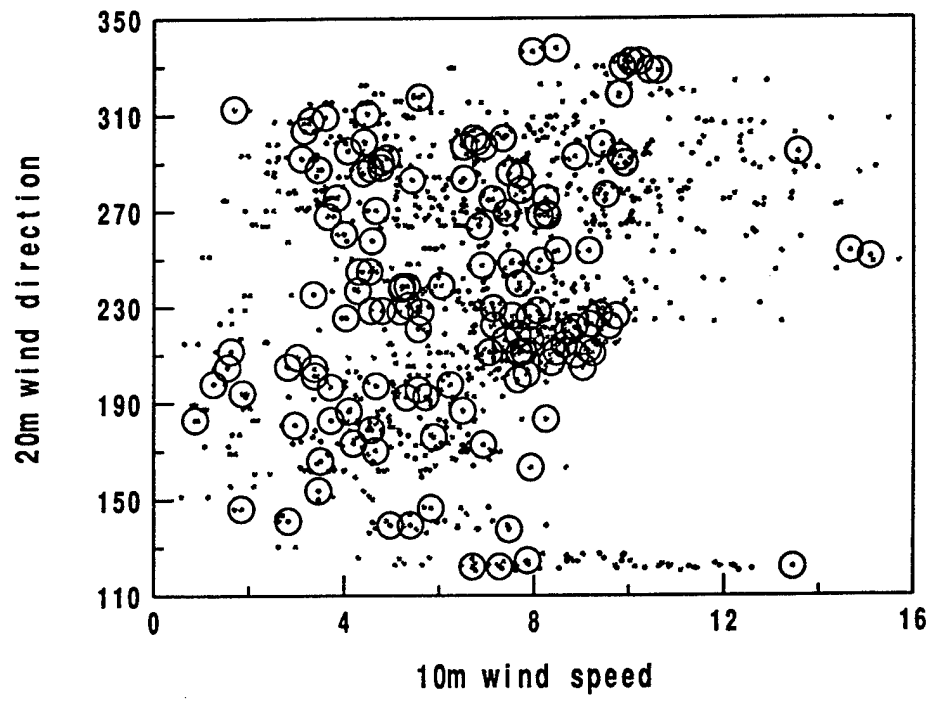


Figure 19.



List of figures

- Figure 1. The record mean momentum flux as a function of local averaging scale L for stationary flow.
- Figure 2. A verified hard flag for dropouts and a Haar jump in the variance of virtual temperature associated with precipitation.
- Figure 3. A verified hard flag detected by the Haar mean of virtual temperature occurring with precipitation.
- Figure 4. A verified hard flag detected by the skewness, kurtosis and Haar variance of virtual temperature.
- Figure 5. A verified hard flag detected by the skewness of virtual temperature, probably caused by precipitation.
- Figure 6. A 20 second section of a verified hard flag detected by the resolution parameter and skewness of virtual temperature.
- Figure 7. A verified hard flag detected by dropouts for virtual temperature probably caused by precipitation.
- Figure 8. Variance of the wind components and virtual temperature for intermittent turbulence in light and variable flow.
- Figure 9. Variance of the wind components and virtual temperature for a sharp transition from weak to strong turbulent flow.
- Figure 10. A gravity wave possibly initiated by a frontal passage.
- Figure 11. A verified hard flag detected by the skewness and kurtosis of virtual temperature possibly associated with precipitation.
- Figure 12. A verified hard flag detected by the Haar mean of the along-wind component. The kurtosis of virtual temperature is just below the hard flag threshold. Precipitation is a likely cause.
- Figure 13. A verified hard flag detected by the skewness, kurtosis and Haar variance of virtual temperature.
- Figure 14. A verified hard flag for virtual temperature probably associated with precipitation.
- Figure 15. A verified hard flag detected by the kurtosis and Haar variance of vertical velocity and virtual temperature, probably due to precipitation.
- Figure 16. A verified hard flag detected by spikes, skewness, kurtosis and Haar variance of virtual temperature, probably caused by precipitation.
- Figure 17. All records (dots) and the hard flagged records (circled).

Figure 18. All records (dots) and the large vector stress flux sampling error records (circled). Verified hard flags were excluded.

Figure 19. All records flags (dots) and the large virtual heat flux sampling error records (circled). Verified hard flags were excluded.

References

- Barthelmie, R. J., M. S. Courtney, J. Højstrup, and P. Sanderhoff, The Vindeby Project: A Description. Report R-741(EN), RisøNational Laboratory, DK4000, Roskilde, Denmark, 1994.
- Højstrup, J., and N. G. Mortensen, Flow-response characteristics and temperature sensitivity of the solent sonic anemometer, RisøNational Laboratory, DK4000, Roskilde, Denmark, August 24, 1995.
- Højstrup, J., J. Edson, J. Hare, M. S. Courtney, P. Sanderhoff, The RASEX 1994 experiments, Risø-R-788, RisøNational Laboratory, DK4000, Roskilde, Denmark (ISBN-87-550-2039-9), 1995.
- Mahrt, L., Eddy asymmetry in the sheared heated boundary layer, *J. Atmos. Soc.*, 48, 472-492, 1991.
- Mahrt, L., and J. F. Howell, The influence of coherent structures and microfronts on scaling laws using global and local transforms, *J. Fluid Mech.*, 260, 247-270, 1994.
- Mortensen, N. G., and Højstrup, J., The solent sonic - response and associated errors, Ninth Symposium on Meteorological Observations and Instrumentation, Charlotte, NC, March 1995.
- Schotanus, P., F. T. M. Nieuwstadt, and H. A. R. De Bruin, Temperature measurement with a sonic anemometer and its application to heat and moisture fluxes, *Boundary-Layer Meteorol.*, 26, 81-93, 1983.
- Sun, J., and L. Mahrt, Spatial distribution of surface fluxes estimated from remotely sensed variables, *J. Appl. Meteor.*, 33, 1341-1353, 1994.

Further work on the Kitaigorodskii roughness length model: A new derivation using Lettau's expression on steep waves¹

Carsten Hansen
Danish Meteorological Institute
DK-2100 Copenhagen Ø, Denmark

Søren E. Larsen
Risø National Laboratory
DK-4000 Roskilde, Denmark.

Abstract

A model for the roughness of the sea surface is derived by a combination of two ideas: a) Kitaigorodskii's (1973) about wavelets being roughness elements that move with their associated phase speed; b) Lettau's (1969) about the roughness of a field of roughness elements with characteristic dimensions.

The resulting sea surface roughness is related to a wave spectrum consisting of a Kitaigorodskii (1983) inertial form and a Phillips (1958) saturation form.

The variation of roughness with wave age is discussed and related to the corresponding variation of the Phillips B .

¹Symposium on Air-Sea Interaction in honour of Professor Sergei Kitaigorodskii, Helsinki, 29 September, 1994

1 Introduction

Kitaigorodskii (1973) derived an expression for the roughness of the sea surface. In his analysis the roughness of the wavelets were associated with the standard deviation of their height, following laboratory studies of the roughness of sand. The effects of the wave motion were included by considering the roughness in a coordinate system being translated with the phase speed, c , of the waves. For a wave spectrum of the form $F = Bk^{-4}$ (Phillips, 1958) where k is the wave number modulus and B is the Phillips constant, Kitaigorodskii found that $z_0 \propto B^{1/2}u_*^2/g$. Here u_* is the friction velocity and g acceleration due to gravity. From various reported experiments it appears that B varies about a factor 2 in the range 0.005 to 0.01, while z_0g/u_*^2 is found to vary more than a decade for the same data set. Undoubtedly, part of this variation is associated with measuring difficulties. Still the discrepancy seems worth studying.

Also many recent studies of the drag coefficient (e.g. Geernaert et al., 1987) indicate that z_0 of the sea depends on the wave age c_0/u_* , where c_0 is the phase speed of the dominating longer waves.

None of these phenomena are easily explainable in terms of the results derived by Kitaigorodskii (1973). In the present paper we therefore revisit his derivations to study the possibility of refining the results.

In section 2 we discuss the similarity between wavelets and land surface roughness elements, assuming that only wavelets with a steepness larger than a certain value ($s \simeq 0.25$) will give rise to flow separation, making the wavelet a roughness element. The roughness length corresponding to a given distribution of roughness elements over the surface is further evaluated, using an empirical formula developed by Lettau (1969). In Kitaigorodskii (1973) this discussion was based on the results of Nikuradse (1932, cfr. Kitaigorodskii 1973) relating the roughness of a surface with roughness elements to the characteristic size of the roughness element. Lettau's formula has the advantage that it further incorporates the ratio of the roughness sizes and the distances between them.

In section 3 we rederive the Kitaigorodskii (1973) transformation of the roughness length from a coordinate system being translated with the phase speed, c , of the individual waves to a fixed coordinate system. The formulation in section 2 is applied, based on the spectral properties at the wave number scale k of each wave, i.e. assuming linear wave theory, then $c = \sqrt{g/k}$. The average roughness length is then obtained by integration over the full wave number range.

In section 4 we shortly discuss the influence of orbital motions of longer waves as well as the long wave influence on short wave breaking and thereby on their steepness distribution. This subject, which leads to quantitative models about the dependence of the roughness length on wave age, swell and swell direction, will be pursued in a forthcoming paper.

2 The similarity between wavelets and land surface roughness elements

Lettau (1969) formulated a simple empirical relation to represent his experimental results on the boundary layer, formed above a distribution of bushel baskets on the frozen surface of Lake Mendota,

$$z_0 = \alpha_L h X/A, \quad (1)$$

where h is the height of the roughness element, X its crosswind area, A the horizontal area available to each element, and α_L is a dimensionless coefficient of order unity. Eq. (1) was found to be valid for fairly isolated roughness elements in the range $X/A = 0.01$ to 0.4 (Garratt, 1992).

An application of this methodology for analysing an inhomogeneous distribution of roughness elements was given by Kondo and Yamazawa (1986), who examined roughness heights over some rural towns and cities. To represent the variation of the measured roughness length, Kondo and Yamazawa suggested the relation

$$z_0 = \alpha_K \frac{\sum A_i H_i}{A}; \alpha_K = 0.25 \quad (2)$$

where H_i is the height of individual buildings or forest areas, A_i is the horizontal cross section area occupied by each roughness element, and A is the total area.

Equation (2) is similar to Lettau's formula (Eq. 1) because there is a uniform aspect ratio $\sum A_i H_i / \sum X_i H_i$, where X_i is the vertical crosswind area of individual roughness elements. Therefore, we may apply the result of Kondo and Yamazawa (1986) to randomly distributed wavelets, which also have a distribution of heights and lengths. We assume that the overall roughness length is obtained by a direct average of Eq. (1) over this distribution.

The principal feature of the flow across roughness elements is the formation of flow separation over the corner(s) of the roughness elements, with reattachment on the lee side and a subsequent redistribution of the momentum deficit within the atmospheric boundary layer. The complex nature of boundary layer flow makes it very speculative to estimate the force on each roughness element. Therefore, we build our approach on the empirical relation (Eq. 1). We emphasize, though, that the resulting profile wind speed near the height of the roughness elements exerts a force on the individual roughness element determined by a bluff body resistance coefficient of order unity¹. To verify that this is indeed the case, insert Eq. (1) into the logarithmic profile at the roughness height h ,

$$\frac{U(h)}{u_*} = \frac{1}{\kappa} \ln \frac{z}{z_0},$$

where $U(h)$ is the profile wind speed at height h , u_* the friction velocity and $\kappa = 0.4$ the von Karman constant.

Let l be the distance in the wind direction between the roughness elements; we then find the individual resistance coefficient

$$D = \frac{l}{h} \left(\frac{u_*}{U(h)} \right)^2 = \frac{l}{h} \left(\kappa / \ln \frac{l}{\alpha_L h} \right)^2.$$

With a characteristic value $\frac{l}{h} = 10$ we have $D = 0.3$, and with $\frac{l}{h} = 100$ $D = 0.8$. For waves we may estimate X/A as the roughness wavelet height to the wavelength ratio, h/L , times the fraction of wavelets, where flow separation occurs.

We assume that flow separation occurs where the steepness exceeds a critical value, s_0 . The value of s_0 was evaluated by Csanady (1985) in his review on energy and momentum transfer to centrimetric waves. An experiment by Kawai (1982, Csanadys figure 7) indicates that flow separation occurs at a wave height to wavelength ratio $h/\lambda \approx 0.08$. This corresponds to a steepness $s_0 = \pi h/\lambda \approx 0.25$. As the air and water flow for these laboratory waves of wavelength ≈ 10 cm is characterized mainly by a nonrotational water orbital flow and a logarithmic wind profile, we expect the flow to be kinematically similar to the flow over the somewhat longer waves of a length of typically one meter, which we consider to be dominant roughness elements on a well-developed sea.

Consider a wavelet with wave number k and amplitude a . We take the following definition of the equivalent roughness element height of a wavelet:

¹The common word in hydrodynamical textbooks is "drag coefficient". However, we use the word "resistance" in order to avoid confusion with the boundary layer surface drag coefficient.

$$h = 2a \text{ for } a > a_0 \text{ and } h = 0 \text{ for } a < a_0,$$

where a_0 is the amplitude corresponding to the critical wave steepness discussed above.

We may then rewrite Eq. (1) as:

$$z_c = \alpha_L h X / A = \frac{2}{\pi} \alpha_L a^2 k = \frac{2}{\pi} \alpha_L s^2 k^{-1} \quad \text{for } s > s_0$$

$$z_c = 0 \quad \text{for } s < s_0, \quad (3)$$

where $s = ak$ is the steepness of the wavelet and z_c is the roughness of the wavelet in the coordinate system moving with the wave. In that coordinate system, the overall roughness length is the average z_c of all wavelets.

We assume that the wave field is a random superposition of harmonic components in a narrow wave-number band, i.e. all of essentially one wave number scale \bar{k} .

The wave number scale \bar{k} is defined from

$$\langle \eta^2 \rangle \bar{k} = \int_k^\infty k' F(k') k' dk' \quad (4)$$

where $F(k)$ is the one-dimensional wave number spectrum and $\eta = \eta(x, t)$ is the surface displacement.

Note that if $F(k)$ is of the Phillips (Phillips, 1958) saturation form, Bk^{-4} , then $\bar{k} = 2k$ and $\langle \eta^2 \rangle \bar{k} = Bk^{-1}$.

To determine z_c for waves of a given angular frequency ω with a corresponding wave number $k = \omega^2 g$, we specify the amplitude of waves from

$$\langle \eta^2 \rangle = \int_k^\infty F(k') k' dk' = \int_\omega^\infty S(\omega) d\omega, \quad (5)$$

where $S(\omega)$ is the omnidirectional frequency spectrum.

It is convenient to associate the steepness, s , of such waves with the local maximum slope between every two successive local wave maxima and normalize the steepness with the overall slope parameter $\langle \eta^2 \rangle^{\frac{1}{2}} \bar{k}$

If the surface displacement $\eta(x, t)$ has a narrow spectrum, then the square of the normalized steepness is expressed in the parameter

$$y = \frac{s^2}{(2\langle \eta^2 \rangle \bar{k}^2)}$$

The probability distribution of y is described by an exponential density distribution function

$$f(y) = e^{-y}, \quad (6)$$

i.e. the probability of finding a wave steepness in an interval dy is $f(y)dy$ (see e.g. the review by Srokosz (1990) of Longuet-Higgins' exceedance theory). The observed wave spectra are, however, not sufficiently narrow for Eq. (6) to be valid. In fact the mean square wave slope determined from integration over the spectrum ($\int_k^\infty k^2 F(k) k dk$) becomes indefinitely high for the case of a Phillips saturation spectrum (Phillips, 1958). But the underlying assumption that the wavy sea surface is a superposition of a spectrum of linear wave trains with random phases is probably violated by wave breaking events at high wave number scales. Therefore it is likely that Eq. (6) is still an adequate formulation.

In Appendix A we demonstrate the result of a numerical reconstruction of a one-dimensional sea surface from a spectrum of the Phillips form. From this reconstruction we determine the distribution of wave heights $2a$ and wavelengths λ defined as the maximum sea level difference and distance between successive upcrossings through the mean sea level. The distribution of the quantities $2a/\lambda$ is examined (the wave slope) and the frequency of waves exceeding various critical slopes is calculated as functions of $(2a)^2/\lambda$ (proportional to the wavelet roughness of Eq. 3). We find that the reconstructed mean wavelet roughness length compares well with the result (Eq. 10 below) which is based on the assumption of Eq. (6).

The wavelet roughness of Eq. (3) is expressed as a function of the normalized square steepness y :

$$z_c(y) = \frac{2}{\pi} \alpha_L \langle \eta^2 \rangle \bar{k} y \quad \text{for } s > s_0$$

$$z_c = 0 \quad \text{for } s < s_0, \quad (7)$$

The characteristic value of \bar{z}_c for a given wave number \bar{k} can now be found from Eq. (7) with the above considerations as an integral of the form:

$$\int_x^{\infty} z_c(y) f(y) dy$$

with

$$x = \frac{s_0^2}{2\langle\eta^2\rangle\bar{k}^2}. \quad (8)$$

However, it was shown experimentally by Rapp and Melville (1990) that waves break (by spilling breaking) when their steepness s exceeds a value of about 0.3^2 . This is close to our value of $s_0 = 0.25$, and may even coincide. Therefore, we approximate the integral by considering the individual roughness length of a wave at any $y > x$ approximately equal to $z_c(x)$. Thus we estimate the average roughness as

$$\bar{z}_c = z_c(x) \int_x^{\infty} f(y) dy = z_c(x) e^{-x}, \quad \text{where } x = \frac{s_0^2}{2\langle\eta^2\rangle\bar{k}^2}. \quad (9)$$

Inserting Eq. (7) yields

$$\bar{z}_c = \alpha_L \frac{2}{\pi} \langle\eta^2\rangle \bar{k} x e^{-x} = \alpha_L \frac{s_0^2}{\pi} e^{-x} \bar{k}^{-1}. \quad (10)$$

A theoretical upper bound for the roughness length of young waves

Under certain hypothetical conditions that may be established in a wave tunnel experiment or in case of a strong, steady wind blowing perpendicularly off a straight coastline, the wave field may be brought to a very high energy level with incipient breaking on almost all wave crests. In such a case x is somewhat smaller than one, so that the probability e^{-x} that a wave crest is a roughness element is close to unity. In such circumstances the wave phase speed is much smaller than the wind speed, and

²We thank Professor Y. Papadimitrakakis for pointing out to us that the steepness of Rapp and Melville corresponds to our definition.

thus the effect of moving roughness elements described in section 3 can be ignored. Then from Eq. (10) the upper bound, which the roughness length cannot exceed, may be approximated as

$$z_0^u = \overline{z_c}(x=0) = \alpha_L \frac{s_0^2}{\pi} \bar{k}^{-1} . \quad (11)$$

It is convenient to rewrite this expression in terms of the *inverse wave age* u_*/c_0 , where c_0 is the phase speed of the spectral peak wave component. We define the dimensionless angular frequency scaled with the friction velocity ω_* and g as:

$$\omega_* = \omega u_*/g . \quad (12)$$

Assuming linear gravity wave dynamics we have $\omega_* = u_*/c$, and the inverse wave age is equal to a dimensionless peak angular frequency $\omega_{0*} = \omega_0 u_*/g = u_*/c_0$. This follows from the linear dispersion relation $c = \omega/k = \sqrt{g/k} = g/\omega$. For extremely steep waves the spectral peak wave number is approximately equal to \bar{k} . The dimensionless version of Eq. (11) then becomes

$$\hat{z}_0^u = \alpha_L \frac{s_0^2}{\pi} (u_*/c_0)^{-2} . \quad (13)$$

In Eq. (13) $\hat{z}_0 = z_0 \frac{g}{u_*^2}$ is the dimensionless roughness length, sometimes called the Charnock's constant (Charnock, 1959).

There is a fundamental difference between such steep waves and Lettau's experiment, as steep waves produced in laboratory experiments tend to be long-crested and cross-wind oriented while Lettau (and others) made experiments with roughness elements that have horizontally isotropic geometries. Also for a well-developed oceanic wave field the roughness waves tend to have a broad directional distribution. This means that a specific value of Lettau's constant α_L cannot be inferred from one wave state to another.

However, the similarity may apply to an order of magnitude. Taking $\alpha_L = 1.0$, $s_0 = 0.25$ we find at the inverse wave age $u_*/c_0 = 1.0$ that $\hat{z}_0^u = 0.02$, which is typical for young laboratory waves. This value corresponds roughly to the bulk mean of published data from laboratory experiments as compiled e. g. by Toba et al. (1990).

As a wave field develops and the inverse wave age becomes smaller than of order unity, the effective roughness length of the spectral peak waves begins to drop off,

and the significant contribution to the overall roughness length is transferred to high wave number components on the spectral tail. This will be quantified in the next chapter by application of Kitaigorodskii's (1973) method. In order for the observed rate of energy increase near the spectral peak to be maintained, this shift to higher wave numbers of the roughness elements and associated momentum transfer demands a different mechanism to be responsible for wave energy input near the spectral peak. This is a qualitatively good reason that the spectral level at high frequencies, i.e the saturation level B of the Philips range is observed to decrease with increasing wave age. The consequence is that the roughness length drops far below the upper limit of Eq. (13), even when the Kitaigorodskii effect is applied.

3 Extension of the Kitaigorodskii (1973) approach

The roughness length, z_0 , of a flow over a flat surface is defined in terms of the logarithmic profile as the height in which the wind speed becomes zero,

$$u(z)/u_* = \frac{1}{\kappa} \ln \frac{z}{z_0} . \quad (14)$$

Once the logarithmic profile is established in one inertial system, a logarithmic profile is found also in any other reference system moved with constant horizontal speed c . In the wavelet-following reference system the velocity profile is expressed in terms of the roughness length z_c defined in Eq. (3).

$$(u(z) - c)/u_* = 1/\kappa \ln (z/z_c) . \quad (15)$$

Thus z_0 can be referred to z_c by a combination of the logarithmic profiles (14) and (15), which yields

$$z_0 = z_c \exp \left(-\kappa \frac{c}{u_*} \right) . \quad (16)$$

Note that in this derivation we assume that all roughness generating wavelets travel along the wind direction. This assumption is appropriate, but an exact quantification is difficult, since the force on waves propagating in a high angle to the wind is strongly reduced. Neglecting this directional filter may cause the calculated roughness to be too high, or conversely be reflected in a value for the Lettau constant α_L

somewhat lower than unity. However, it is our hope that the directional filter does not change considerably with the other parameters, i.e. with B .

We want to account for the variation of the phase speed with wave number k that appears in our expression (Eq. 10) for the moving-frame roughness length. Motivated by the experience that the effective roughness length is estimated as the sum over each roughness element in Lettau's expression, we will calculate the wave roughness as an integral over the wave number domain. The contribution from an infinitesimal wave number interval dk to the moving-frame roughness length \bar{z}_c of Eq. (10) is found from the differential of Eq. 4:

$$d(\langle \eta^2 \rangle \bar{k}) = kF(k) kdk .$$

Then from Eq. (10)

$$d\bar{z}_c = \alpha_L \frac{2}{\pi} x e^{-x} kF(k) kdk , \quad (17)$$

where x is found from Eq. (8) using the integral expressions (4) and (5) for the spectral tail above k .

The next step is to multiply Eq. (17) with Kitaigorodskii's filter z_0/z_c (Eq. 16) at each wave number. The filter is applied at the integral scale $\bar{\omega}_* = \bar{k}^{1/2}$. For simplification we rewrite the expressions in terms of the dimensionless angular frequency $\omega_* = \omega u_* / g = u_* \sqrt{k/g}$. The omnidirectional frequency spectrum $S(\omega)$ is defined such that $S(\omega)d\omega = F(k)kdk$, and the dimensionless frequency spectrum is $S_*(\omega_*) = S(\omega)g^2/u_*^3$. We then find for the differential roughness length in the fixed reference frame:

$$d\hat{z}_0 = \frac{g}{u_*^2} dz_0 = \alpha_L \frac{2}{\pi} x e^{-x} e^{-\kappa/\bar{\omega}_*} \omega_*^2 S_*(\omega_*) d\omega_* . \quad (18)$$

In figure 1 we present the contribution to \hat{z}_0 for different frequencies with the integral scale $\bar{\omega}_* = \bar{k}^{1/2}$, assuming a wave spectrum consisting of a Phillips (1958) saturation form $S(\omega) = 2Bg^2\omega^{-5}$ above some frequency ω_g and an inertial range of the form $S(\omega) = \alpha g u_* \omega^{-4}$ for $\omega < \omega_g$ as suggested by Kitaigorodskii (1983). The two ranges are matched at the frequency ω_g so that $\alpha \omega_g g u_* = 2Bg^2$.

A special case: spectral tail of an all-over Phillips form

We consider the simplified case, where the spectrum is of the form $S(\omega) = 2Bg^2\omega^{-5}$ over the whole spectral tail. This corresponds to the curves ' α_∞ ' in figure 1. Then x has the constant value

$$x = \frac{s_0^2}{4B},$$

and the term $xS(\omega)$ in Eq. (18) becomes simply $s_0^2g^2\omega^{-5}$, i.e. the saturation level B only remains in the e^{-x} term. Eq. (18) becomes

$$d\hat{z}_0 = \frac{g}{u_*^2} dz_0 = \alpha_L \frac{s_0^2}{\pi} e^{-x} e^{-\kappa/\bar{\omega}_*} \omega_*^{-3} d\omega_*.$$

Integration over all frequencies yields

$$\hat{z}_0 = \frac{g}{u_*^2} z_0 = \alpha_L \frac{2s_0^2}{\kappa^2\pi} e^{-x}, \quad (19)$$

Equation (19) yields a characteristic value of $\hat{z}_0 = 0.026$ for $B = 0.01$, $s_0 = 0.25$, $\kappa = 0.4$ and Lettau's constant ambiguously chosen as $\alpha_L = 0.5$.

4 Discussion

Our result (Eq. 19) differs from Kitaigorodskii (1973) in that the wave statistics only enters through the probability that a wave of any wave number scale reach the threshold steepness. This probability has, of course, to be derived from the spectrum.

We consider the most realistic case when Phillips' saturation spectrum dominates the spectrum in the wave number frequency range of the roughness elements. The dimensionless roughness length \hat{z}_0 is a function of Phillips' constant B , through the term e^{-x} in Eq. (19). This dependence is shown in figure 2 for the cases that the lower steepness limits for flow separation are $s_0 = 0.2$, $s_0 = 0.25$ and $s_0 = 0.3$. The other numbers are: α_L chosen as 0.5 and $\kappa = 0.4$.

It is seen that \hat{z}_0 is increased by a factor of order 10 (depending on the value of s_0) when B is raised from 0.005 to 0.01.

Thus we have obtained a formulation that has the potential that it can explain large variations of the roughness length as a consequence of a varying level of the wave spectral tail, within reasonable limits.

For example, various experiments seem to indicate that the level, B , of Phillips' saturation range depends on the wave age c_0/u_* . The dependence may be expressed as a power law, $B = B_0 (c_0/u_*/40)^{-\gamma}$, where B has the reference value B_0 at very developed waves with $c_0/u_* = 40$. Figure 3 shows the dependence of \hat{z}_0 on the inverse wave age u_*/c_0 for various choices of the exponent γ , when $s_0 = 0.25$ and $\alpha_L = 0.5$, and $B_0 = 0.05$. We note that a modest value γ in the range $0.5 < \gamma < 1.0$ has the consequence that the dimensionless roughness length \hat{z}_0 is approximately proportional to the inverse wave age u_*/c_0 in the range $0.05 < u_*/c_0 < 0.1$.

Figure 4 shows a comparison between observations as compiled by Donelan et al. (1993) and our result for the cases $\gamma = 0.5$ and $\gamma = 1.0$. The comparison demonstrates that our model is realistic. Also shown is a modified version of the upper bound with Eq. (13) as its high-frequency asymptote. This upper bound is derived from Eq. (18) for a simplified spectrum of the form

$$S(\omega) = 2Bg^2\omega^{-5} \text{ for } \omega \geq \omega_0, \text{ and } S(\omega) = 0 \text{ for } \omega < \omega_0,$$

which yields

$$\hat{z}_0^u = \alpha_L \frac{2s_0^2}{\kappa^2\pi} \left(1 - (1 + \kappa/\bar{\omega}_*)e^{-\kappa/\bar{\omega}_*}\right). \quad (20)$$

In order to obtain Eq. (13) as a high-frequency asymptote, the result is plotted as a function of the (dimensionless) integral frequency scale, i.e. the abscissa is $u_*/c_0 = \bar{\omega}_*$.

The directional filter on the calculated roughness length is probably only a weak function of wave age. However, the spectral level is considerably affected by the presence of longer waves, as short waves are modulated by the longer waves in the wave spectrum via strong nonlinear interactions. It can be shown, following the results of Phillips (1981), that B is an exponential function of the long-wave instantaneous amplitude, providing the long-wave steepness is small. As a consequence of the exponential probability density function e^{-y} , wavelets have a considerable chance of reaching the level s_0 only on the higher crests of longer waves. Thus the

overall probability of roughness wavelets will decrease with increasing wave age. Simultaneously the orbital water motions on the crests of the longer waves enter the Kitaigorodskii expression (Eq. 16) in addition to the wave phase speed and thereby further decrease the effective roughness. In a forthcoming paper we will demonstrate that this can be quantified in terms of an equivalent decrease of the Phillips' B in the expression (Eq. 19).

Acknowledgement

This work has been supported by US Office of Naval Research and the Danish Technological Scientific Research Council.

References

- Charnock, H. (1959). Wind stress on a water surface. *Quart. J. Roy. Meteorol. Soc.*, **81**, 639-640.
- Csanady, G. T. (1985), Air-sea momentum transfer by means of short-crested wavelets. *J. Phys. Ocean.*, **15**, 1486-1501.
- Donelan, M. A., F. W. Dobson, S. D. Smith, and R. J. Anderson (1993). On the dependence of sea surface roughness on wave development. *J. Phys. Oceanogr.*, **23**, 2143-2149.
- Garratt, J. R. (1992), *The Atmospheric Boundary Layer*, Cambridge University Press, 316 pp.
- Geernaert, G. L., S. E. Larsen, and F. Hansen (1987). Measurements of the wind stress, heat flux and turbulence intensity during storm conditions over the North Sea. *J. Geophys. Res.*, **92C**, 13,127-13,139.
- Kawai, S. (1982), Structure of air flow separation over wind wave crests. *Boundary-Layer Meteorol.*, **23**, 503-521.
- Kitaigorodskii, S.A. (1973). *The Physics of Air-Sea Interaction*, Israel Program for Scientific Translations.

Kitaigorodskii, S.A. (1983). On the theory of the equilibrium range in the spectrum of wind-generated gravity waves. *J. Phys. Ocean.*, **13**, 817-827.

Kondo, J., and H. Yamazawa (1986). Aerodynamic roughness over an inhomogeneous ground surface. *Boundary-Layer Meteorol.*, **35**, 331-348.

Lettau, H. (1969). Note on aerodynamic roughness-parameter estimation on the basis of roughness-element distribution. *J. Appl. Met.*, **8**, 820-832.

Phillips, O. M. (1958). The equilibrium range in the spectrum of wind-generated waves. *J. Fluid Mech.*, **4**, 426-434.

Rapp, R. J. and W. K. Melville (1990). Laboratory measurements of deep water breaking waves. *Phil. Trans. R. Soc. Lond.*, **A331**, 735-780.

Srokosz, M. A. (1990). Wave statistics. *Surface waves and fluxes*, (G. L. Geernaert and W. J. Plant, Eds.), Kluwer Academic Publishers, 285-332.

Toba, Y., N. Iida, H. Kawamura, N. Ebuchi, and I. S. F. Jones (1990). Wave dependence on sea-surface wind stress. *J. Phys. Oceanogr.*, **20**, 705-721.

Appendix A: A numerical reproduction of surface wave roughness elements

In order to test the applicability of the simplified probability density function of Eq. (6), we performed a numerical reconstruction of waves. A series of harmonic functions was defined with wave numbers k in the range $[1.01, 100]$ distributed at intervals $\Delta k = 0.02k$. The amplitudes define a variance spectrum of the form $S_k = 3k^{-4}$ for $k \leq 1$, and $S_k = 0$ for $k > 1$, so that it integrates to the variance $\int_0^\infty S_k dk = 1$.

The phase of each harmonic was chosen at random for a series of calculations with different initialisations of the random number generator. The sum of the functions then represents the wavy surface. From this sum we determined the trough to crest level difference H between every two successive upcrossings of the zero level, and the distance λ between each upcrossing.

Then the wave steepness was defined as $s = \pi H/\lambda$. We chose series of the critical steepness s_0 normalized with the mean steepness determined from the spectrum to form the parameters $x = s_0^2/(2\langle\eta^2\rangle\bar{k}^2)$.

In Fig. A1 we show the number density distribution over H^2/λ of the fraction of waves whose steepness $\pi H/\lambda > s_0$, plotted for various values of the parameter x . It is seen that there is a wide distribution of heights corresponding to each critical steepness. The density distribution level is seen to depend on x like $\exp(-1.3x)$ rather than the $\exp(-x)$ dependence we expect from the simple hypothesis of a narrow spectrum.

In Fig. A2 we show the calculated mean roughness height $\langle H_0^2/L \rangle$, where L is the distance between two successive roughness waves, and H_0 is the critical height defined by $\pi H_0/\lambda = s_0$. This result is compared with the model of the text, $\langle H_0^2/L \rangle = x \exp(-x)$ and a best fit similar expression $\langle H_0^2/L \rangle = 2.0x \exp(-1.3x)$.

The difference between the two exponents $-1.3x$ or $-x$ is a consequence of the chosen “zero-upcrossing” selection procedure of roughness elements, which is not exactly the way the wind flow senses the surface. Because of this ambiguity we conclude that the exponent $-x$ provides a model that resembles the numerical simulation “close enough”.

Figure Legends

Figure 1. The contribution to the sea surface roughness from different parts of the wave spectrum, $S(\omega)$, derived from Eq. (16) where $\alpha_L = 0.5$, $s_0 = 0.25$. The importance of the characteristic parameters of $S(\omega)$ is illustrated. A very high value of $\alpha(\alpha_\infty)$ means that the spectrum has the Phillips saturation on the whole range.

Figure 2. The variation of z_0 with Phillips' constant B , for the case when the saturation range dominates the contributions to z_0 (case α_∞ cf. Fig. 1). The variation is shown for different lower steepnesses of flow separation, $s_0 = 0.2, 0.25$, and 0.3 .

Figure 3. The predicted variation of z_0 with inverse wave age for different values of the parameter γ in the wave age dependency of Phillips' constant $B \sim (c/u_*)^{-\gamma}$.

Figure 4. A comparison of our model with published field and laboratory data compiled by Donelan et al. (1993, from their figure 2). Full lines: Our model as in Fig. 3 with $\gamma = 0.5$ and $\gamma = 1.0$; broken line: Eq. (20).

Figure A1. Results from a numerical experiment showing the number density distributions for H^2/λ , H being the maximum level difference between two zero crossings λ apart, for the steepness $\pi H/\lambda > s_0$, where s_0 is a lower limit steepness. The curves reflect different values of s_0 .

Figure A2. Calculated mean roughness height $\langle H_0^2/L \rangle$, with L being the distance between two succession roughness waves and H_0 a characteristic height given by $\pi H_0/\lambda = s_0$. The simulated results are compared with two different exponential variations corresponding to the formulation (Eq. 10) in section 2.

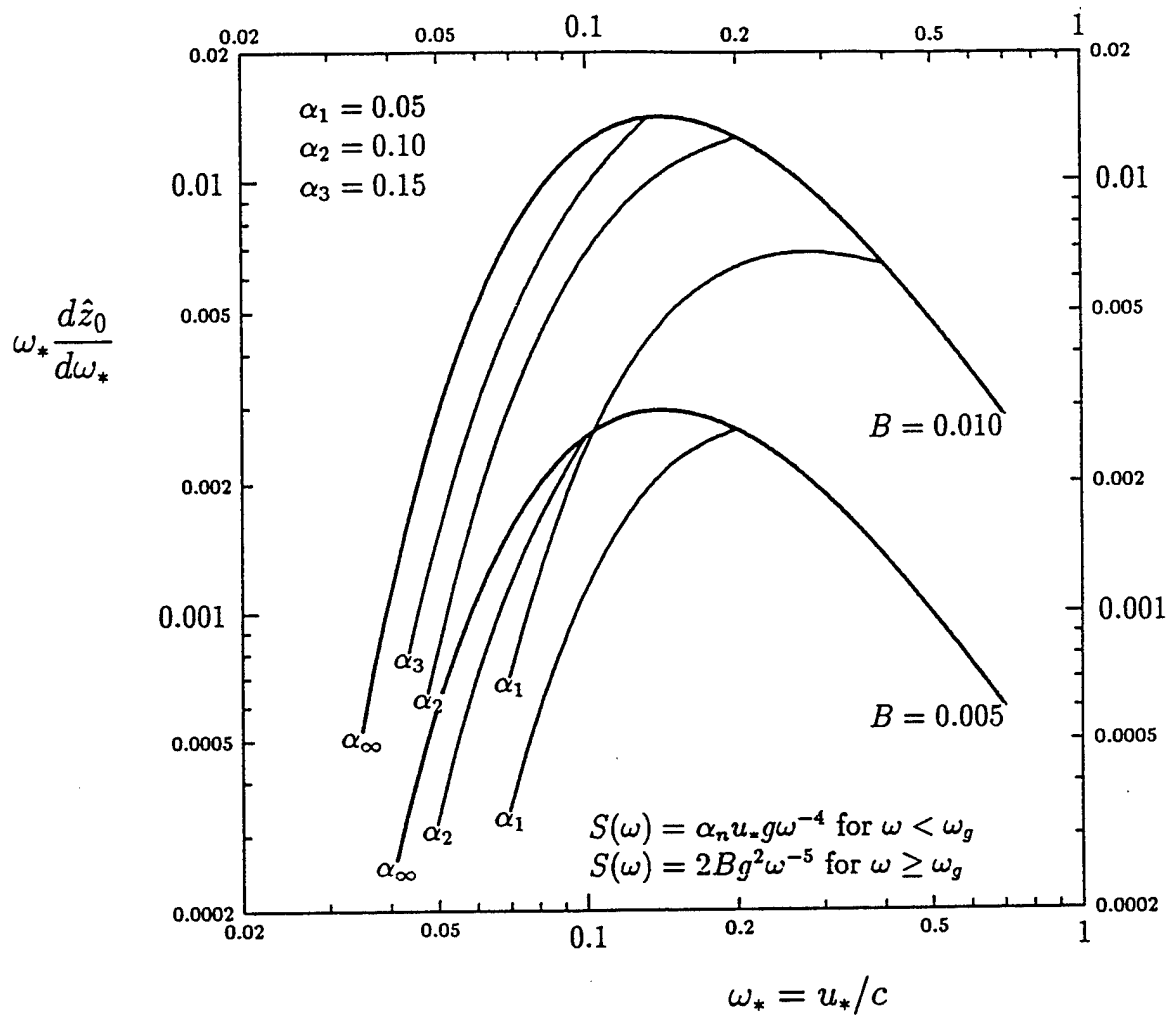


Figure 1

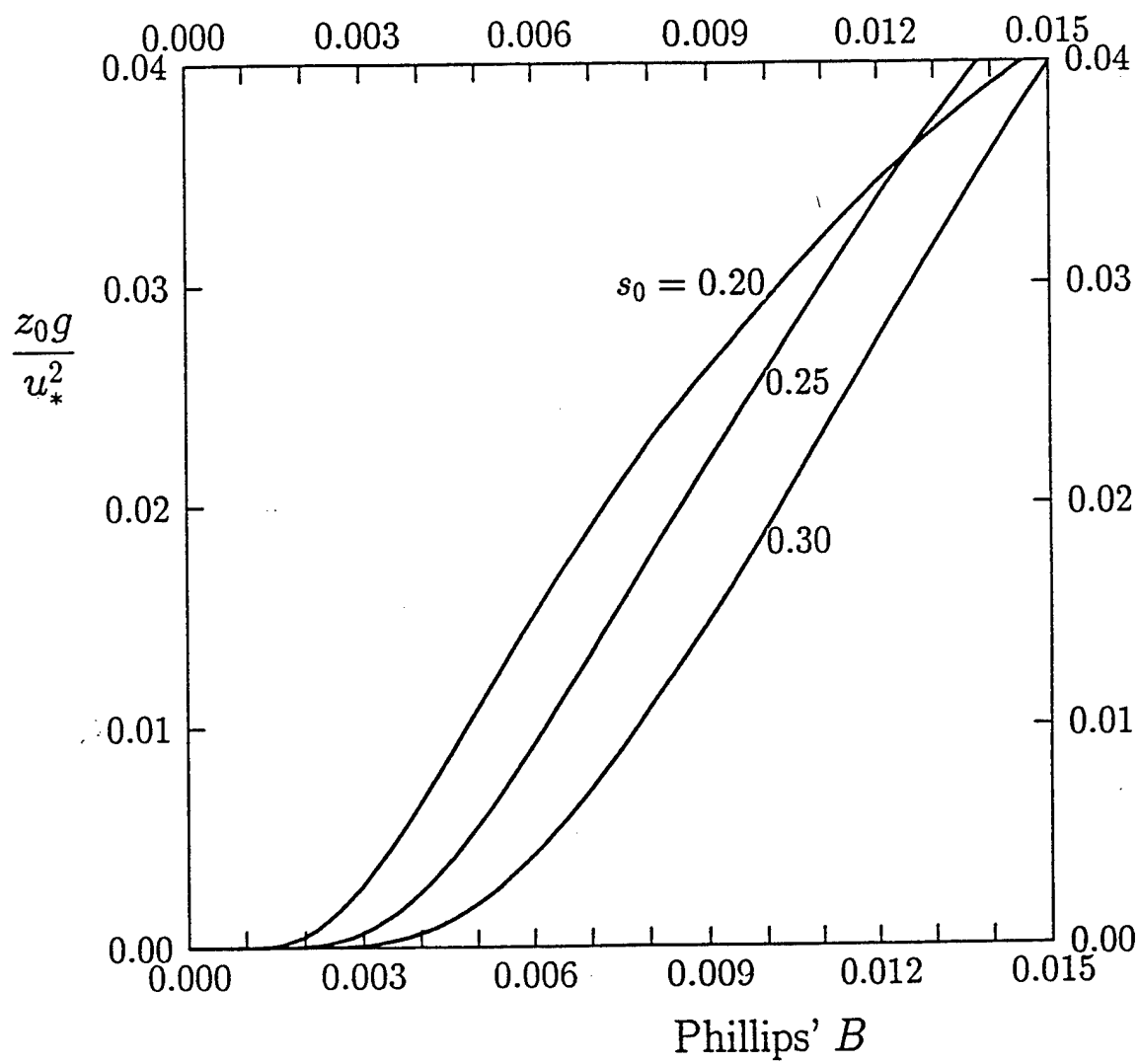


Figure 2

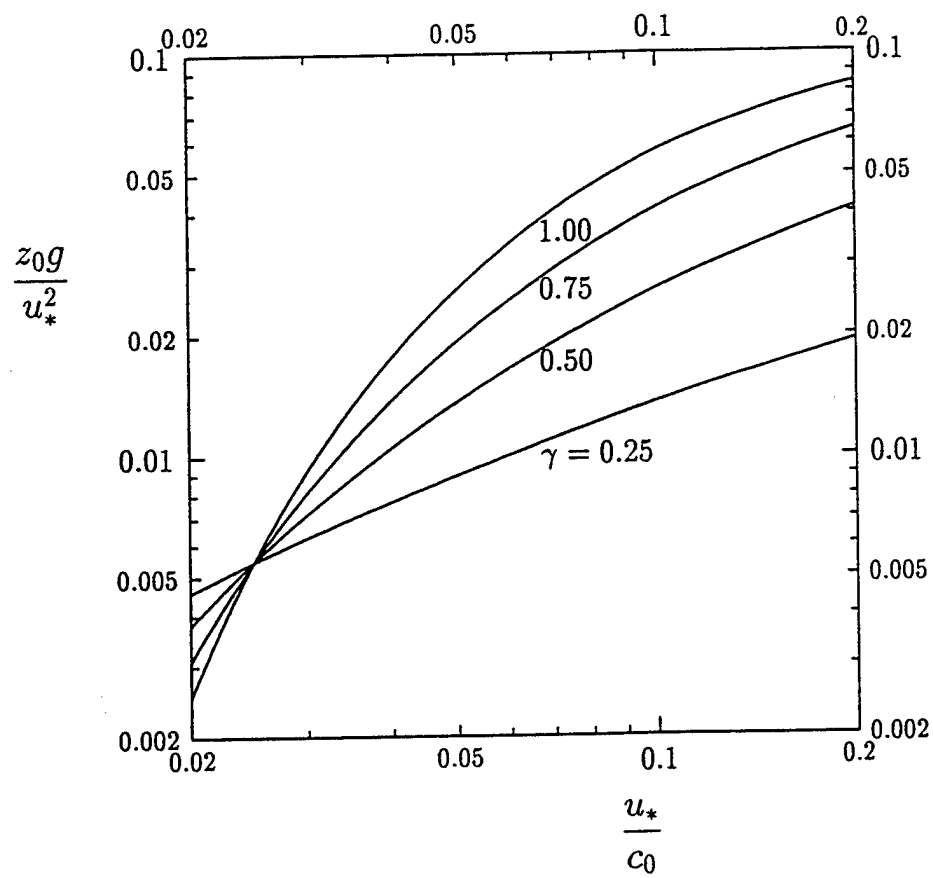


Figure 3

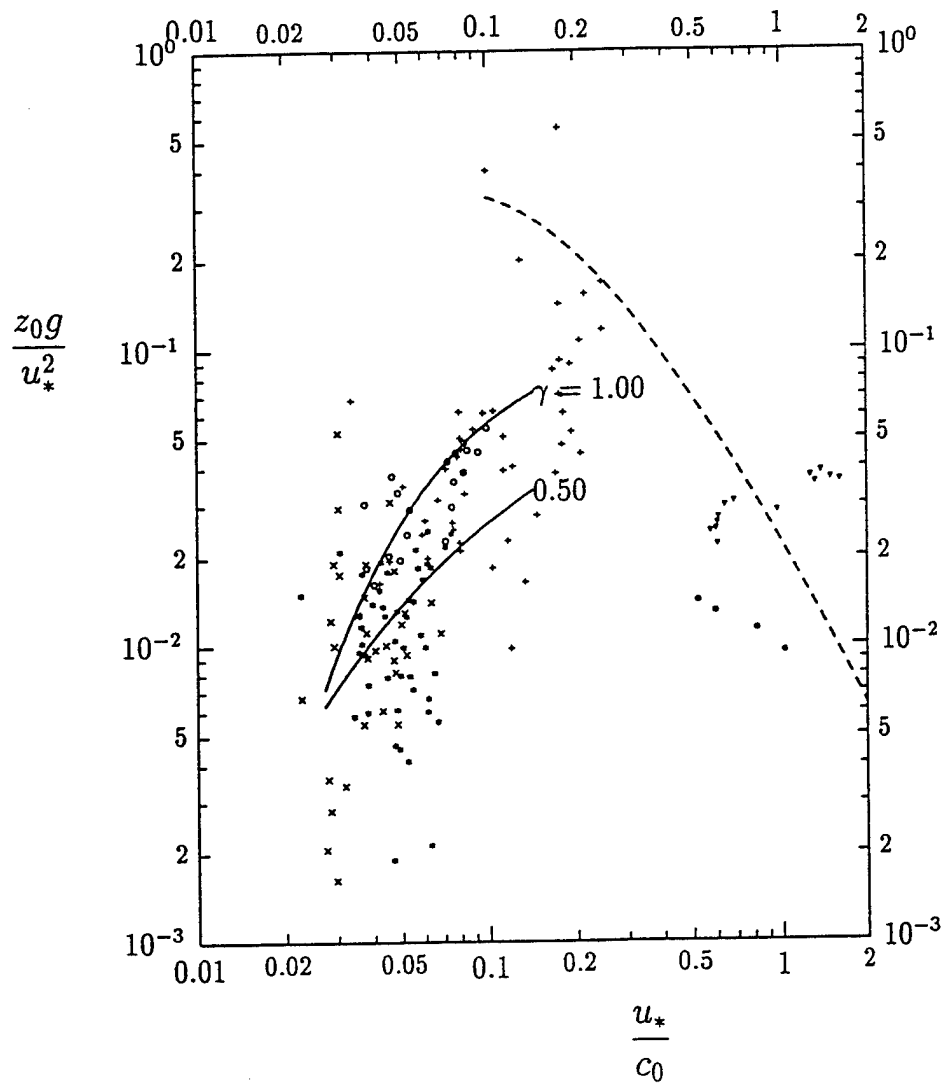
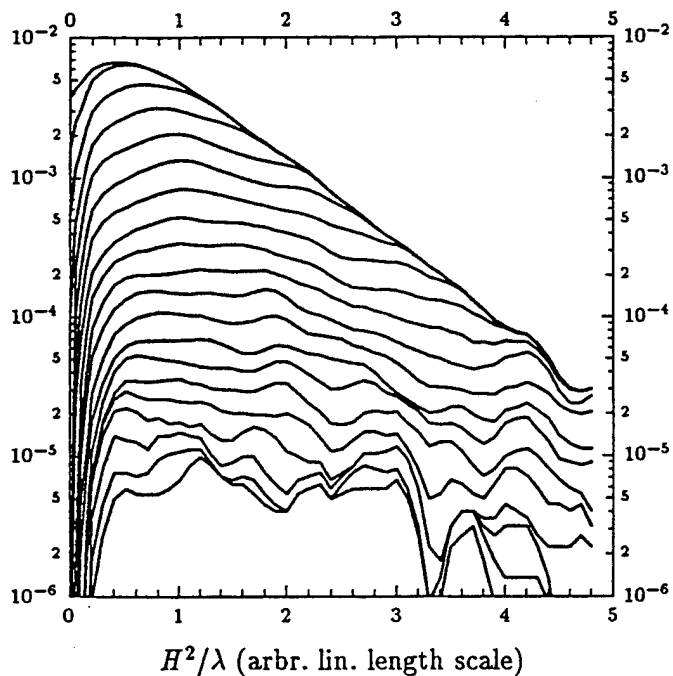
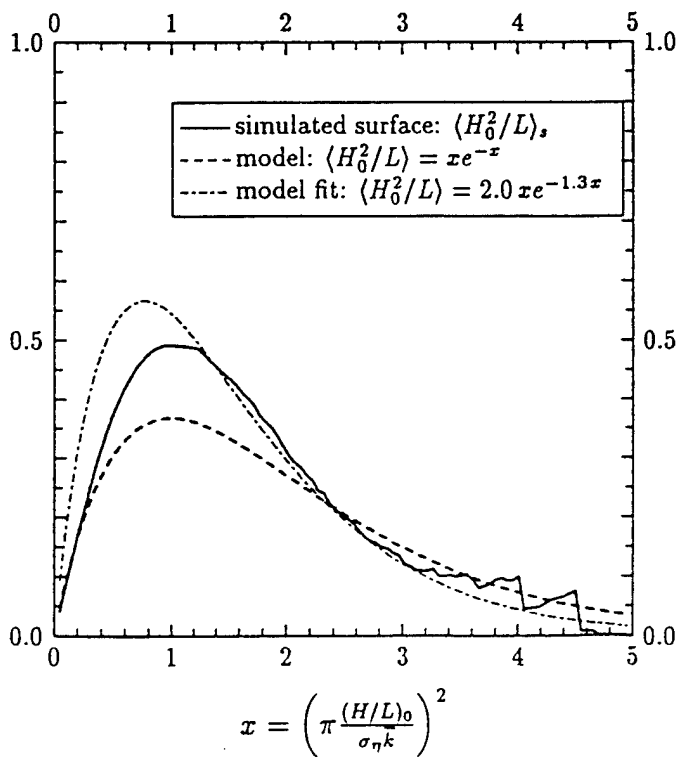


Figure 4

Density distribution function of H^2/λ
when $\pi H/\lambda > s_0$ for $x = 0.05$ (top curve)
and x incremented by 0.25 (subsequent
curves)



A 1



A 2

6. PUBLICATIONS SUPPORTED BY THE GRANT

Mahrt, L., Vickers, D., Howell, J., Højstrup, J., Wilczak, J., Edson, J. and J.Hare: Sea surface drag coefficients in RASEX. to appear J.Geophys. Res.

Vickers, D. and L. Mahrt: Quality control and assessment of flux sampling problem: Application to RASEX. to be submitted to J.Atm. and Oce.Tech.

Barthelmie, R. J., Melas, D. Højstrup, J. and M. S. Courtney: Wind speed modification in the transition from land to sea in the coastal zone. to be submitted to Bound.-Lay. Meteor.

Hansen, C. and S. Larsen: Further work on the Kitaigorodskii roughness length model: A new derivation using Lettau's expression on steep waves. To appear in *Geophysica*.

Højstrup, J.: Roughness lengths in coastal terrain. 11th Symposium on Boundary Layers and Turbulence. Charlotte, NC, March 1995, AMS, 481-484.

A. M. Sempreviva, Højstrup, J. and R. J. Bethelmie: Turbulent fluctuations of heat and moisture in the marine surface layer. Tenth Symposium on Turbulent Shear Flows. The Penn. St. U., August 1995. P3 103-107.